Dissertation

Bernd von Kuhlmann

Properties of the population of field galaxies at medium redshift

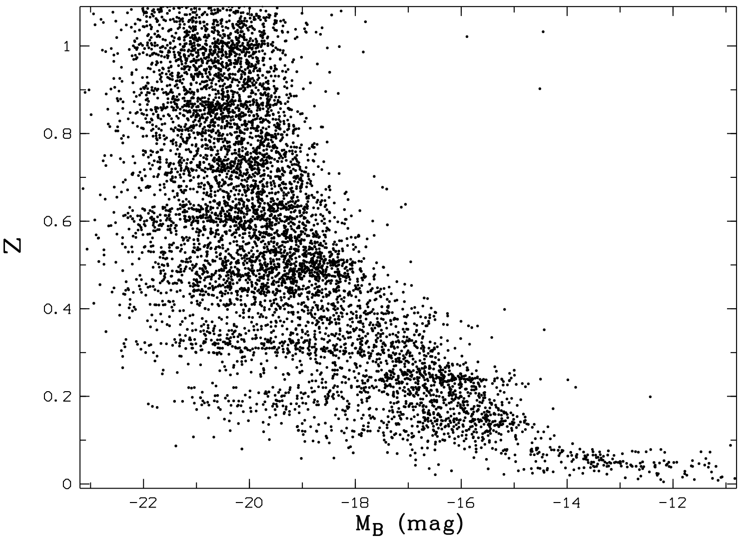

Max–Planck–Institute
for Astronomy
Heidelberg 2002

Dissertation
submitted to the
Combined Faculties for the Natural Science and for Mathematics
of the Ruperto–Carola University of Heidelberg, Germany
for the degree of
Doctor of Natural Sciences

presented by

Diplom–Physicist: Bernd Max Friedrich von Kuhlmann
born in: Bielefeld, Germany

Oral examination: 12th February 2002

Properties of the population of field galaxies at medium redshift

Referees: Prof. Dr. Josef Fried
Prof. Dr. Roland Wielen

Zusammenfassung
Eigenschaften der Population von Feldgalaxien bei mittlerer Rotverschiebung

Der **C**alar **A**lto **D**eep **I**maging **S**urvey (**CADIS**) hat auf vier Feldern mit insgesamt 435,2 Quadratbogenminuten Informationen über 8000 Galaxien gesammelt und mit einer fotometrischen Methode Rotverschiebungen sowie Galaxientypen (nach spektralen Eigenschaften) bestimmt. In dieser Arbeit werden die Galaxien im Bereich von $0{,}1 < z < 1{,}1$ untersucht und statistische Aussagen zu dieser Stichprobe gemacht.

Gefunden wurde für späte Galaxientypen (Starburst oder Irreguläre) eine über den gesamten Rotverschiebungsbereich innerhalb des Fehlers konstante Leuchtkraftfunktion ($\phi^* \approx 0{,}003\,{}^1/_{\mathrm{Mpc}^3}$, $M^* \approx -21{,}5^{\mathrm{m}}$, $\alpha \approx -1{,}5$). Für Galaxien der Typen E, S0, Sa, Sb und Sc konnte eine Erhöhung des Parameters M^* um 1,5 Magnituden von fernen Galaxien bei z = 1,1 zu nahen Objekten bei z = 0,1 festgestellt werden.

Der Anteil dieser Galaxientypen steigt in diesem Rotverschiebungsbereich auf das 1,5–fache. Ferner wurde festgestellt, dass die Population alle Galaxientypen im Durchschnitt von $z = 1{,}1$ bis $z = 0{,}1$ röter geworden sind (steigendes B–V).

Vergleiche mit Modellen der hierarchischen Galaxienbildung haben gezeigt, dass dieser Rötungseffekt konsistent mit Simulationen ist.

Ferner haben wir die fotometrischen Informationen mit Simulationen von Spektren verglichen und konnten gute Anzeichen dafür finden, dass die Sternentstehungssrate bei $z = 1{,}4$ ein Maximum gehabt hat, wie von Madau et al. proklamiert [Madau et al., 1998].

Abstract
Properties of the population of field galaxies at medium redshift

In the **C**alar **A**lto **D**eep **I**maging **S**urvey (**CADIS**), over 8000 galaxies were observed within an area of 435.2 arcmin^2. On the basis of 17 observed filters they were classified according to redshift and spectral energy distribution. In this work we present analysis of the population of galaxies in the redshift range of $1.1 > z > 0.1$.

For late type galaxies no evidence for evolution in the B–band luminosity function can be found over the whole redshift range ($\phi^* \approx 0.003\,{}^1/_{\mathrm{Mpc}^3}$, $M^* \approx -21.5^{\mathrm{m}}$, $\alpha \approx -1.5$). For early type galaxies (E, S0, Sa, Sb and Sc) we found an evolution of the luminosity function. The bright cut–off of the luminosity function is shifted by 1.5 magnitudes. Thus, the population of galaxies tends to become brighter with time.

The fraction of early type galaxies rises towards lower redshifts by a factor of 1.5. The population of all galaxy types tend to become redder at local redshifts (B–V rises).

Comparing the CADIS data set to simulations of hierarchical modeling, the simulated data set becomes redder at low redshift, as well.

We analyzed simulations of chemically consistent spectral evolution with our photometric data and determined the time passed since the last major star formation process in early type galaxies. We found strong evidence that the star formation rate peaks around $z = 1.4$ as the Madau–plot suggested [Madau et al., 1998].

Dedicated

to my

parents

Karin

and

Emmich † 12. March 2001

... it doesn't matter how

beautiful your theory is,

it doesn't matter how smart you are

— if it doesn't agree with experiment,

it's wrong.

Richard Phillips Feynman (1918–1988)

Contents

Chapter 1

Introduction

The question of how galaxies form and evolve from the early stage of the universe until the present is one of the challenges of modern astronomy. An advantage in astronomy is that peering out into space is equivalent to looking back in time, due to the finite speed of light. By observing very distant objects we can thus learn about the past of the universe. The interest in the subject of galaxy evolution increased in the 1990s. The fraction of publications on galaxy evolution in that decade rose up to 15% of the scientific publications in the field of astronomy [Ellis, 2001]. Nowadays, the knowledge on galaxy evolution is growing rapidly and is being increasingly discussed in the scientific community.
Continuously larger distances in astronomical observations are reached with the new generation of 8–10–meter class telescopes and more efficient CCD–detectors as well as with space based observations. Thus, we observe fainter objects, and with the increasing look–back time we can observe more and more of the history of galaxies and how they evolve with time. Only ten years ago, the observational limit was still at a redshift of four, whereas nowadays the most distant objects observed are a galaxy at a redshift of $z = 5.58$ and a quasar at $z = 6.28$ [Fruchter, 2001, Fan et al., 2001].

Extragalactic research has a long history. Already in 1755 the philosopher Immanuel Kant had first conceived that those little fuzzy objects are *island universes* far beyond the edges of our Milky Way. Today this objects are called galaxies[1], and we know since Edwin Hubble's studies in 1924, that they have extragalactic nature. Hubble set up his famous scheme for the classification of galaxies into morphological types (figure 1.2). Hubble named E–S0 galaxies as early type galaxies and Sa, Sb, Sc as well as irregular galaxies as late type galaxies.
Analysis of the stellar population in galaxies showed that elliptical galaxies have nearly no ongoing star formation and consist of an old population of stars. Irregular or starbursting galaxies are dominated by a young component of stars which have formed more recently. As it was discovered recently, the sequence of morphological types arises most certainly from a merging process. This process starts with irregular dwarf galaxies, next spirals (Sa,

---

[1] *Galaxy* originates from the Greek expression *gala* for milk.

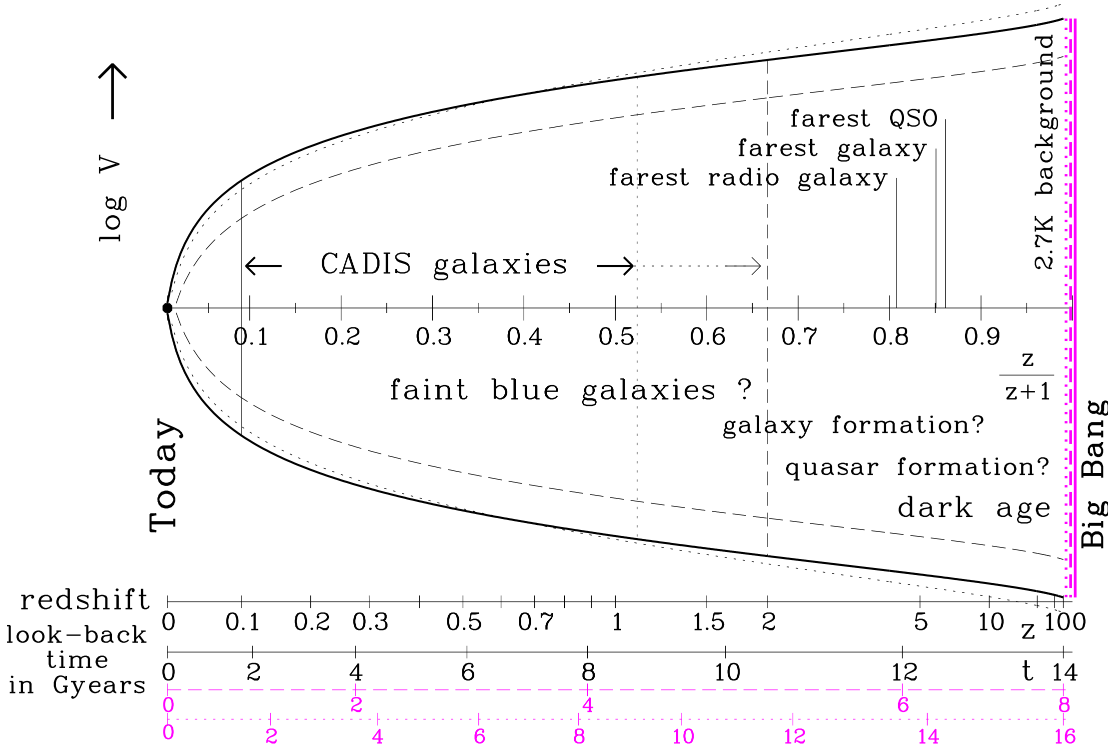

Figure 1.1: Redshift structure of the universe with observational information and theoretical view; abscissa logarithm of volume of the universe from 0 to $z\ /(z{+}1)$
Three cosmologies with different volume and time axis are used:
$\Omega_m = 1$, $\Omega_\Lambda = 0$, $q_0 = 0.5$, $H_0 = 50$ km/(sec Mpc) solid lines
$\Omega_m = 1$, $\Omega_\Lambda = 0$, $q_0 = 0.5$, $H_0 = 100$ km/(sec Mpc) solid dashed lines
$\Omega_m = 0.3$, $\Omega_\Lambda = 0.7$, $q_0 = 0.5$, $H_0 = 62$ km/(sec Mpc) dotted lines

Sb, Sc) and finally elliptical galaxies (E) were formed, which almost entirely lost their star forming material. Therefore, ellipticals are galaxies with a long formation history.
Today, galaxies are more commonly classified by their spectrum rather than by their morphology, and thus by their stellar population and star formation history.

Figure 1.1 presents a scheme of mankind's current knowledge about the history of the universe. From the COBE[2] and BOOMERANG[3] observations of the 2.7K background fluctuation we know about the early phase of structure formation in the universe. However, the timescale for matter to condense and form the first stars, which ended the dark age, is still not clear. When and how quasars and galaxies formed remains an open question. Yet another question arises: What did galaxies look like in their early stages and how have they evolved to their present state?

---

[2] **COBE:** The **Co**smic **B**ackground **E**xplorer was an astronomical satellite experiment to measure the diffuse infrared and microwave radiation (1989–1990).

[3] **BOOMERANG**: **B**alloon **o**bservations **o**f **m**illimetric **e**xtragalactic **r**adiation **an**d **g**eomagentics (1997–1998).

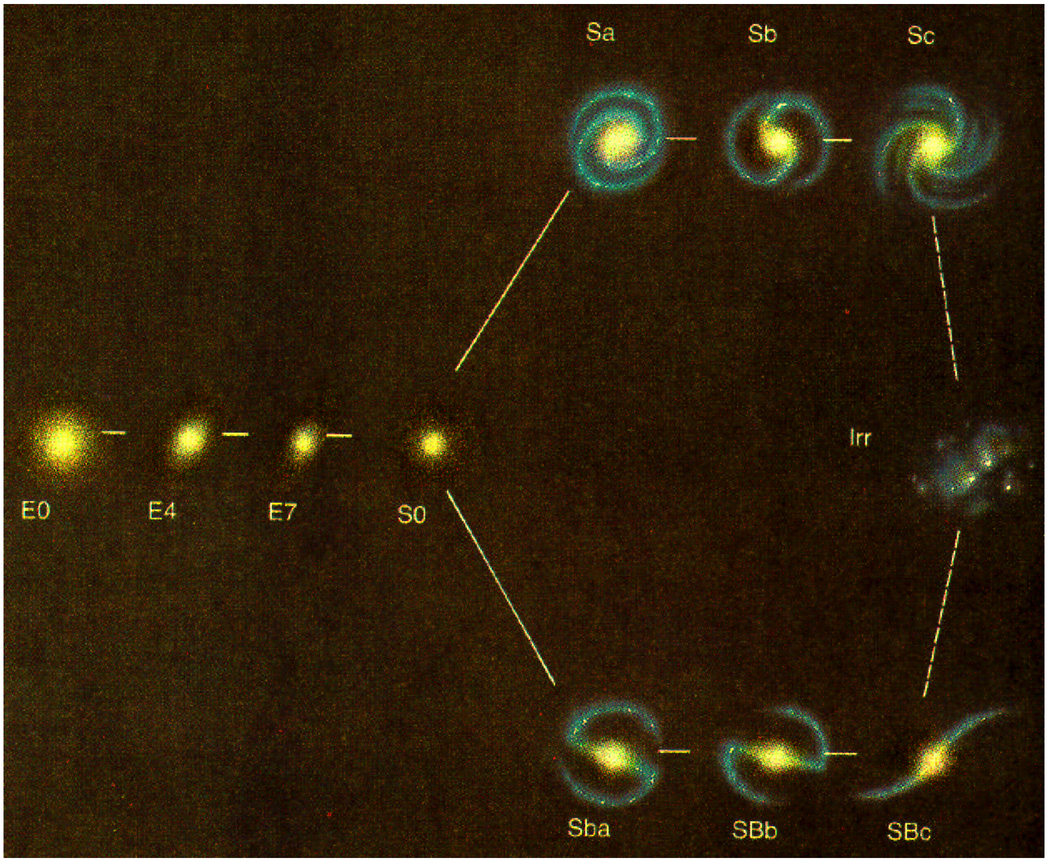

Figure 1.2: Hubble sequence for morphological classification of galaxies (Hubble's tuning fork diagram); different colors indicate different populations of stars in the galaxies. [Chaisson and Mc Millan, 1993]
Early type galaxies: elliptical galaxies E0–E7 and S0
Late type galaxies: spiral galaxies Sa, Sb and Sc
barred spiral galaxies: SBa, SBb, SBc
and irregular galaxies Irr

The present population of galaxies is observed to be different from the population in the earlier universe. According to observations of the local universe ($z < 0.01$) the predicted number of red galaxies at medium redshifts ($0.3 < z < 1.5$) is as expected. But faint blue galaxies show an excess in their population [Ellis, 1997]. Thus, the question arises: Did the numerous blue galaxies that are present in the younger universe merge to create present–day galaxies, or was an initial burst of star formation responsible for the temporary brightness of small galaxies? At medium redshifts ($0.1 < z < 1.5$) there are ten times more faint blue galaxies than in the present population.

This rules out the steady state theory and favors hierarchical models for the evolution of the universe. Therefore, the star formation rate had to change during this epoch of the evolution of the universe. Madau claimed in 1996 that the star formation rate increases

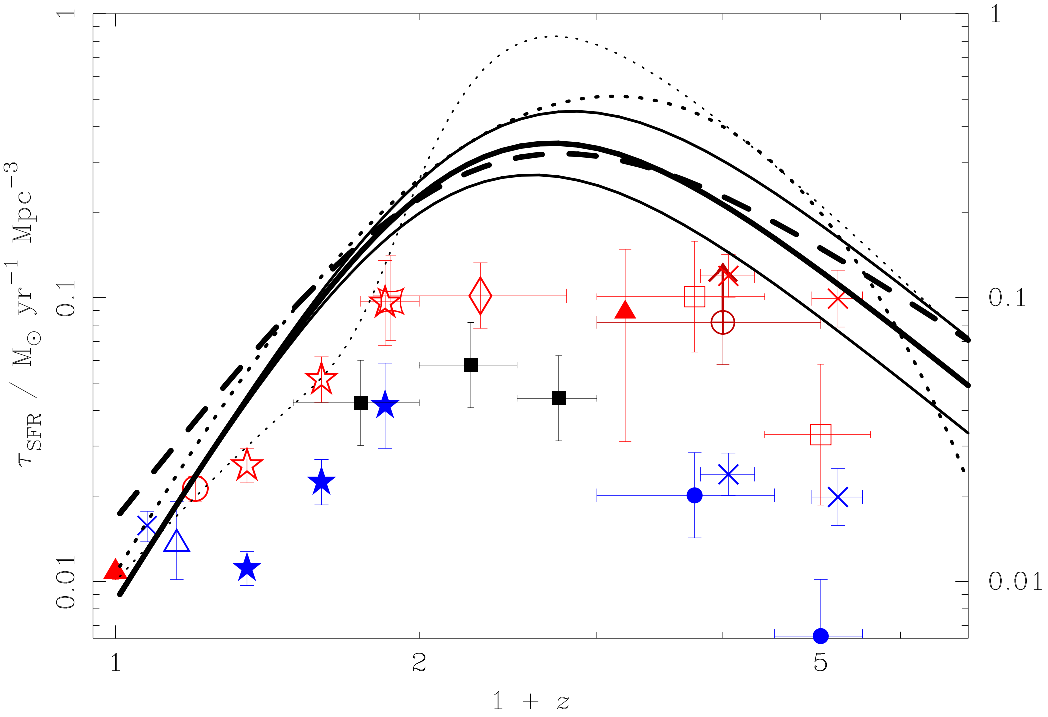

Figure 1.3: The history of star formation as density (τ) inferred from different models and observations (Madau plot)[Blain, 2000, Ellis, 2001, Madau et al., 1998].
The thick solid, dashed and dotted lines represent the simple luminosity evolution model and the hierarchical model, respectively. The thinner solid lines show the approximate envelope of 68% uncertainty in the results of the simple model. The data points are taken from a variety of sources.

steeply within $0 < z < 2$, but approaches zero at high redshifts as is expected (figure 1.3) [Madau et al., 1996, Blain, 2000]. Thus, the medium redshift range of $0.1 < z < 1.5$ is an interesting epoch to study, and motivates the work presented here. The CADIS[4] galaxy sample spans a time range of more than 50% of the age of the universe, thus being ideally suited to study the evolution of galaxies.

There are several surveys currently analyzing the medium redshift galaxy population. The CFRS[5] [Lilly et al., 1995] yielded a spectroscopic sample of 730 galaxies in the range of $0.1 < z < 0.75$. The Autofib[6] [Ellis et al., 1996] survey measured 1700 spectroscopic redshifts up to $z = 0.75$. The 200 spectra of the CNOC2[7] [Lin et al., 1999] survey are reaching a redshift up to $z = 0.55$. However, their conclusions about evolution are controversial and need further investigation. How this evolution is proceeding or if there is a consistency with a passive evolution with the observations remains unclear [Totani and Yoshii, 1998].

---

[4] **CADIS:** The **C**alar **A**lto **D**eep **I**maging **S**urvey is described in chapter 2.

[5] **C**anada–**F**rance **R**edshift **S**urvey

[6] **Autofib** redshift survey named after the **Auto**mated **Fi**bre **P**ositioner (AUTOFIB-2) at the William Herschel Telescope.

[7] **C**anadian **N**etwork for **O**bservational **C**osmology field galaxy redshift survey **2.**

In the CADIS project we used a different approach to survey medium redshift objects using a non–preselected sample. The derived photometric redshifts are based on a large set of medium and narrow band filters. The database of only half of the reduced survey area already holds more than 9000 galaxies in the redshift range $0.1 < z < 2.0$ with redshift errors of $\Delta z \leq 0.015$. The goal of the CADIS project is to study the properties of the galaxy population and bring more clarity to the evolution processes.

In this thesis we will add another piece of evidence to the big puzzle of knowledge about the evolution of the universe. Almost all observationally accessible quantities such as luminosity, colors, spectra, morphology, masses, and comoving space density may have changed substantially as individual galaxies evolve. Due to the large timescales involved, it is not possible to observe the evolution of an individual galaxy. This is why a statistical approach is useful: within CADIS a statistically relevant sample of galaxies is observed in different evolutionary epochs of the universe. With such snapshots of a large number of galaxies we investigate the general evolution of the galaxy population.

To gather such statistical information, we chose a survey project. A survey which samples a small representative fraction of the universe allows us to draw conclusions on the universe in general, virtually as *pars pro toto*[8]. In the CADIS project (chapter 2), we observe a fraction of the sky to identify a statistical sample of galaxies and derive information about their intensity in different filters. We then analyze the properties of this galaxy sample at different epochs in the history of the universe and investigate evolutionary effects in chapter 3. Questions concerning the evolution of the luminosity function of galaxies, the evolution of the spectral energy distribution or color indices will be addressed.

Besides observations (or experiments), theory has been established as the second foundation of modern science. Theoretical astrophysics models the universe with physical equations and computer simulations and predicts observational quantities. In chapter 4 we bridge between theory and observation by comparing a hierarchical semianalytic model of the evolution of the galaxy population to the results of the observed data set.
In chapter 5, we address the aspect of theoretical spectral evolution of single galaxies and compare this to the observed spectral evolution, in order to derive information about the age of galaxies from our data set. Finally, we give a summary and point out prospects for future work in chapter 6.

Throughout the entire work, unless noted differently, an Einstein–de Sitter cosmological model with $\Omega_m = 1$, $\Omega_\Lambda = 0$ and $q_0 = 0.5$ and a Hubble constant of $H_0 = 50\,\mathrm{km/(sec\,Mpc)}$ is used ($h = H_0/(100\,\mathrm{km/(sec\,Mpc)}) = 0.5$).

---

[8] From Latin: *A subsample representing the whole.*

Chapter 2

CADIS

2.1 The CADIS project

The **C**alar **A**lto **D**eep **I**maging **S**urvey (henceforth **CADIS**) is a key project of the *Max–Planck–Institute for Astronomy in Heidelberg* since spring 1996. It combines the instrumental resources of the institute (the 2.2– and 3.5–meter–telescopes on Calar Alto, Spain) with the upcoming access of the new 8–10 meter class telescopes. We observed a large sample of objects in a deep survey with easily accessible telescopes on Calar Alto to provide larger telescopes with interesting targets for follow–up observations.

Primary goal and origin of the project is the search for primeval galaxies at high redshifts [Beckwith et al., 1998, Meisenheimer et al., 1998, Thommes, 1996]. Those primeval galaxies are also known as Lyman–α (henceforth Ly–α) galaxies, due to their strong Ly–α emission. The detection of the Ly–α emission line is done by the use of a combination of narrow wavelength Fabry–Pérot (henceforth FP) images and a set of supporting narrow and broadband filters. To find Ly–α emission lines, a set of 8–9 neighboring 1.8–2.5 nm wide FP–images were taken (table 2.1). The wavelengths ranges were chosen to avoid night sky emission lines. The integration times allows object detection down to $L = 3 \cdot 10^{-20}\,\mathrm{W/m^2}$. To identify detected emission lines as high redshift Ly–α galaxy candidates foreground emission line galaxies have to be excluded. When those objects are low redshift ($z < 1.5$) Hα, Hβ, [O II] or [O III] emission line galaxies additional lines should be detected in appropriate wavelength differences. This leads to a set of 3 medium/narrow–band *veto* filters (table 2.1) for each FP-setting. A set of broad band (also called backbone) filters from B to K (table 2.1) has been added to measure the continuum level underneath the emission lines and to enable a multi–color classification. So far, no other project has yet a filter set covering an equivalently wide range in optical and infrared wavelengths (figure 2.1). Thus, we are able to address a wide range of scientifically interesting problems:

- ▷ Search for Ly–α candidates at redshifts of $z \approx 4.7$ (FP–A), $z \approx 5.7$ (FP–B) and $z \approx 6.6$ (FP–C) (see table 8 and figure 2.2) [Thommes, 1996],

λ_c (nm)	$\Delta\lambda$ (nm)	CADIS filter name	$\Delta t_{2.2m}$ (ksec)	observational goal in Vega magnitude	remarks
396	10	V 396	50	23.5	veto for FPI–A
461	113	B B (B′)	10	25.0	
465	9	V 465	40	24.0	veto for FPI–B
489	20	B 489	20	24.0	
522	15	V 522	40	24.0	veto for FPI–A and FP–C
535	14	V 535	40	24.0	veto for FPI–A
611	16	V 611	25	23.8	veto for FPI–B
628	16	V 628	32	23.8	veto for FPI–B
649	172	B R2 (R_2)	10	24.5	
683	18	V 683	20	23.3	veto for FPI–C
702	19	B 700	15	23.7	FP–A prefilter, veto for FPI–C
752	28	B 752	22	23.0	
815	25	B 815 (I)	20	23.0	FP–B prefilter
855	13	B 855	40	22.6	
909	33	B 909	40	22.4	FP–C prefilter
1250	300	B J	40	21.8	Δ t for 3.5m
2150	300	B Kp (K′)	40	19.8	Δ t for 3.5m
694.5	1.8	*I* 694	10	21.52	FP range A (9 settings)
696.0	1.8	*I* 696	10	21.515	
⋮	⋮	⋮	⋮	⋮	
706.5	1.8	*I* 706	10	21.48	
814.0	2.0	*I* 814	12	21.17	FP range B (9 settings)
815.0	2.0	*I* 815	12	21.16	
⋮	⋮	⋮	⋮	⋮	
824.0	2.0	*I* 824	12 18	21.13	
910.0	2.5	*I* 910	22	20.77	FP range A (8 settings)
911.5	2.5	*I* 912	22	20.76	
⋮	⋮	⋮	⋮	⋮	
926.0	2.5	*I* 926	22	20.73	

Table 2.1: Filter set and Fabry–Pérot (FP) bands of the CADIS project
B = broad band (*backbone* or *broadband*); V = veto filter (medium/narrow band);
I = interferometer exposure
$\Delta t_{2.2\mathrm{m}}$ = observation time at a 2.2–meter–telescope to reach the observational limits for the filter observation in each field

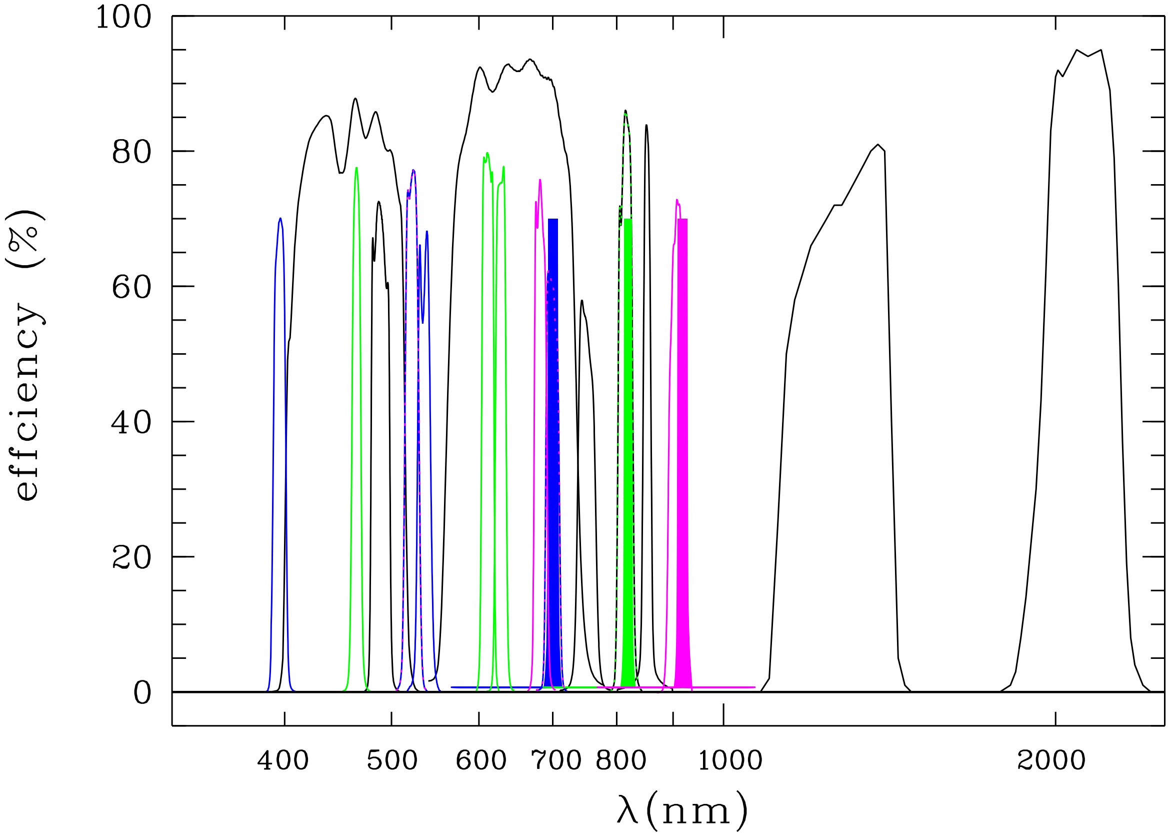

Figure 2.1: CADIS filter set
black = medium/narrow band filter; magenta = FP–C + veto filter; green = FP–B + veto filter; blue =FP–A + veto filter

- ▷ Evolution of galaxies in the medium redshift range, $0.2 < z < 1.5$, as addressed in this work and [Fried et al., 2001, von Kuhlmann and Fried, 1999],
- ▷ Investigation of quasar density at a wide redshift range ($0 < z < 6$) [Wolf et al., 1999, Wolf, 1999],
- ▷ Luminosity function of emission line galaxies in the FP–settings [Fockenbrock, 1998, Hippelein, 2002],
- ▷ Density and properties of **E**xtremely **R**ed **O**bjects (**ERO**s) [Thompson et al., 1999],
- ▷ Search for very late–type M dwarfs and brown dwarfs [Wolf et al., 1998],
- ▷ Structure of the Milky Way from the faint stellar foreground population in different galactic lines of sight [Phleps et al., 2000, Phleps, 1998],
- ▷ Clustering of emission line galaxies and *normal* galaxies (2 dimensional correlation function),

- ▷ Longterm variability of objects.

The distributions in time and redshift of extragalactic objects addressed by CADIS, are illustrated in figure 2.2.

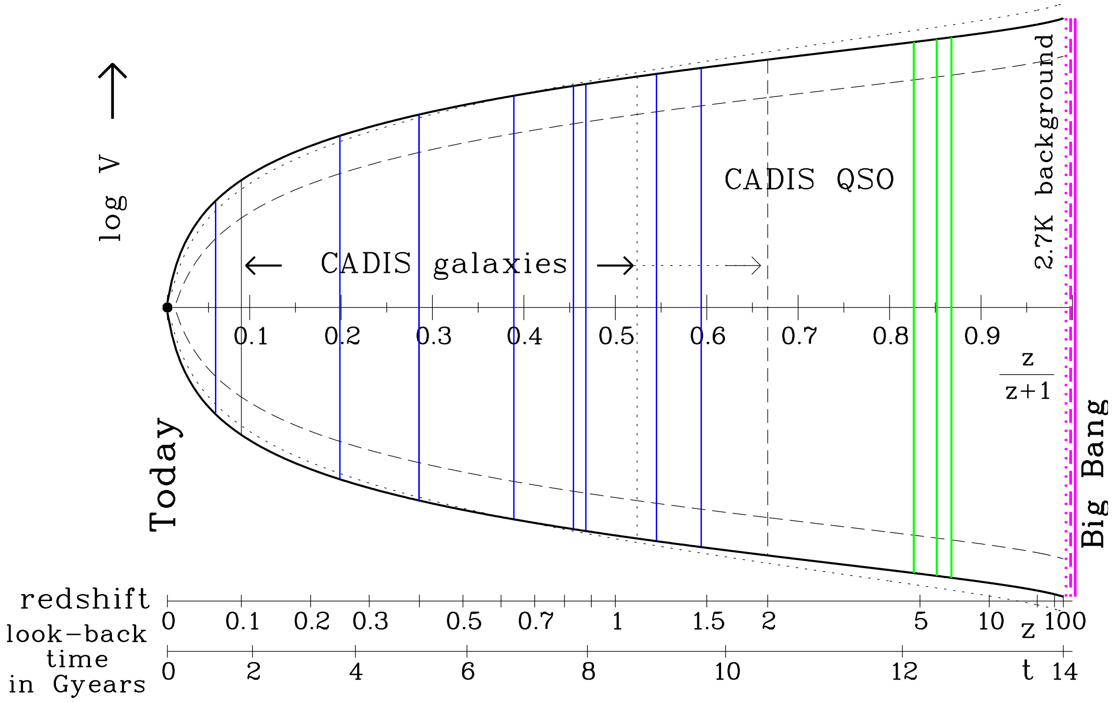

Figure 2.2: Distribution of extragalactic objects observed by CADIS (blue: emission line galaxies Hα, O[II] and O[III], green: primeval /Ly–α galaxies);
$\Omega_m = 1$, $\Omega_\Lambda = 0$, $q_0 = 0.5$, $H_0 = 50$ km/(sec Mpc) cosmology is used; further explanation are given in figure 1.1.

The accessed area in the sky is based on the capabilities of the instruments of the institute. For the observations in the optical we use the two focal reducers MOSCA [von Kuhlmann, 1997] and CAFOS [Glänzer, 1994, Meisenheimer, 1994]. CAFOS has a round aperture of Ø = 13.5 arcminutes and MOSCA a rectangular aperture of 11×11 square arcminutes. The Omega prime camera with 4 pointings of 6×6 square arcminutes field is used in the infrared. The overlapping sky coverage of all three instruments is 10×10 square arcminutes, which is used as a CADIS field.
A compromise had to be found between observation depth and observed area. In CADIS eight fields were chosen to give a statistically large enough data set to find primeval galaxies. The criteria for the field selection were as follows:

- ▷ Absence of bright objects (foreground stars) in the field ($m > 16^{\mathrm{m}}$)
- ▷ Location at high galactic latitude with a small (< 2 MJy/sr) interstellar extinction, based on the IRAS maps of the 100μm emission, to avoid reddening effects and galaxy clusters

- ▷ Fields visible from Calar Alto and distributed such that observations can be carried out throughout the whole year
- ▷ A few fields were chosen close to the celestial equator to allow for follow–up observation using the VLT observatory in the southern hemisphere
- ▷ One field should have a spacial overlay to other projects (in order to compare classification etc.)

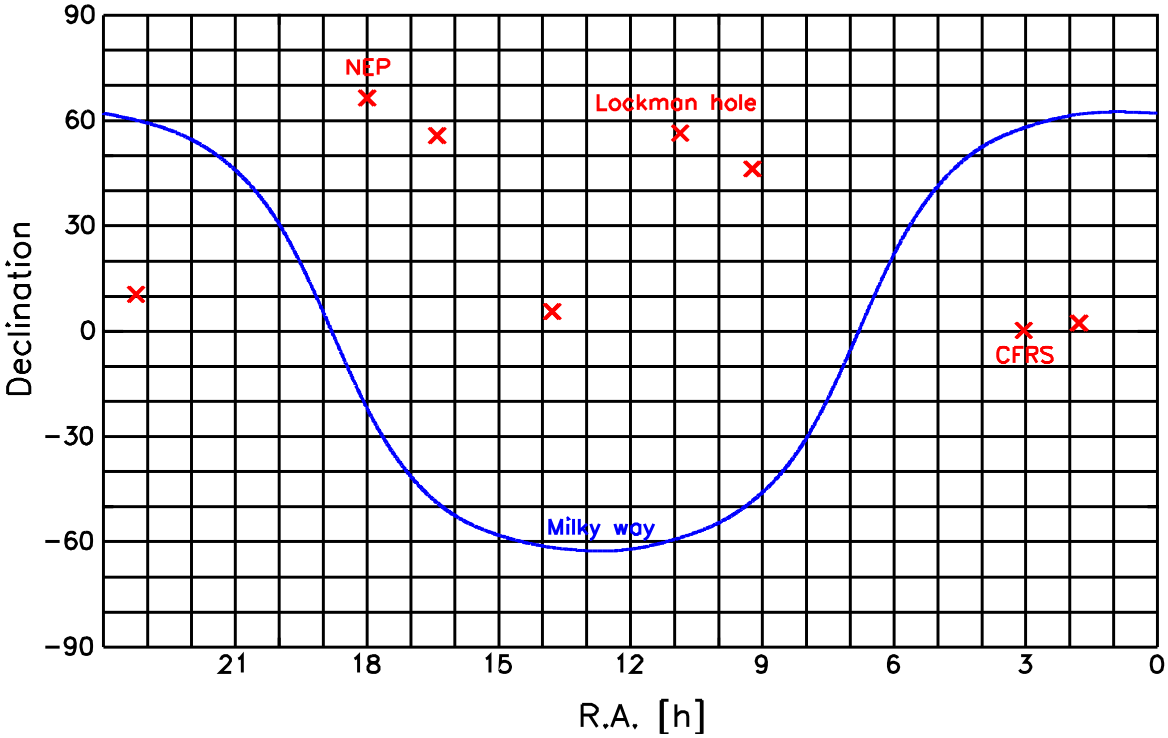

Figure 2.3: Positions of the CADIS fields on the sky.

CADIS field	ID	α (2000)	δ (2000)	remarks
1 h	A	$1^h47^m33^s$	02° 19′55″	
3 h	T	$3^h02^m40^s$	00° 10′00″	CFRS field (reduced filterset)
9 h	B	$9^h41^m47^s$	46° 14′20″	
10 h	L	$10^h52^m05^s$	57° 25′25″	Lockman Hole
13 h	D	$13^h47^m42^s.3$	05° 37′34″	
16 h	F	$16^h24^m32^s.3$	55° 44′32″	
18 h	N	$17^h59^m43^s.8$	66° 21′21″	NEP
23 h	G	$23^h45^m46^s.9$	11° 27′00″	

Table 2.2: Positions of the CADIS fields on the sky (±5″)

Distribution and positions of the selected fields are shown in figure 2.3 and table 2.2. The observations were performed during 1996–2001, they are nearly finished in over 600 nights of allocated telescope time. For four fields 90% of the observed data are completed. The 5σ detection limits are summarized in table 2.3.

In each filter five to fifteen individual exposures were taken with an average seeing of 1.5 arcsec. All images observed in the same filter are co–added to a single deep result frame (sumframe). Object detection is done on the sumframes using the SExtractor software [Bertin and Arnouts, 1996]. Object tables of all filters and FP were combined. All objects were considered identical, if they fall into a common error circle of one arcsecond radius. Therefor in the final object list detections are included, even if they are detected in only one filter or FP setting.
There are two reasons for taking a weighted fixed radius aperture. Firstly, there are objects with no significant flux in that measured filter. Thus, the aperture has to be limited in size, not to measure flux of a neighboring object. Second in order to suppress background noise in the measurements it is radial weighted, because the observed objects have different angular sizes.

The fixed weighted aperture is initially round, but is folded with the point spread function of each single flat fielded and cosmic[1] corrected frame. Thus, different seeing conditions are taken into account.
The photometry was calibrated by 2–4 stellar spectra in each field, which were used as tertiary standards to secondary standard stars [Oke, 1990, Röser and Meisenheimer, 1991, Walsh, 1995]. A precise photometric error can be derived from the variance of five to fifteen single frame measurements and is therefore superior to other techniques [Röser and Meisenheimer, 1986, Röser and Meisenheimer, 1991]. From the physical photon fluxes astronomical logarithmic Vega magnitudes were calculated:

$$m_\lambda = -2.5 \log_{10} \frac{F_{object}(\lambda)}{F_{Vega}(\lambda)} \,. \tag{2.1}$$

- ▷ $F_{object}(\lambda)$ object flux at a certain wavelength,
- ▷ $F_{Vega}(\lambda)$ Vega flux at a certain wavelength,
- ▷ m_λ astronomical logarithmic magnitude in mag.

For CADIS color indices a special magnitude scale — the CD magnitude — was defined in [Wolf, 1999] as

$$\mathrm{CD}_{\mathrm{mag}} = -2.5 \cdot \log_{10} \cdot F_{phot} + 20.01^{\mathrm{m}} \,,$$

---

[1] Cosmic ray or cosmic hit: High energy particles which are pretending to be a luminous astronomical object in the observed image but are due to atmospherical radiation

where F_{phot} is the flux in $\frac{photons}{\mathrm{m^2 \cdot sec \cdot nm}} \left(= \frac{\gamma}{\mathrm{m^2 \cdot sec \cdot nm}}\right)$. The color indices are defined by

$$m_1 - m_2 = -2.5 \cdot \log_{10} \cdot \frac{F_{phot\,1}}{F_{phot\,2}} \,.$$

This system is chosen such that an object with a flat spectrum ($F_{phot} = const.$) has in all wavelengths the same CD–magnitude and all CD–color indices are zero. The offset is set to the Luminosity of Vega in for Johnson V (548 nm).

The classification of the objects is not done by morphology but by the best spectral match. To classify objects CD–indices are calculated from the CD–magnitudes for each filter measurement. The filter indices are compared with a set of template filter indices by using a maximum likelihood algorithm [Wolf et al., 2001, Wolf, 1999]. The templates contain 175 stellar spectra [Gunn and Stryker, 1983] of O to M type stars, which are interpolated into 211 spectra. For quasars 120 templates spectra in redshifts from 0 to 6 of 0.02 steps are calculated. They are assembled from two components and damped at wavelengths lower than 120nm. One component is a scaled emission line spectrum, the other a scaled power law continuum [Wolf, 1999, Wolf et al., 2001].

For galaxies, a library based on observed averaged local galaxy spectra of Kinney was used [Kinney et al., 1996, Wolf et al., 2001] . The galaxy types are identified by numbers coding the spectral energy distribution (henceforth SED). Kinney's ten averaged observed spectra are the basis of a more detailed set of 100 templates ranging from red to blue. The SED numbers range from 0 to 99 and is based on linear interpolation of the color index values. The incorporated reference spectra are as follows (SB = starburst):

E0	-	S0	-	Sa	-	Sb	-	SB6	-	SB5	-	SB4	-	SB3	-	SB2	-	SB1
0	-	15	-	30	-	45	-	75	-	80	-	85	-	90	-	95	-	99

The spectra were extended to the infrared on the basis of Bruzual models to fit the infrared J and K band data (figure 2.4) [Bruzual A. and Charlot, 1993]. Analysis done by Kinney et al. [Kinney et al., 1996] on the basis of Bruzual and Charlot [Bruzual A. and Charlot, 1993] models of synthetic stellar spectra showed that the E spectrum can be well reproduced by a 16 Gyr old single starburst population. The starburst spectrum can be reproduced by a 0.72 Gyr old galaxy with continuous star formation. This fit is only valid for the continuum of the spectrum, because nebular emission was not included in the models [Kinney et al., 1996].

For every object the best fitting spectrum from the templates is computed using a maximum likelihood algorithm. In the case of a galaxy we derive the most probable combination of redshift and SED. Details on the classification scheme can be found by Wolf et al. [Wolf et al., 2001, Wolf, 1999].

For a detailed description of the project consult the CADIS–web–page [Meisenheimer et al., 2001], the revised CADIS–proposal [Beckwith et al., 1998], or an overview of the project at [Meisenheimer, K., 2002] in preparation.

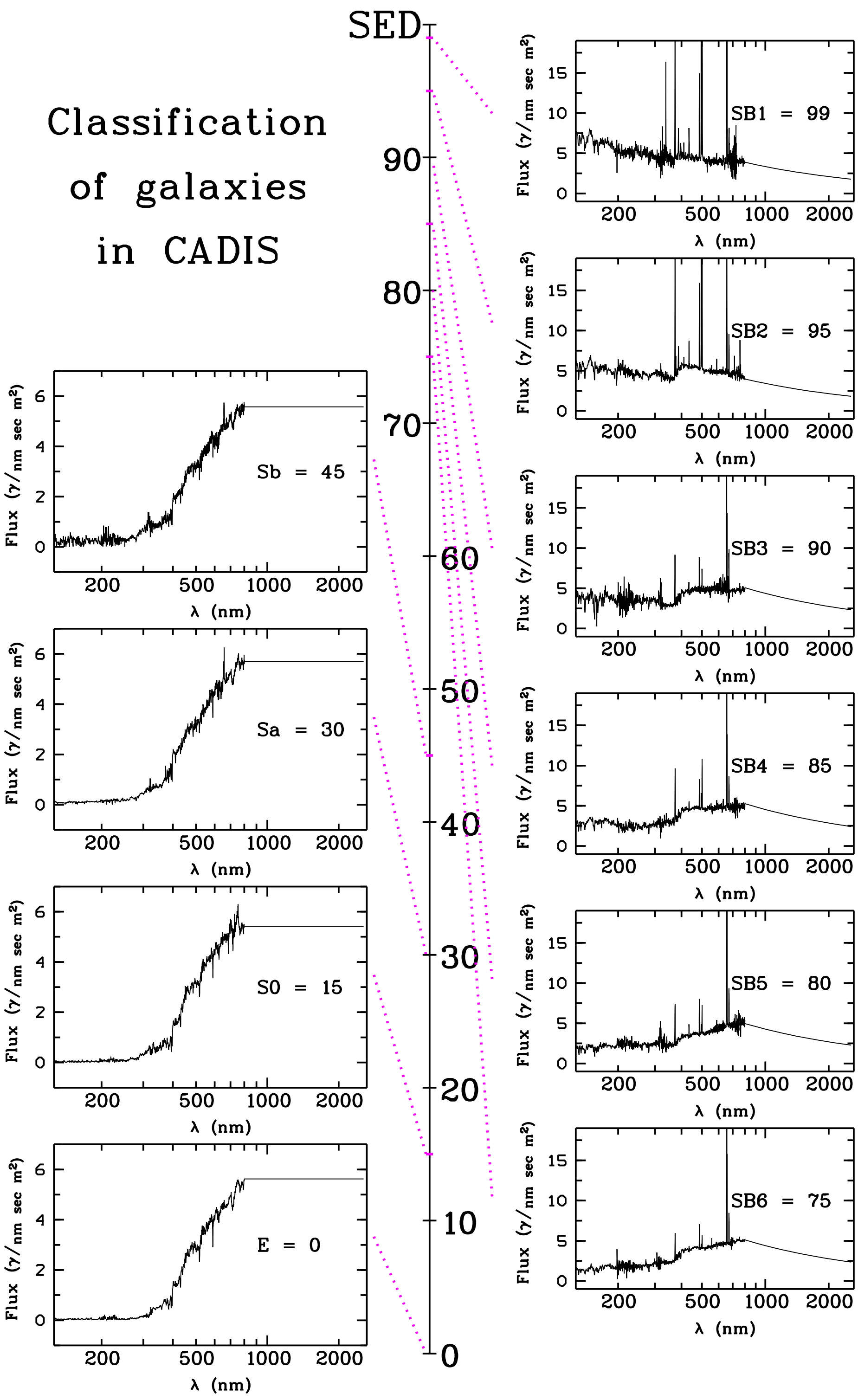

Figure 2.4: Template spectra from Kinney et al. [Kinney et al., 1996], which are incorporated into the CADIS–multi–color classification scheme [Wolf et al., 2001]. The fluxes in $\frac{photons}{\mathrm{m}^2 \cdot \mathrm{sec} \cdot \mathrm{nm}}$ $\left(= \frac{\gamma}{\mathrm{m}^2 \cdot \mathrm{sec} \cdot \mathrm{nm}}\right)$ are not normalized to absolute values, because CADIS only uses relative color–indices.

2.2 The CADIS data set

The project has collected 97% of all the broad and medium/narrow band filter data and 90% of the FPI-settings. The data set on which this work is based, includes the reduced data of four CADIS fields (compare table 2.2). Hereafter the fields are named by their position in right ascension as 1h–, 9h–, 16h– and 23h–field. Until April 2001, in these four fields observations of 12 to 17 filters were reduced. The 5σ detection limit in each filter and each field is summarized in table 2.3.

Field	V396	BB	V465	B489	V522	V535	V611	V628	BR2	V683	B700	B752	B815	B855	B909	BJ	BKp
1h	24.0	24.7	23.8		24.5		24.2	23.5	24.2		23.8	23.1	23.2		22.2		19.9
9h	23.4	24.8	23.9	23.5	24.3	24.0	23.4	23.8	24.5	23.5	23.8	22.5	22.9	22.3	21.9	21.5	20.0
16h		24.7	24.1	23.7	23.4	24.1	23.4	23.6	24.1	23.2	23.0	22.9	22.9	22.4	22.3	21.7	19.5
23h		24.7	23.6	22.9	24.6	23.3	23.5	23.3	24.5	23.4	23.5	23.2	22.4	21.6	21.6	21.6	19.5
goal	23.5	25.0	24.0	24.0	24.0	24.0	23.8	23.8	24.5	23.3	23.7	23.0	23.0	22.6	22.4	21.8	19.8

Table 2.3: CADIS broad and medium/narrow band filter observational limits (5σ–limit) in Vega magnitudes at data reduction status, April 2001

In each field we detect roughly 39 500 objects. The majority of objects are detected in only a few filters, often only in one of the FP-settings, because every detected object is represented. To provide reliable multi–color classification, detection in more than half of the broad and medium/narrow band filters is needed. We can thus perform a reliable multi–color classification for about 8% of the objects (table 2.4 row 2). Out of these, 19% are classified as stars or quasars and the remaining 81% as galaxies (table 2.4 row 3). These 9915 galaxies form the basis of most of the analysis in this work.

At the edges of the CADIS–fields not all flux information is available, because the survey uses three different instruments (section 2.1) with three different fields of view. Analysis of the two dimensional density (the number of objects per square arcminute) shows that the density of classified objects decreases with the number of measured filter fluxes.
A homogeneous sample is needed for deriving the luminosity function or density of galaxies. Thus, we define a *complete* subarea of the CADIS–fields as the area common to observations with all instruments used. The complete area is about 78% of the size of the field area and contains 8311 classified galaxies. Detailed object counts are summarized in table 2.4.

2.2.1 Morphological aperture correction of magnitudes

Photometry in CADIS is done using weighted fixed aperture in order to reduce background noise and nevertheless ensure the measurements of faint objects. This weight is derived from the point spread function of the individual frame and an effective aperture according to the maximum seeing.
Since the individual shape of the objects is not taken into account this aperture cuts

	object characteristic	1h	9h	16h	23h	all
1	detected objects	30 721	46 374	33 351	48 038	158 484
2	classified objects	2878	3104	3619	2644	12 245
3	classified galaxies	2423	2617	2853	2022	9915
4	classified galaxiesin *complete* area	2062	2301	2277	1671	8311
5	*complete* area in square arcminutes	111.6	109.6	103.9	110.2	435.2

Table 2.4: Object counts and classification in the CADIS–fields

off the flux at the edges of large objects. Therefore, our method measures lower fluxes than for example isophotal measurements using standard software like SExtractor [Bertin and Arnouts, 1996]. For further analysis first the total surface luminosity has to be derived.
Therefore, we correct our measured luminosities to real luminosities by an aperture correction factor. Measured fluxes for objects which are larger than the fixed aperture are corrected.

This cannot be done analytically, because of the complexity and variance of the weighted aperture and the error in the morphological information. A correction function was developed basing on a Monte Carlo simulation of a representative number of randomly generated objects, and fitting the parameter of a semianalytic function to the luminosity measurements.

In detail the following steps were performed to determine the morphological correction function:

- ▷ An artificial image of 10 × 10 arcmin^2 was created, with the same properties as a CADIS single frame observed in the BR2 filter, mainly the two dimensional object density luminosity distribution and shape . It contains 1900 randomly generated objects: elliptical galaxies (1000) with an $1/r^4$ profile, spiral galaxies (700) with a bulge (profile $1/r^4$) and a disk with exponential profile and 200 stars.
- ▷ The image was folded with a seeing profile (a double gaussian profile).
- ▷ Ten copies were created and individually generated noise was added to the single frames. The added noise was scaled with the intensity. Therefore, less noise appears in high luminosity objects than in the background. The following scaling function has been used:

$$F_{noise}(F) = F + noise\,\sigma_{real}\sqrt{1+F}$$

  - F_{noise} flux with noise,
  - F input flux
  - $noise$ normal distributed random values for the noise with $\sigma = 1$,
  - σ_{real} the standard deviation of background noise in a real frame.

- ▷ The single images were added up to give a sumframe.
- ▷ The photometric measurement procedure was performed as for all CADIS–images.
  - The objects were detecteded using SExtractor
  - At the object location the intensity was measured with a weighted fixed aperture in the ten single frames.
  - From the ten measurements the average intensity and the error was derived.
- ▷ By comparing the measured intensities to the initial intensities their deviations could be studied depending on morphological shape.
- ▷ A morphological correction function was fitted to the data, depending on two parameters morph1 and morph2. Morph1 is the major and morph2 the minor perpendicular axis and they indicate the difference in shape of each object in arcseconds compared to the pointspread function of the observed best signal to noise sumframe.

The fitting function is:

$$corr(morph1, morph2) = \left(\frac{\sqrt{morph1^2 + a^2 - 1} \cdot \sqrt{morph2^2 + a^2 - 1}}{a^2} \right)^b ,$$

with the free parameters a and b.
The function was derived as an approximation to an analytical folding of the object shape with the diameter of the measuring weighted aperture a^2 (compare CADIS description section 2.1), and the factor $-1 = -1^2$ to ensure that a round object has a correction factor of 1.
Morph1 and morph2 are measured by the SExtractor software in the sumframe with the best signal–to–noise ratio and compared to the pointspread function of that frame.

The best fits, using different seeings in the simulation, were found for the parameter set:

$$a = 1.5 \qquad \text{and} \qquad b = 1.25$$

This is a compromise between spiral and elliptical galaxies. We calculate a standard deviation of 0.12^{m}, which demonstrates the accuracy of the correction.

The correction function is shown in figure 2.5a. Stars are plotted in green and it is clear from the plot that they need no morphological correction. The spiral galaxies (in blue) show a narrow distribution, because their luminosity is dominated by a central bulge.

In summary the correction for the intensities is given by:

$$\begin{aligned} \text{Flux}: \quad F_{tot} &= F_{measured} \cdot corr(morph1, morph2) \\ \text{Magnitude}: \quad M_{corr} &= M_{measured} - 2.5 \log_{10} \left(corr \left(morph1, morph2 \right) \right) \end{aligned}$$

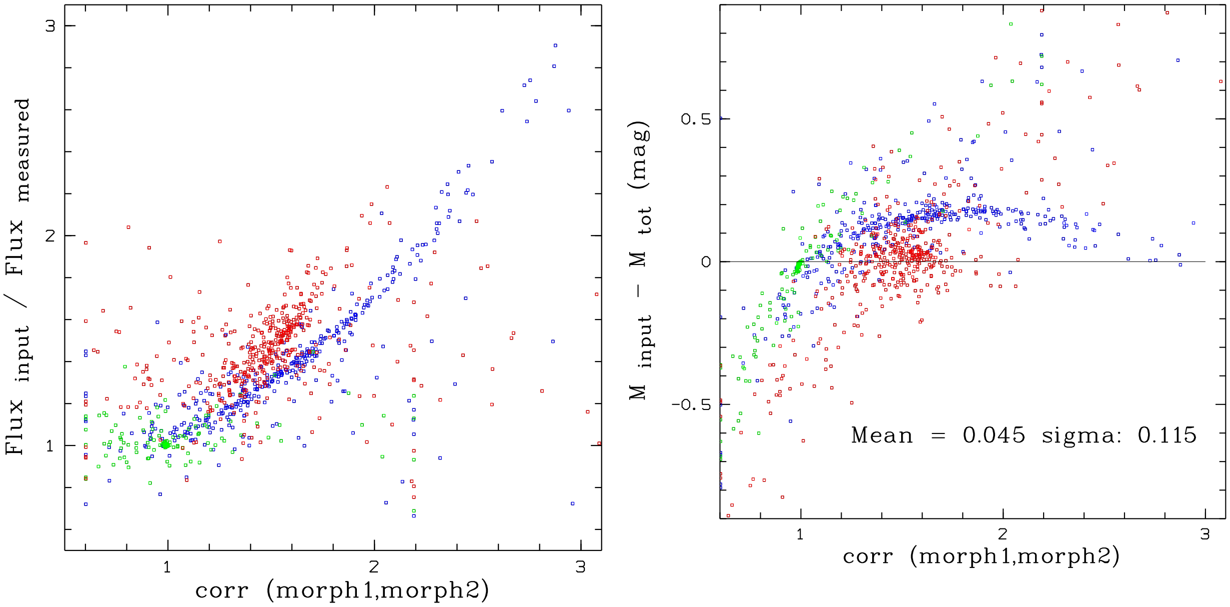

Figure 2.5: Green: stars, blue: spiral galaxies, red: elliptical galaxies
a) [left] Morphology correction function versus flux quotient
b) [right] Residual difference in magnitude between input data and CADIS measurements after aperture/morphological correction

2.2.1.1 Aperture correction in the CADIS data set

The distribution of the correction in the 12 245 classified objects (compare table 2.4) within the data sample is shown in figure 2.6a. The peak around 1 indicates that the majority of the objects are point like objects as stars, quasars and compact galaxies, which need no correction.
There are objects with a correction of less then one which would mean a downward or negative correction. This is due to the seeing and also the way morph1 and morph2 are measured by the SExtractor software.
One argument is, that in the statistical distribution, negative correction has to be applied, but we decide not to perform negative correction and use a lower limit for the correction of one, because each measured photon is real.
The largest objects in the sample are attributed a morphological correction factor of 3 in flux (corresponding to -1.6^{m}). Faint objects, which are close to the observational limit the SExtractor software can measure larger morph1 and morph2, because they are that close to the background noise. These morph1 and morph2 are not considered as real, thus the correction was restricted to a maximum factor of 3 in flux or -1.6^{m} in magnitudes.

The influence of the morphological correction on the further analysis is shown in figure 2.6b and 2.7a-c. In figure 2.6b we can see that the most luminous objects need the largest correction. Therefore the number counts (2.7a) at brighter magnitudes are more influenced by the correction than fainter ones. This is because luminous foreground objects have the

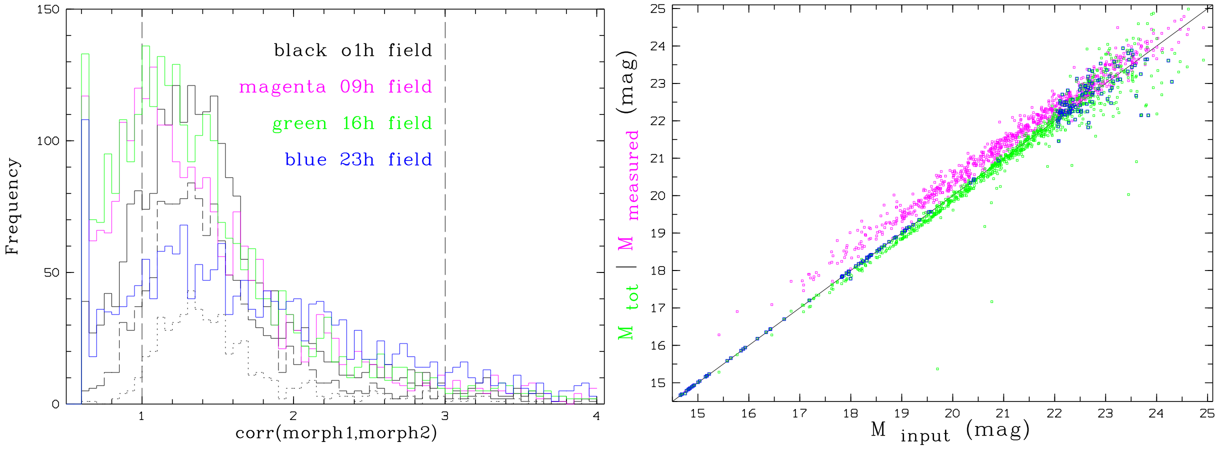

Figure 2.6: a) [left] Histogram of the correction of galaxies in the four used CADIS fields with lower and upper limit of the correction (for 1h–field black solid line all objects; dashed line $M_B < 23^m$; dotted line $M_B < 22^m$)
b) [right] Correction as function of magnitude (before correction magenta; after the correction green; and in blue stars with almost no correction)

largest morph1 and morph2. These objects have the highest correction factor and thus their magnitude changes are the most.
The slope in the corrected number counts is in agreement with the literature as we will discuss in section 2.2.3.2, which is a confirmation for the derived aperture correction.
In figure 2.7b a luminosity function with and without morphological correction is plotted, with its error ellipses shown in figure 2.7c. It can be seen that the luminosity function has become 1.5^m brighter at the bright end, while the slope at the faint end has remained unchanged. This is not surprising, because bright galaxies need large corrections. We can see that we would incorporate a major error, if we did not use an aperture correction before calculating the luminosity function.

2.2.2 Rest frame / absolute magnitude

To derive information from the observed galaxy sample, a standardized luminosity has to be defined. This is the real or rest frame or absolute luminosity, an object would have, if it was placed at a distance of 10 pc.

Many efforts have been made in the past to calculate absolute luminosity of observed objects. The problem is that emitted blue light from a galaxy is observed as red light depending on the redshift of the object. This shifting of the wavelength is due to the expansion of space. Edwin Hubble discovered the relation of redshift to distance in 1926. The absolute flux of an object can be calculated with the measurements of the distance or redshift. One problem that arises is, that the observed blue flux is based on the emitted ultraviolet fluxes of the object. Depending on a more or less steep slope of the galaxy spectrum a different correction factor for the flux has to be used. This leads to an error, if

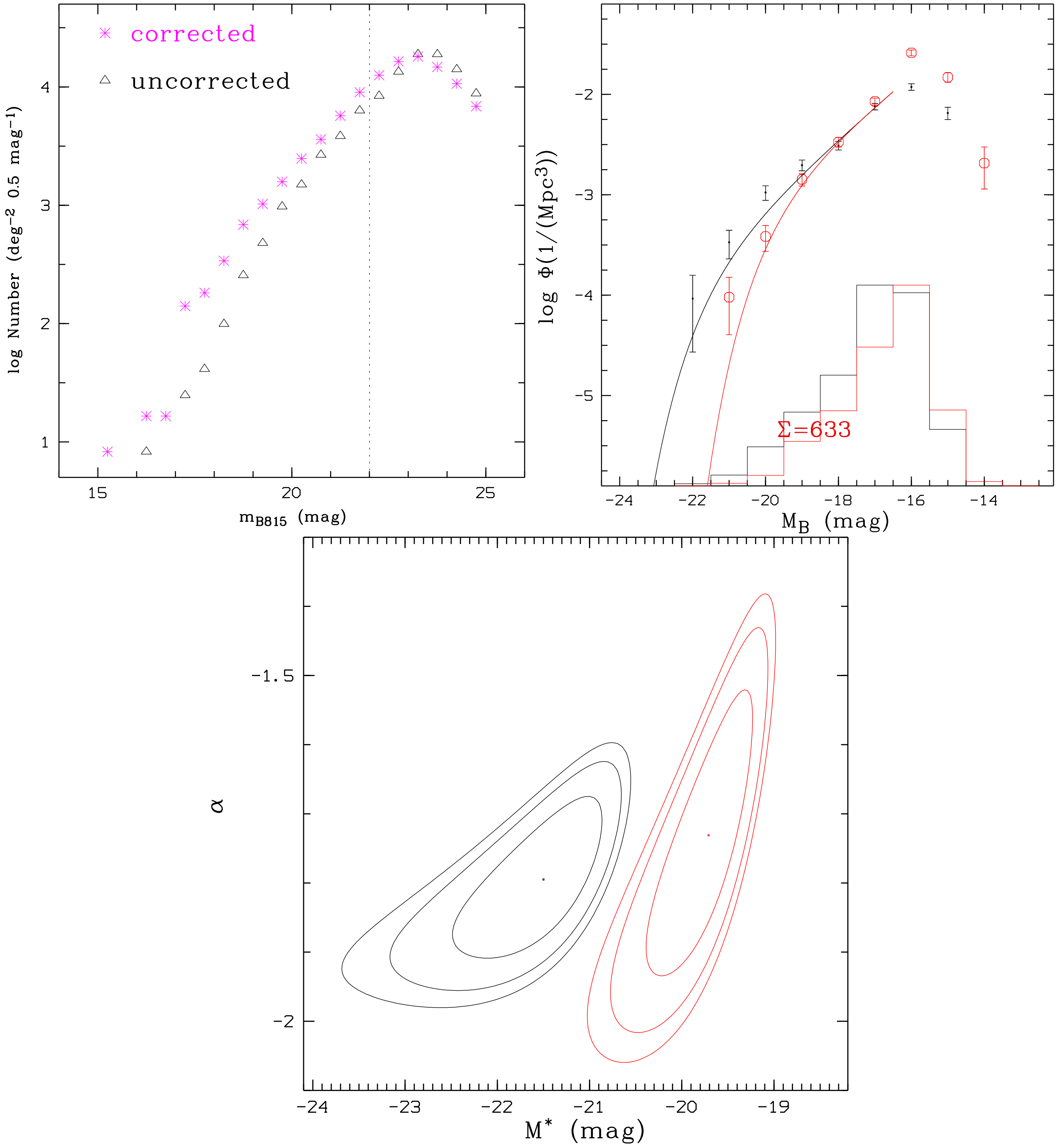

Figure 2.7: a) [left] Number counts with and without morphological correction
b) [right] Luminosity function of starburst galaxies at $0.1 < z < 0.3$ with (**black**) and without (red) morphological correction
($\phi^* = 0.00031\,1/_{\mathrm{Mpc}^3},\ M^* = -21.50^{\mathrm{m}} \pm 0.61,\ \alpha = -1.80 \pm 0.11$
$\phi^* = 0.0014\ 1/_{\mathrm{Mpc}^3},\ M^* = -19.71^{\mathrm{m}} \pm 0.43,\ \alpha = -1.73 \pm 0.23$)
c) Error ellipses of the luminosity function color coded as in b (1σ, 2σ and 3σ) detailed explanation see section 3.1.1 on page 42.

the slope of an object spectrum is not known. The luminosity correction, due to the slope of the galaxy spectrum, is generally described as a K–correction term:

$$M = m - 5\log D_l - 25 - K(z)$$

- ▷ M absolute magnitude,
- ▷ m apparent magnitude,
- ▷ D_l luminosity distance, depending on redshift z and cosmology $(H_0, q_0, \Omega_m, \Omega_\Lambda)$, e. g. [Kayser et al., 1997]
- ▷ The K(z)-correction term, is obtained from spectra simulations or local galaxies observations and has therefore large errors and uncertainties.

The large wavelength coverage of the CADIS filter set gives us the unique possibility to derive precise absolute fluxes without using any K–correction factor.
We tested two different methods for computing the absolute magnitude which will be described in the following sections.

2.2.2.1 Interpolation method for absolute magnitudes

With the large CADIS filter set we measured many fluxes points in the object spectrum. The slope of the spectrum between two measured data points can be considered as linear, because CADIS has such a good wavelength coverage with the flux measurements. With the redshifts obtained by the multi–color classification we derive the observed wavelength of the rest frame filter.
The flux value at this wavelength is calculated by linear interpolation between the measurements of the two adjacent filters. With the Vega flux of the rest frame filter, the magnitude of the object is calculated (equation 12) and corrected by the morphological correction factor from section 2.2.1.

Filter name	central wave-length (nm)	Vega flux $\left(\frac{\gamma}{m^2\,sec\,nm}\right)$	reliability limit upto B909 filter in redshift z	limit including J filter	limit including K filter
Johnson B	447.8947	$13.775 \cdot 10^7$	1.09	1.79	3.76
Johnson V	552.6235	$9.9867 \cdot 10^7$	0.70	1.16	2.85
Johnson R	687.7308	$6.9437 \cdot 10^7$	0.36	0.82	2.10
Johnson I	835.7648	$4.3747 \cdot 10^7$	0.12	0.50	1.55

Table 2.5: Used filter information and limits for interpolation

In figure 2.8 an example for the flux interpolation method is sketched. The Johnson B–filter flux for a Sb galaxy at redshift z=0.6 is interpolated to 0.272 $\gamma/(\mathrm{m}^2\,\mathrm{sec}\,\mathrm{nm})$.

In this thesis, several flux values for different filters are calculated. To derive magnitudes the filter set of Johnson and Morgan is used. This set is established in astronomy since 1951, to derive standardized results and to compare them later with results from other groups. The central wavelengths and Vega fluxes for the absolute magnitude calculation are listed in table 2.5.

For larger wavelength differences between the neighboring filters, the interpolation becomes less accurate (figure 2.8). The precision of the interpolated absolute fluxes decreases with redshift when the shifted wavelength leaves the optical wavelength. In CADIS, only two filters in the infrared range were observed. Thus, the reliability of interpolated flux values decreases when the rest frame wavelength of the computed filter reaches the B909–filter (table 2.5). Due to the larger wavelength difference of the CADIS filters in the infrared and the larger error of the J and K measurements, the corresponding derived magnitudes are more uncertain and results derived from this are less reliable. Nevertheless, interpolation we performed interpolation at higher redshift.

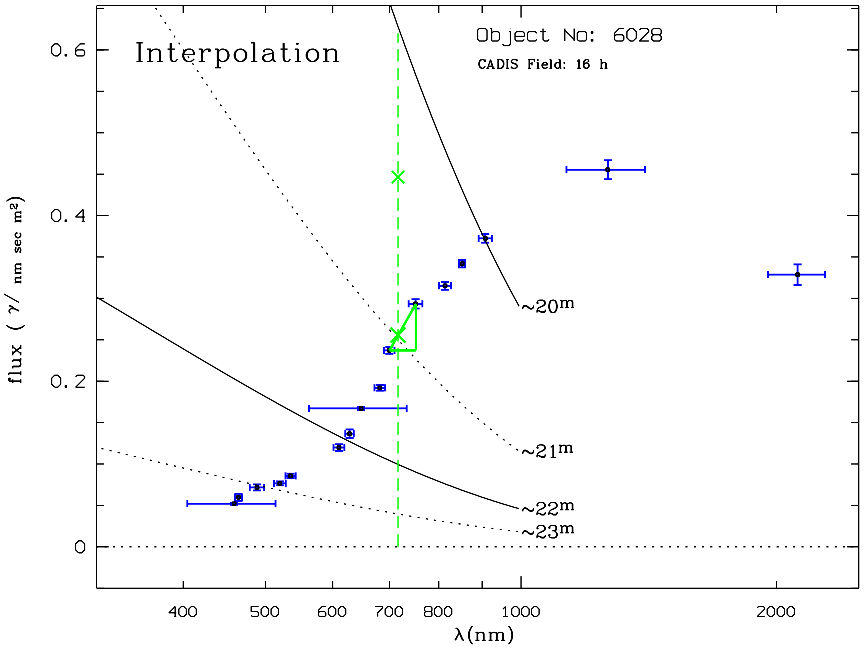

Figure 2.8: Example to derive the absolute flux for Johnson B 447 nm corresponding to 716 nm at a redshift of z = 0.60. The linear interpolation between the two adjacent filters (B700 and B752) is illustrated in green. The larger cross marked the interpolated flux position and the smaller one flux with the aperture correction. Black solid and dotted lines indicate fluxes of the same Vega magnitude ($\sim 20^{\mathrm{m}} \sim 21^{\mathrm{m}} \cdots$). They decrease to higher wavelength because the Vega spectrum is decreasing. This estimation is limited to the optical because no Vega spectrum is available for the entire infrared range.

2.2.2.2 Integration method to derive absolute magnitudes

Another way to derive the absolute fluxes is to use a template spectrum to calculate the spectrum for each object, and then determine the rest frame spectrum by folding it with the filter curve.

The multi–color classification assigns every object a most probable spectrum. In the case of galaxies, those spectra are characterized by a redshift z (0.00-2.00) and an SED (0-100) (compare section 2.1 and [Wolf et al., 2001]). We derive an object spectrum by linear interpolation of the two Kinney spectra, which are most similar to the object spectrum. We normalize this spectrum with respect to all but one filter measurement. The filter with the largest discrepancy of the spectrum is not taken into account. Thus, the best fitting spectrum can be found for each object.
By folding the spectrum with a filter curve, the flux in this filter can be derived. With the Vega flux noted in table 2.5, the absolute magnitude is then calculated. This procedure is illustrated in figure 2.9 schematically.

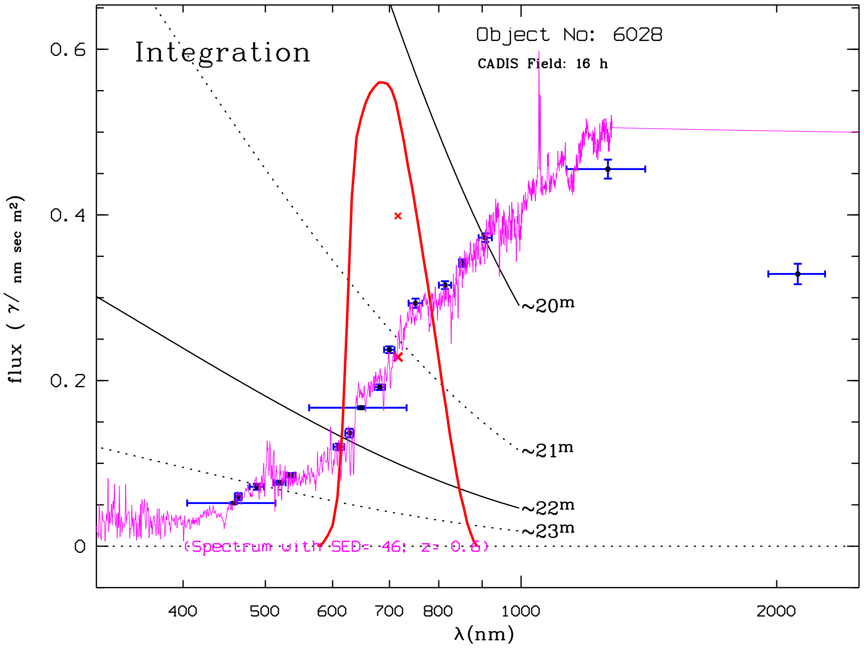

Figure 2.9: Flux integration to derive the absolute flux in the Johnson B Filter (448nm) from the matched spectrum of a multi–color classified object. The SED–type for the template spectrum used is 46, and the redshift is $z = 0.06$. The solid red line illustrates the filter transmission curve, while the big red dot represents the integrated flux value and the small one the aperture corrected flux value. (Further explanations in figure 2.8)

2.2.2.3 Comparison of the two methods for calculating the absolute magnitude

As shown in figure 2.10, the difference in absolute magnitude as derived from the two methods of integration and interpolation is not zero for most of the observed galaxies. The differences show a statistical distribution around zero. For 68% of the objects the difference is less than $\pm 0.5^{\mathrm{m}}$. A difference of more than 1.2^{m} is found in rare cases.
In figure 2.11a and b two examples of spectra are plotted with large discrepancies between interpolated and integrated magnitude. This difference are in most cases due to filter measurements, which are inconsistent with the fitted continuum spectrum. It can be due to emission lines or data reduction problems e. g. cosmic rays. In the data sample the amount of objects with such differences is less than 1%.
To decide which absolute magnitude to use, we summarize the advantages and disadvantages of each method:

Absolute magnitude from interpolation	**Absolute magnitude from integration**
+ not dependent on a template spectrum	+ spectrum gives precise information over the whole range of the filter. Measurements are independent of local abnormality of the spectra, because of intensive lines close to the filter
+ measured infrared observations are directly included into the interpolation of the absolute flux	+ suitable over a wider range in redshift, because it is independent from the measuered filter set
+ faster to calculate	
− dependent on emission lines falling into the neighboring filters	− Kinney spectra are the only templates used, unknown spectral distributions have not been taken into account
	− worse infrared extrapolation in the template spectrum, influence of the spectrum used on SED and intensity
	− longer calculation (factor 50)

Given the lower influence by template spectra and the danger of a large discrepancy between fitted spectrum and observed filter values, the decision was made, that the interpolated absolute magnitude is more reliable. This method will therefore be used in the rest of this work whenever possible.

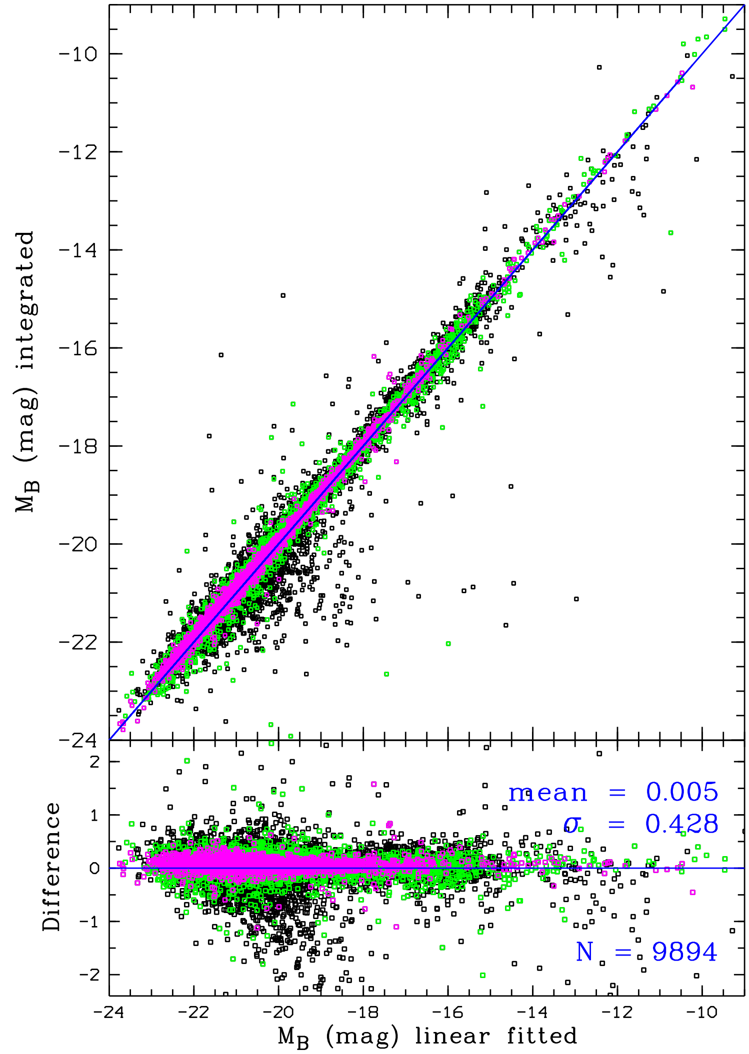

Figure 2.10: Comparing absolute magnitude from interpolation and integration; **faint objects black** $23^m < \mathbf{m}_{B815}$; green $22^m < m_{B815} < 23^m$; bright objects magenta $m_{B815} < 22^m$; Mean and standard deviation are measured for the whole object sample

2.2.2.4 Influence of different absolute magnitudes on further analysis

In figure 2.12 a set of luminosity functions with interpolated and integrated magnitudes is plotted. The influence on a luminosity function of galaxies is small concerning the M^* parameter[2]. The faint end of the function is increasing and the α parameter[2] is decreasing,

---

[2] Detailed explanation for the parameter $M^*$and α are given in section 3.1.1 on page 42

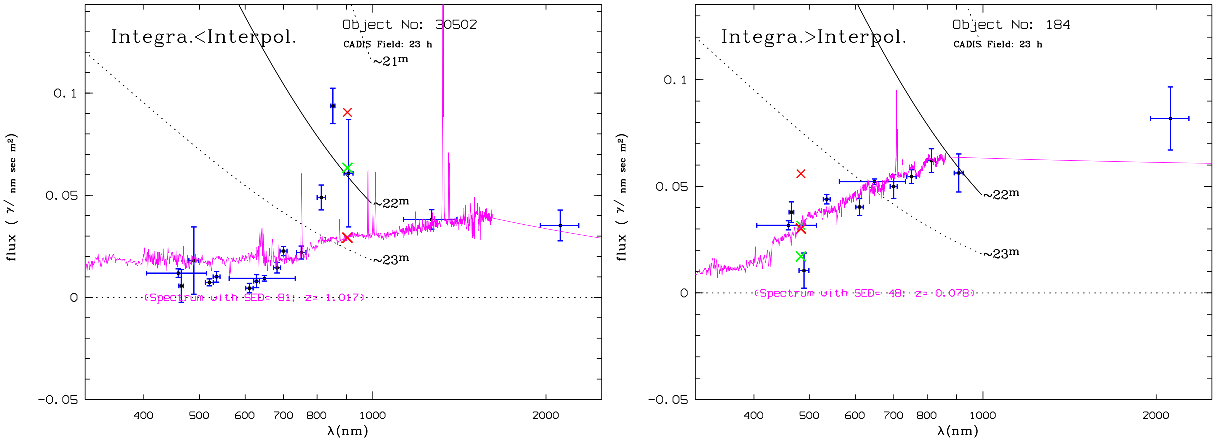

Figure 2.11: Two example spectra with large discrepancies of the interpolated fluxes (green) and the integrated fluxes (red)
a) [left] Interpolated flux exceeds integrated flux
b) [right] Integrated flux exceeds interpolated flux
(Further explanations in figure 2.8 and 2.9)

because the integration method tends to eliminate background noise for faint objects and overestimates their luminosity.
With less objects in the subsample, the influence rises. But in the case of larger samples the difference is small, which is mostly the case in this work.

2.2.3 Limits of the CADIS data sample

2.2.3.1 Field galaxy selection

The CADIS fields were selected to avoid galaxy clusters (see section 2.1). Nevertheless there may still be unknown clusters in the field. Before analyzing field galaxies, obvious cluster contamination has to be excluded.
By inspecting the data set no larger accumulation in redshift space or real space could be found (compare example figure 2.13).

2.2.3.2 Number counts

The limiting magnitude of the observation in one filter can be derived from the number counts in that filter. The cut–off from a linear slope of the logarithm of the number counts shows the completeness limit of the observation in that filter. In figure 2.14a the differential number counts of the classified extragalactic objects in the CADIS *complete area* (compare page 11) are plotted. From the number counts plot (figure 2.14a) we can see almost 100% completeness down to $m_{B815} = 22^{\mathrm{m}}$. The slope in the range from $17^{\mathrm{m}} < m_{B815} < 22^{\mathrm{m}}$ is determined as 0.4094 ±0.014. This is in agreement to the literature

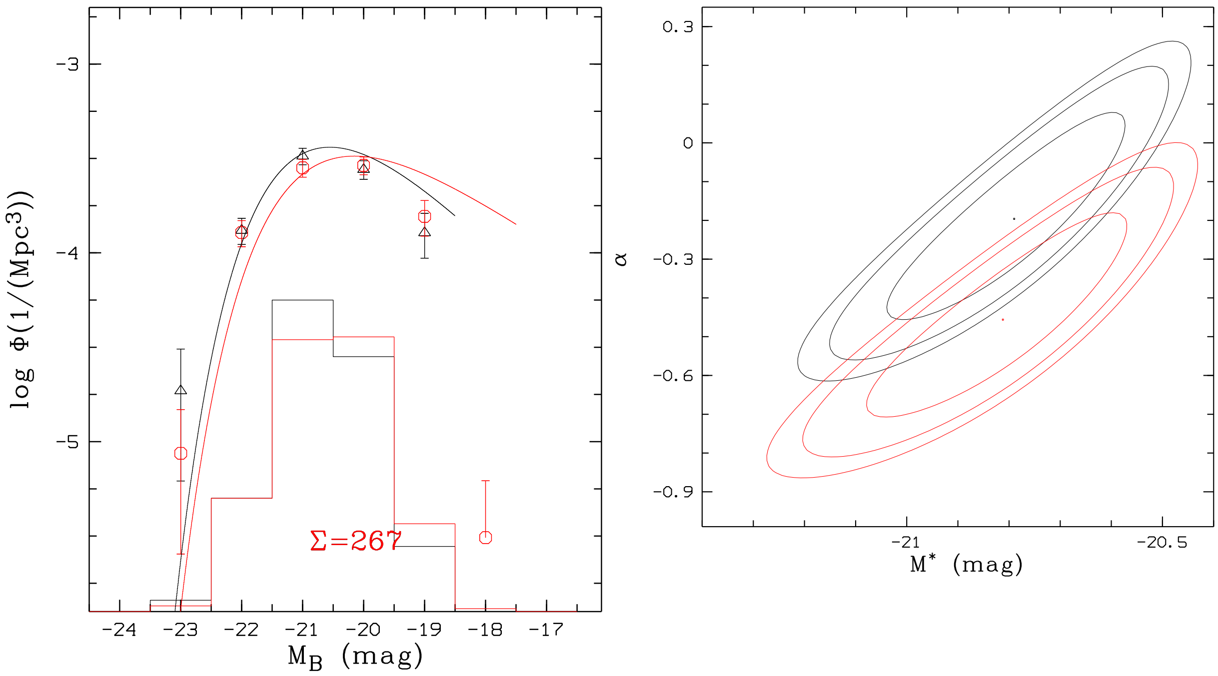

Figure 2.12: a) [left] Luminosity function of starburst galaxies at $0.75 < z < 1.1$ with interpolated absolute magnitudes (**black**) and integrated absolute magnitudes (red)
($\phi^* = 0.00072\,1/_{\mathrm{Mpc}^3},\ M^* = -20.79^{\mathrm{m}} \pm 0.23,\ \alpha = -0.196 \pm 0.19$
$\phi^* = 0.00053\,1/_{\mathrm{Mpc}^3},\ M^* = -20.91^{\mathrm{m}} \pm 0.23,\ \alpha = -0.456 \pm 0.28$)
b) Error ellipses of the luminosity function.
Detailed explanation are given in section 3.1.1 on page 42

(compare [Nonino et al., 1999, Fried et al., 2001]). The number counts in the 4 fields are comparable (figure 2.14b) and we can conclude that the data set has a homogenous quality.

2.2.3.3 Observational limits

In this section an exact observational limit of the CADIS data set will be determined. To motivate this we first investigate the influence of the observational limit on the further analysis.

The most critical parameter for the resulting luminosity function is the observational limit of the data set. This is illustrated in figure 2.15c, where a luminosity function is plotted out of a simulated galaxy sample. The figure shows that the data points of the luminosity function at the faint end depends on the observational limit (different colors denote analysis with different observational limits). This is due to the fact, that the observational limit is limiting the observed volume and thus changes the density of objects.
The parameters for the faint end of the Schechter function (α parameter[3]) is significantly influenced by small changes in the observational limits. For further details see section 3.1.1.

---

[3] Detailed explanation for the parameter α is given in section 3.1.1 on page 42

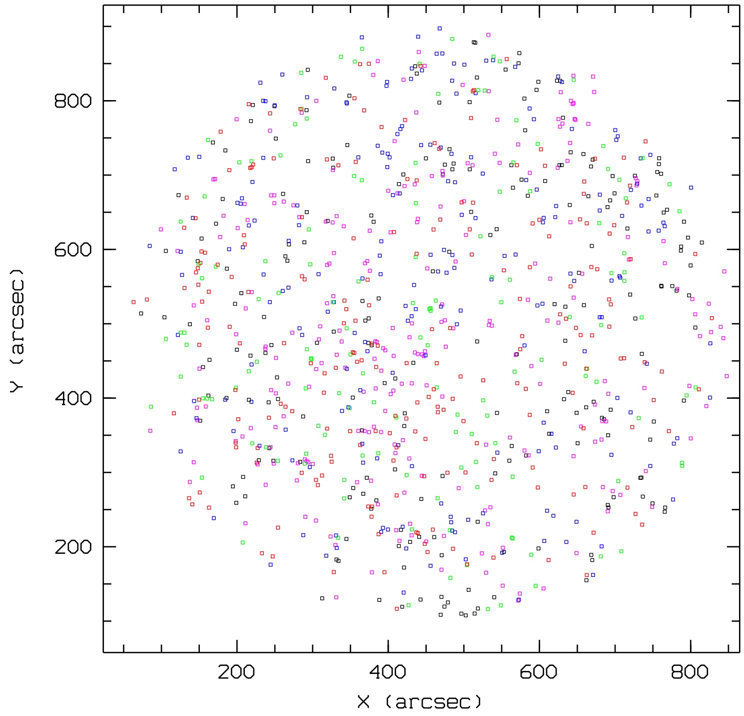

Figure 2.13: 16h field distribution of CADIS galaxies in slices
(**black: $0.4 < z < 0.5$**, magenta: $0.5 < z < 0.6$, blue: $0.6 < z < 0.7$, green: $0.7 < z < 0.8$, red: $0.8 < z < 0.9$)

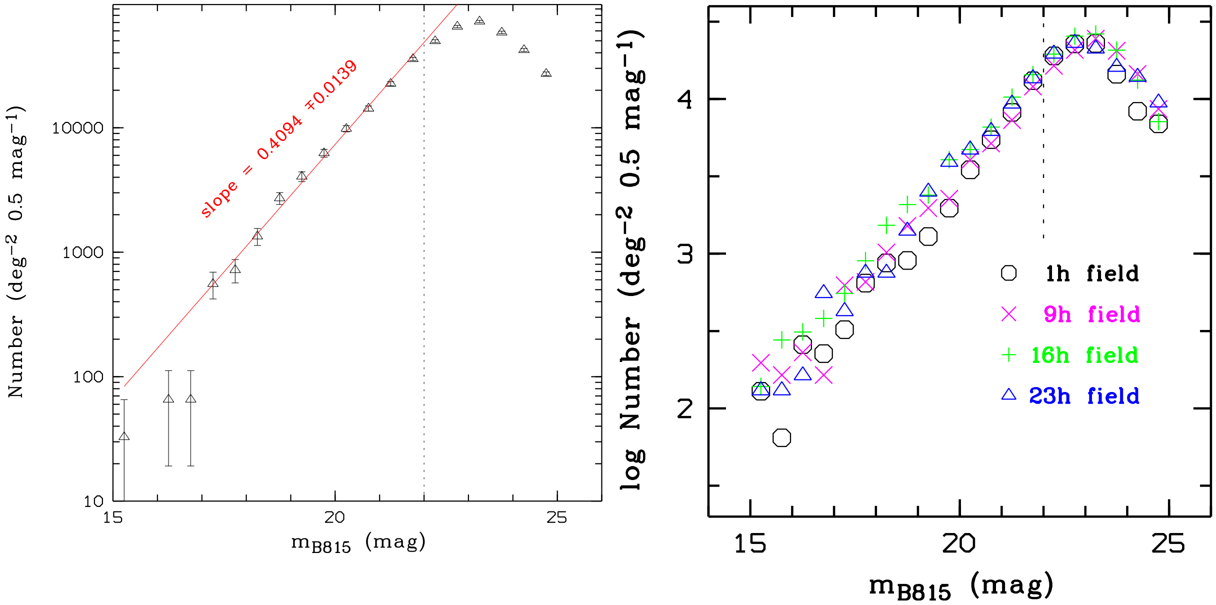

Figure 2.14: a) [left] Number counts of classified galaxies and quasars in CADIS (complete center area)
b) [right] Field variation in CADIS number counts

But therefore this it is very important to calculate a precise observational limit of the data sample. This motivates the efforts described in the following paragraphs to derive this limit for the CADIS data set.

In CADIS it is not straight forward to set an observational limit. One reason is that the observational depth in flux varies with filter and field (compare table 2.3). But this is only one factor that influences the observational limit. It is also influenced by different slopes of the rest frame spectra of the observed objects, the different observed redshifts, and the limits of the classification procedure. This leads in a multi–parametric problem.

Figure 2.16 shows two examples of the inhomogeneity of the detection limit. In this figure is shown a test by simulation down to which luminosity a galaxy can be detected. In the case of a S0 galaxy, the apparent limit is lower for objects with low redshifts (figure 2.16a), while for starburst 4 galaxies it remains relatively constant at all redshifts.

Another effect observed at the observational limit is shown in the figures 2.15a and b. Here two galaxies were analyzed with decreasing apparent magnitude (coded in color). After assigning an absolute magnitude we obtained the distribution in the M–z plane[4], plotted in the figures. In the case of a S0 galaxy at low redshifts, we can see that the redshift of the object tends to get overestimated and congruously the absolute magnitude gets overestimated. In the case of a starburst galaxy at high redshift, we observe the opposite behavior (figure 2.15b). This is a general trend for galaxies at higher redshift.
This is affecting the observational limit as well as the completeness of the observed objects. We analyze the completeness in section 3.1 on page 47 in detail. Here we first estimate an observational limit.

We mentioned the complexity of the problem, so the exact way of deriving an observational limit are simulations. Thus, every object in the data set has different parameters and thus an individual observational limit for each object has to be determined by simulations. A Monte Carlo method to derive the observational limit was developed and applied in the analysis described in the rest of this thesis.

To find the observational limit, each object was simulated individually because of its special filter measurements. This will be important for further data analysis. The procedure for every galaxy in the data set was the following:

- ▷ 1000 homogeneous distributed apparent magnitudes were generated for filter B815 between 22.25^{m} and 24.25^{m}. These limits were chosen, because 95% of the observational limits fall within this range.
- ▷ Using the CD–filter indices of the original object, the apparent magnitude and the other filter–fluxes were calculated in the the Vega flux in the individual filter.
- ▷ The apparent magnitude errors were calculated according to the used field. This depends on the 5σ observational limit of each filter in the specific field (details see section below) .

---

[4] Mz–diagram: redshift z plotted versus absolute magnitude M (for Johnson B)

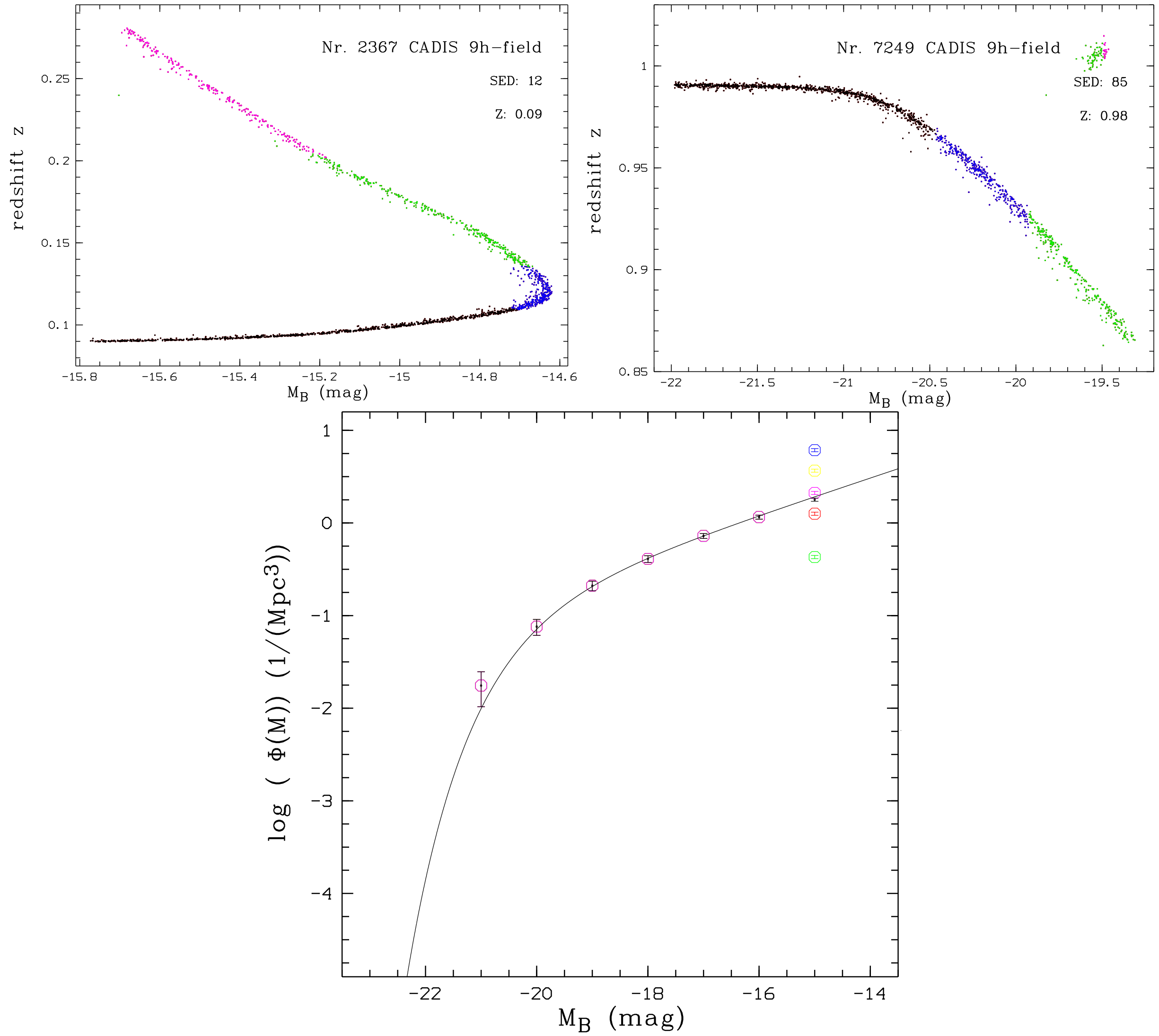

Figure 2.15: a) [top left] M–z diagram of a Monte Carlo simulated S_0 galaxy sample (SED = 12, z = 0.09)
For a and b black: $m_{B815} < 22.5^{m}$, blue: $22.5^{m} < m_{B815} < 23.0^{m}$, green: $23.0^{m} < m_{B815} < 23.5^{m}$, magenta: $23.5^{m} < m_{B815}$
b) [top right] M–z diagram of a Monte Carlo simulated starburst galaxy sample (SED 85) at z= 0.98, color coded as in a
c) [bottom] Influence of different observational limits on the calculation of the luminosity function (observational limit = magenta: $m_{B815} = 24.45^{m}$, black: $m_{B815} = 24.35^{m}$, yellow: $m_{B815} = 24.33^{m}$, blue: $m_{B815} = 24.30^{m}$, green: $m_{B815} = 24.28^{m}$, red: $m_{B815} = 24.23^{m}$)

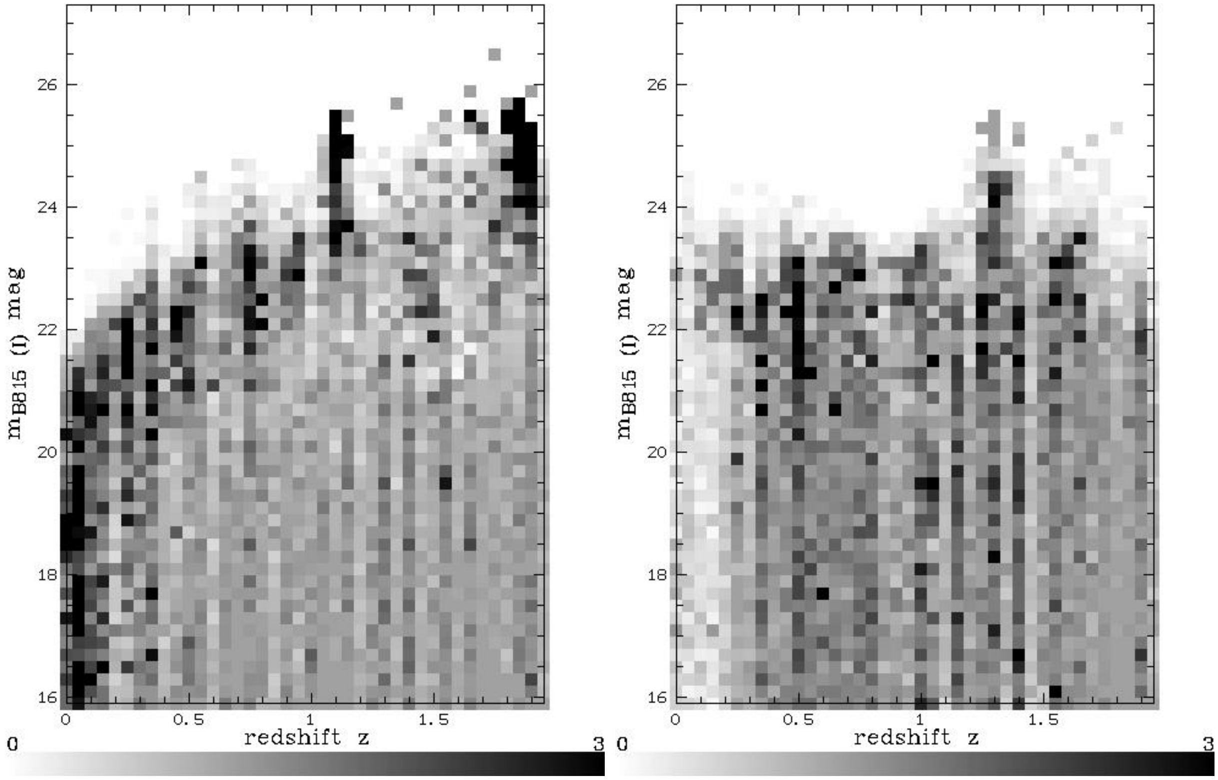

Figure 2.16: a) [left] Observational limit of simulated S0–galaxies (SED 15) $m_{\mathrm{B815}}(z)$
b) [right] Observational limit of simulated starburst4–galaxies (SED 85) $m_{\mathrm{B815}}(z)$
Coded from 0 (white = no galaxy is classified in that SED, m, z – bin) to 3 (black = three or more times as many galaxies where classified in that SED, m, z – bin) as simulated in that bin.

- ▷ The apparent magnitudes were scattered using the calculated apparent magnitude errors.
- ▷ New CD–filter indices were calculated from the apparent magnitudes.
- ▷ This set of simulated objects was classified by the multi–color classification scheme.
- ▷ The apparent magnitude (in I = B815) was determined, at which the classification catches less than 1σ (63%) of the objects.
- ▷ For this apparent magnitude limit the absolute magnitude in Johnson B was derived via the interpolation method from section 2.2.2.1.
- ▷ The morphological correction factor of the real object was taken into account for this absolute magnitude calculation.

- ▷ In case when the 1σ limit not is not in the chosen magnitude range ($22.25^{\mathrm{m}} < \mathrm{m_{B815}} < 24.25^{\mathrm{m}}$), a brighter or fainter sample was taken and the procedure was repeated.

It is not taken into account that the classified redshift or classified SED of the simulated objects do not match with the input every time. This problem is due to the fact that some filter measurements disappear in the background noise sooner than others before an object becomes totally unclassifiable. In figures 2.15a and b this problem is illustrated. As those scattered objects appear also in the real data set, we have to take a correction into account. This will be done when the completeness of the data sample is discussed in section 3.1 on page 47.

Due to the fact that the derived observational limit is a 63% completeness definition, the statistics allow that the magnitude limit is brighter than the actually observed galaxy. Therefore this galaxy belongs to the remaining 37% beyond the set limit. In this case the limiting magnitude is set equal to the observed magnitude of that object.

Observed or apparent magnitude error

At this point, an explanation of the errors in the simulations of CADIS data is given. We introduced into the analysis a more realistic error scattering than in all CADIS analyzes before.

The error can be calculated as:

$$\sigma_{m_i} = 0.1 \cdot 10^{0.4\left(m_i - m_{i_{lim}}\right)}$$

This gives the smallest error in the filter i, depending on the luminosity m_i of the object and $m_{i_{lim}}$ the 5σ detection limit of that filter (magenta line in figure 2.17b). As found in figure 2.17a, the real distribution of the error is underestimated. We used a randomly logarithmic distribution (ϵ_{log}) of the difference between the minimal errors and an estimated maximal error:

$$\sigma_{m_{if}} = 0.1 \cdot 10^{0.4\left(m_i - m_{i_{lim\,field}}\right) + \epsilon_{\mathrm{log}}/100 \cdot 0.1 \cdot 10^{0.4\left(m_i - m_{i_{lim\,field} - 1.5} + 0.03\right)}}$$

- ▷ ϵ_{log} a logarithmic random distribution between 0 and 100
- ▷ $m_{i_{lim\,field}}$ the real observational limit in the filter i within the observed field.

This distribution gives a good estimation of the observed error derived by CADIS photometry, as can be seen in figure 2.17b (black dots).

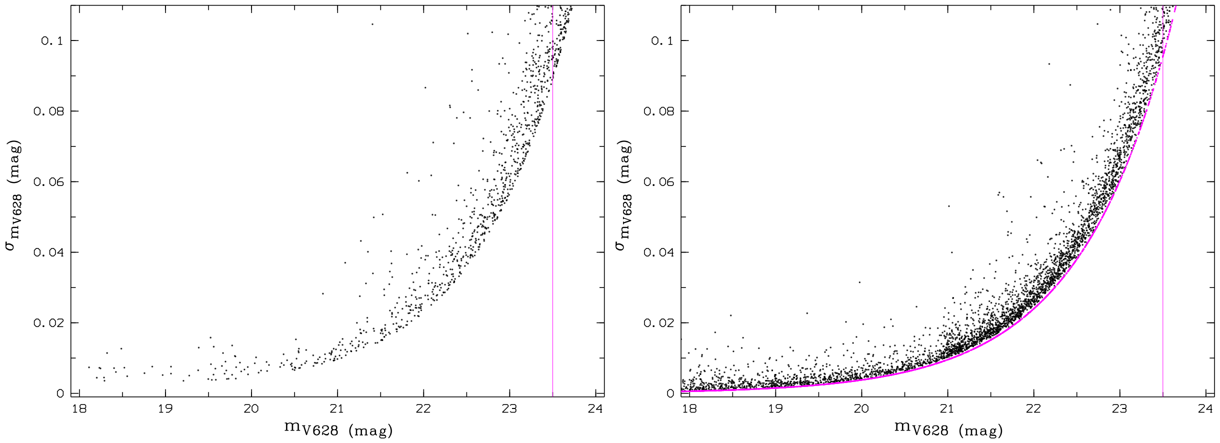

Figure 2.17: a) [left] Magnitude error in a real CADIS filter with 5σ detection limit (magenta vertical line indicates the observational limit)
b) [right] Magenta: simulated magnitude error as used before; black: as developed in this work

2.2.3.4 Error due to the morphological correction

As shown in the simulation of the morphology correction (compare figure 2.5 and 2.6), we introduce an error into the magnitude based on to the morphological correction, in addition to the measurement error. This is due to the fact that morphology correction is a best fit compromise. The morphological parameters are derived in CADIS from the frame with the best signal to noise ratio. There is no error estimation concerning the morphology, so that an error of about $\pm 0.2^{\mathrm{m}}$ is unavoidable (figure 2.5) and propagates into the measurements of the absolute magnitudes.

In CADIS we work with a high number of objects, that resulting errors should be small because of statistics. Minimization of the individual errors in the measurements is of secondary importance for our purpose.

2.2.3.5 Multi–color classification and accuracy

The information that will be derived from the data sample in this work, is directly or indirectly based on the multi–color classification. Thus, we have here a closer look on this central piece of the CADIS data reduction procedure (section 2.1). As described by Wolf et al., the multi–color classification has been checked by comparing multi-color redshifts with spectroscopic redshifts [Wolf et al., 2001]. It is tested with 160 multi– and long slit spectra in the CADIS fields. The classified objects contain 98 galaxies to compare the photometric with the spectroscopic redshift. The distribution is plotted in figure 2.18. The difference between the two determined redshifts shows a standard deviation of $\sigma_{\Delta z} = 0.15$. The obvious misclassifications are eliminated by excluding objects outside the gaussian distribution. Then a standard deviation of $\sigma_{\Delta z} = 0.07$ can be found. This still small sample is at the moment the only confirmation of the classification.

When inspecting the error of the absolute magnitude, we describe its dependence on z (section 2.2.2.3), but also on the measurements of the neighboring filters at the shifted wavelengths. The interpolation of the filter errors can give us an estimate of the magnitude error and the multi–color classification and an error in redshift z, so that it would be possible to calculate a combined error. But the folding function is not trivial and depends on many other assumptions (for instance on z and SED errors etc.). A better way is to simulate an ensemble of galaxies with the same measurement errors, and to calculate the redshift and absolute magnitude error from their statistical distribution within this sample. In detail the procedure for each observed object is as follows:

- ▷ The apparent magnitudes and apparent magnitude errors of each object were taken (only the really measured filters).
- ▷ 100 objects with gaussian scattered apparent magnitudes were generated according to the apparent magnitude errors.
- ▷ New CD–filter indices were calculated from the absolute magnitudes.
- ▷ The set of simulated objects was multi–color classified.
- ▷ The absolute magnitude was calculated with the interpolation method described in section 2.2.2.
- ▷ Obvious misclassifications were eliminated according to 3σ error from the CADIS error in z.
- ▷ The errors in the redshift z and in the absolute magnitude were calculated by the standard deviation of this sample of similar objects.

In figure 2.19 a simulated set of scattered objects is shown. In figure 2.20 we give an overview of the distribution of the errors and thus an impression of the accuracy of the available data set and the dependency of the observed magnitude in the B815 filter (similar to I) and the uncertainties.

In the following analysis we have used binnings, which exceed these errors when we subdivide our data set.

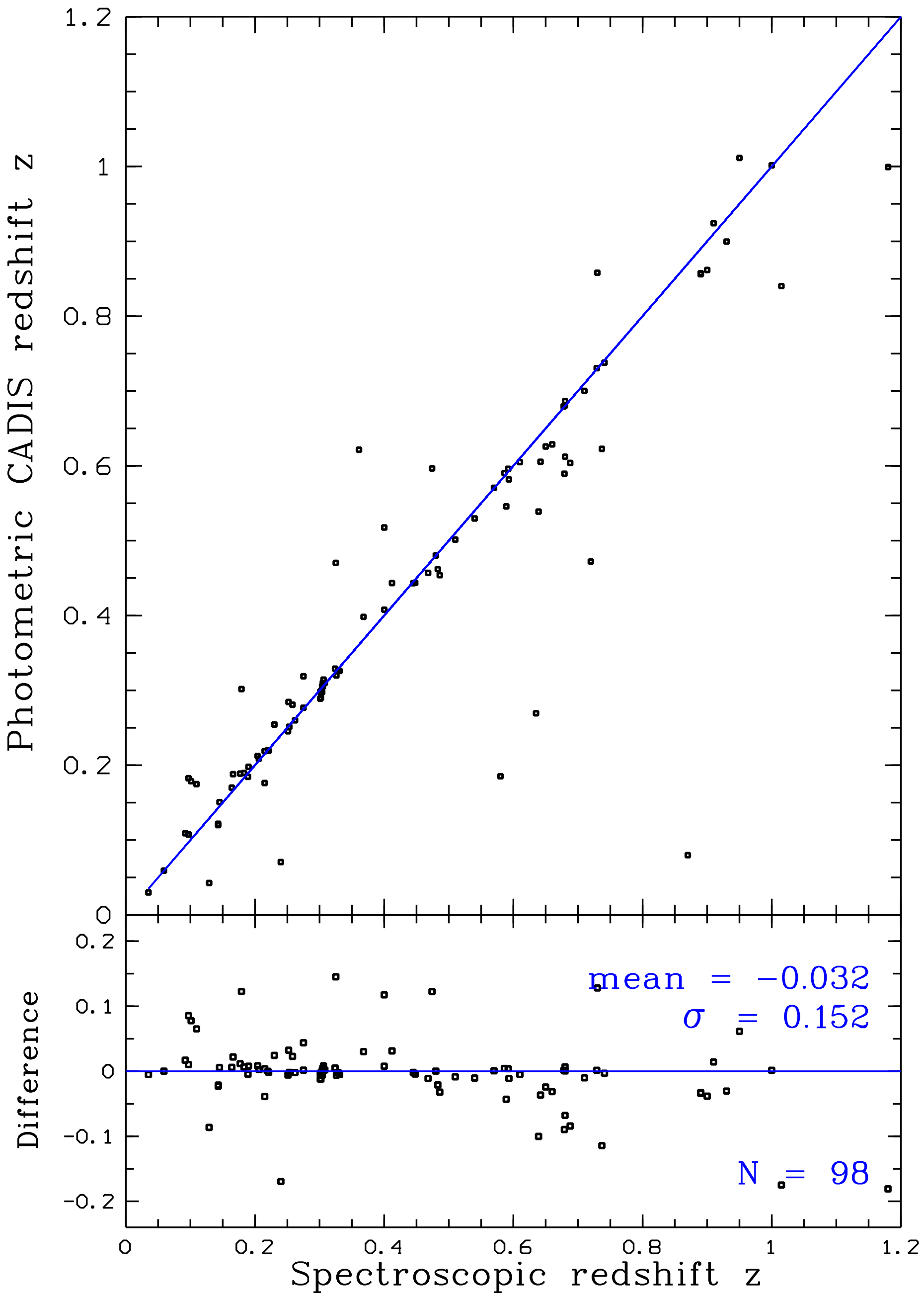

Figure 2.18: Quality of classification by spectroscopical verification is tested by comparing spectroscopic and photometric redshift

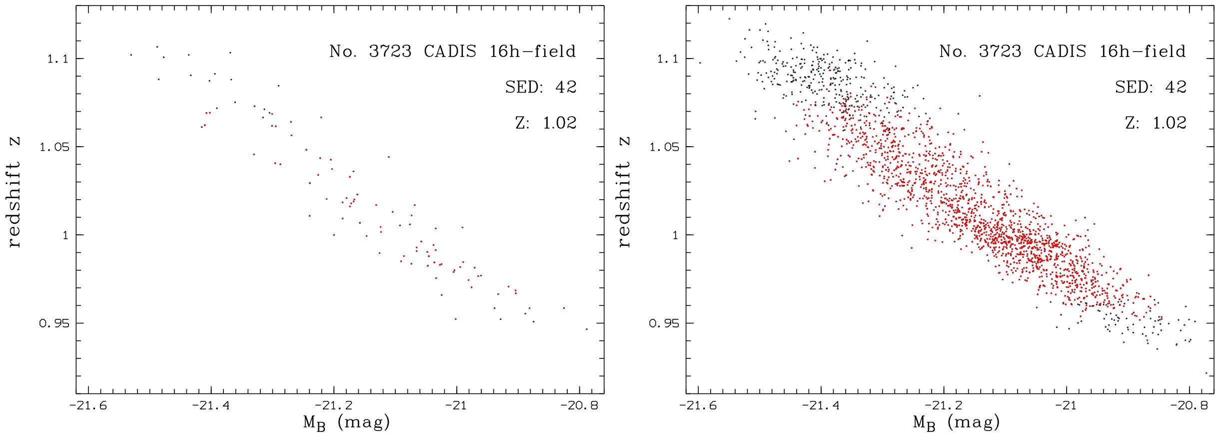

Figure 2.19: Simulated objects in M–z diagram; red objects are within the multi–color classification error

a) [right] 100 objects used for deriving error in z and absolute magnitude

b) [left] Statistics of 2000 simulated objects

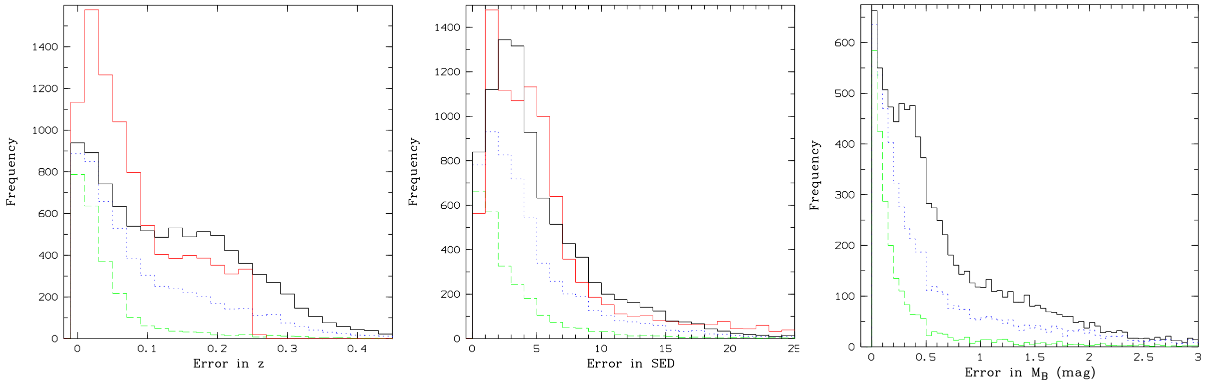

Figure 2.20: Simulated error in the CADIS data set

Black = simulated error of all objects; blue = simulated error of objects brighter then 23^{m}; green = simulated error of objects brighter then 22^{m}; red = error derived form the multi–color classification

a) [left] Distribution of errors in the redshift z

b) [center] Distribution of errors in spectral energy distribution (SED)

c) [right] Distribution of errors in the absolute magnitude in Johnson-B

2.2.3.6 Redshift limit

The gained CADIS galaxies sample is summarized in the M–z diagram (figure 2.21).

A few words on the minimal redshift are appropriate here. At low redshifts the numbers of objects are low, because of the pencil beam construction of the survey (compare section 2.1). The criteria of choosing dark regions (fainter than 16^{m}) additionally eliminates bright objects in the low redshift range. Thus, most of the conclusions derived in chapter 3 have larger error bars at lower redshift. The completeness of the data adds further limitations on the results. This can easily be seen in the summarized M–z diagrams (figure 2.21) of the galaxy data set in CADIS.
The upper limit for interpretation is given by the luminosity of the objects. At redshifts above 1.2 90% of the object are below $m < 23$. We can see in the number count diagram 2.14 that in that range the detection is not anymore complete. Additionally the confirmation of the multi–color classification is never tested with spectra above z > 1.2. Thus, in redshifts above 1.2 all interpretations have to be inspected critically and have a lower confidence level.

Another aspect to mention is the *focusing* effects in z in the M–z plot (figure 2.21). Focusing in that context means, that at some redshifts objects are accumulated and other bins are underrepresented. Other surveys also suffer from this effect [Carlberg et al., 2000].
Some are filaments in the universe structure. Those are canceled out by different CADIS–fields in the M–z diagram (figure 2.21). Other redshift bins are overcrowded in all fields M–z diagrams. This can be due to classification effects. We will take care of this by a completeness correction in section 3.1.1.4 on page 47.
More analyzed CADIS–fields can give in the future further conclusions whether those features are real or artificial.

2.3 CADIS galaxy data set and other survey samples

There are many large scale surveys currently undertaken or completed (2dFGRS[5], CfA[6], Durham/UKST[7], ESP[8], LCRS[9], RSA[10], SDSS[11]), but they only reach into the local universe ($z < 0.1$).
In the medium redshift range ($0.1 < z < 1.5$) there are only three comparable surveys:

- ▷ The **C**anadian **N**etwork for **O**bservational **C**osmology field galaxy redshift survey **CNOC2** [Lin et al., 1999] has an imaging area of 1.55 square degree down to a

---

[5] Two Degree Field system (2dF) Galaxy Redshift Survey (http://www.mso.anu.edu.au/2dFGRS/)
[6] CfA Redshift Survey
[7] Durham/UKST Galaxy Redshift Survey
[8] The European Southern Observatory (ESO) Slice Project (http://boas5.bo.astro.it/~cappi/esokp.html)
[9] Las Campanas Redshift Survey (http://manaslu.astro.utoronto.ca/~lin/lcrs.html)
[10] Revised Shapley-Ames Catalog of Bright Galaxies
[11] Sloan Digital Sky Survey (http://www-sdss.fnal.gov:8000/)

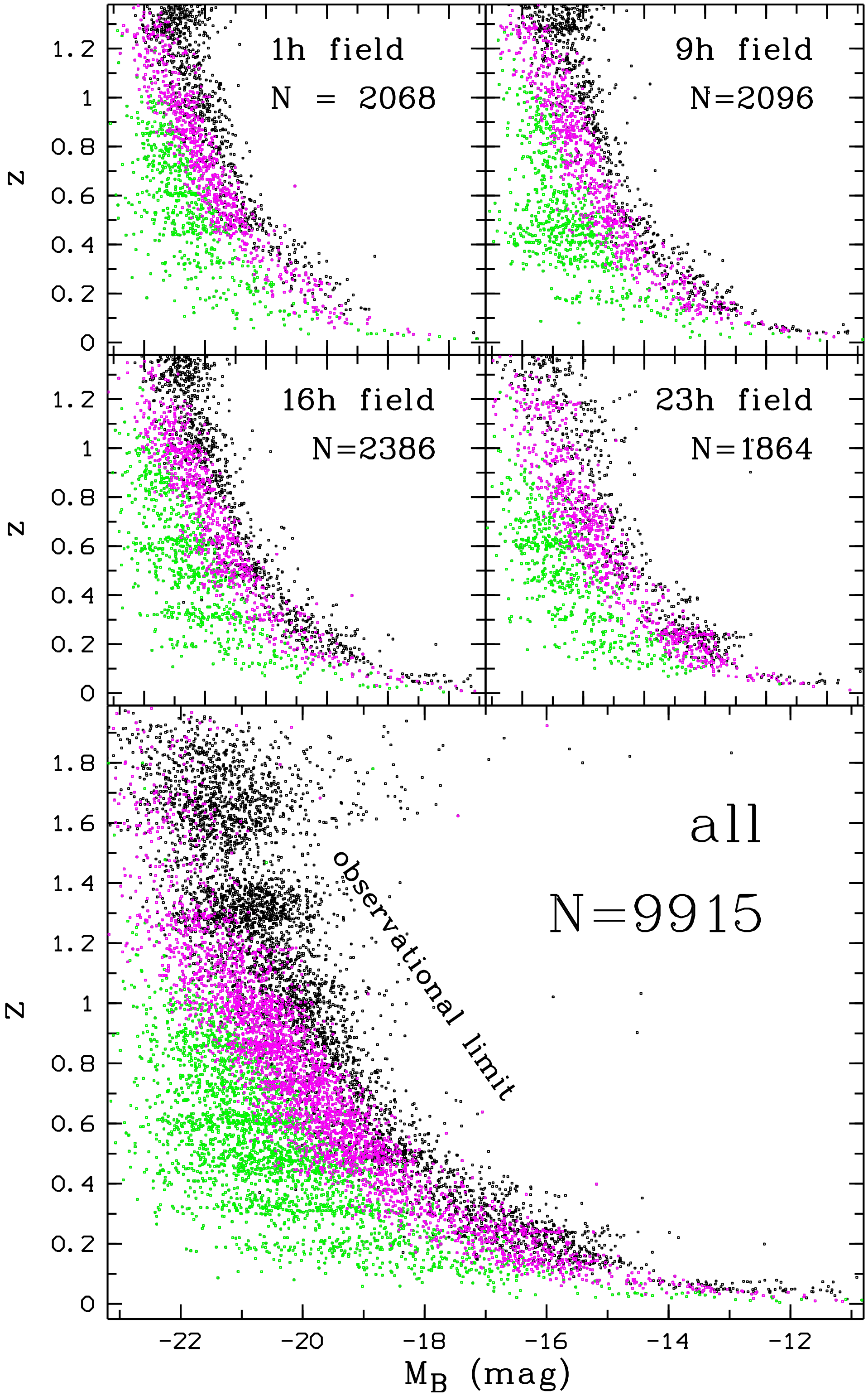

Figure 2.21: M–z diagram of galaxies in the CADIS fields
faint objects black $23^{\mathrm{m}} < \mathbf{m}_{\mathrm{B815}}$; green $22^{\mathrm{m}} < \mathrm{m}_{\mathrm{B815}} < 23^{\mathrm{m}}$; bright objects magenta $\mathrm{m}_{\mathrm{B815}} < 22^{\mathrm{m}}$
(a-d) [top and middle, left and right] M–z diagram for 4 CADIS–Fields (1h, 9h, 16h and 23h) limited to redshift $z = 1.4$
e) [bottom center] M–z diagram for all current CADIS galaxy detections

limiting magnitude of $m_{\mathrm{R}} = 21.5^{\mathrm{m}}$.
10 000 photometric classifications and 2000 spectra were taken, up to redshifts of 0.55. The survey is mainly designed to study clustering effects and differs in the selection of the fields from CADIS [Carlberg et al., 2000].

- ▷ The **Autofib** redshift survey of Ellis et al. observed galaxies with $11.5^{\mathrm{m}} < \mathrm{b_J} < 24.0^{\mathrm{m}}$and has taken spectra of 1700 objects. The survey extends to a redshift of z = 0.75 [Ellis et al., 1996].
- ▷ The **C**anada–**F**rance **R**edshift **S**urvey **CFRS** use an I–band ($17.5^{\mathrm{m}} < \mathrm{I_{AB}} < 22.5^{\mathrm{m}}$) selection and measured 730 spectroscopic redshifts within the redshift range of $0.1 < z < 0.75$ [Lilly et al., 1995].

The standard approach used in all these surveys is to derive spectroscopic redshifts for preselected sample of objects. The preselection is based on three to five color photometry. Spectroscopically derived redshift determinations are usually considered as more accurate than photometrically derived redshifts, but spectroscopy needs more observing time and does not reach equally faint objects. Another critical point is the selection effect, because not all objects in a field are selected to derive spectra.
CADIS not only uses one or two features like emission lines in the spectra to provide the redshift information comparable in quantity to most of the spectroscopic surveys. We use the whole filter (spectral) range. All this information is available for all objects in the fields.
Another advantage is, that there is no preselection influencing the results, like in the other surveys. Information about the continuum and the whole spectral energy distribution (SED) represents the third dimension of our CADIS data sample and we take this into account in our analysis.

Though the CADIS sample is unique at present, we are aware that soon the large multi–object–spectrograph for VLT[12] and Keck[13] will be available for the astronomical community and the next generation of large multi–color surveys will be carried out soon, so that in the near future a large amount of data on intermediate redshifts will be available.

---

[12] The **ESO** (**E**uropean **S**outhern **O**bservatory) **V**ery **L**arge **T**elescope (**VLT**) at the Paranal Observatory (Atacama, Chile) (http://www.eso.org/paranal/)

[13] Keck–thelecope: The twin 394 inch primary mirrors teleskopes on Hawaii's dormant Mauna Kea build by the W.M. **Keck** Foundation (http://www2.keck.hawaii.edu:3636/)

Chapter 3

Properties of galaxies

3.1 The luminosity function

When we observes a galaxy population, one of the basic quantities is the density (number of objects per volume). Due to the fact that bright objects are less common than faint objects, the density depends on the luminosity. This information is represented by the luminosity function $\Phi(M)$ (often also referred to as the differential luminosity function). As the magnitude M most often the rest frame Johnson B magnitude is used, because it best indicates the young stellar component in galaxies and the redshifted blue light is observable optical spectrum until a redshift of $z = 1.2$.

The galaxy luminosity function is one of the most basic quantities in observational cosmology. Its evolution in time is used for fitting cosmological models to observations. In addition, the shape of the galaxy luminosity function is of theoretical interest as it provides information for galaxy formation models [Koo and Kron, 1992, Efstathiou et al., 1988].

Therefore numerous investigations were made to derive the luminosity functions for different galaxy populations, starting with local measurements [Zucca et al., 1997, Marinoni et al., 1999] and galaxy clusters [Valotto et al., 1997], where it is easy to get large samples of galaxies.
Dressler [Dressler, 1980] suggested that the luminosity function depends on the mix of morphological types and on the environment (field or cluster) . This was confirmed when Sandage, Binggeli and Tammann [Sandage et al., 1985] found that the galaxy luminosity function depends on morphological type at the faint end in their Virgo cluster analysis. We will derive in this section the luminosity function of field galaxies at different redshifts and of different galaxy types (E–S0–Sa, Sb–Sc and starburst galaxies).

Many different methods have been developed to determine the luminosity function, each having its special advantages and disadvantages [Binggeli et al., 1988, Felten, 1977, Willmer, 1997, Subbarao et al., 1996, Efstathiou et al., 1988]. For our analysis we use two different techniques:

- ▷ The traditional maximum volume approach (Vmax) to derive the density in a data sample for the different luminosity bins. This makes direct use of the data and allows a nonparametric estimation.
  Then a least square fit to the data points is used to derive the best parameters for the Schechter function (see below).
- ▷ A parametric fit to the data is given by the maximum likelihood method. We use as a parametric form the Schechter function and derive the best fitting parameters.

A brief description is given in the following sections.

3.1.1 Methods for deriving the luminosity function

3.1.1.1 Maximum volume (Vmax) approach

The most direct access to the density for the luminosity function is obtained by dividing the observed number of galaxies by the **max**imal observed **V**olume (henceforth **Vmax**). This method is often labeled as the classical or traditional $\mathrm{V_{max}}$ method. It is based on the generalized Schmidt estimator [Schmidt, 1968], which is also described in the work by Felten [Felten, 1976]. We used the method as clearly outlined by Ellis et al. [Ellis et al., 1996]. This method represents a nonparametric form of the luminosity function. The major steps are the following:

Consider a sample of N galaxies ($i = 1 \cdots N$), with absolute luminosities M_i, apparent magnitudes m_i and redshifts z_i in a solid angle ω in the sky in square arcminutes. The luminosity function – the number of galaxies per unit comoving volume per bin of absolute magnitude – can be derived in a redshift limited sample $z_1 \leq z \leq z_2$ in the bin $\mathrm{M_1 \leq M \leq M_2}$ from

$$\frac{\int_{M_1}^{M_2} \int_{z_1}^{z_2} \Phi\left(M,z\right)\ dz\, dM}{\left(M_2 - M_1\right)\left(z_2 - z_1\right)} = \frac{1}{\left(M_2 - M_1\right)} \sum_{i:\, M_1 \leq M_i \leq M_2} \frac{1}{V_i} \ ,$$

where V_i is the maximal or total volume for the galaxy i, in which it is detectable. It is given by

$$\begin{aligned}
V_i &= \sum_{j=1}^{M} V_{ij} \qquad \text{where} \\
V_{ij} &= \frac{\omega}{60^2 \cdot \left(\frac{360}{2\pi}\right)^2 \cdot 4\pi} \int_{z_{min}^{ij}}^{z_{max}^{ij}} \frac{dV}{dz} dz \qquad \text{with} \\
z_{min}^{ij} &= max\ \left(z_1, z\left(M_{max}\right)\right) \\
z_{max}^{ij} &= min\ \left(z_2, z\left(M_{min\, limit_i}\right)\right),
\end{aligned}$$

where $M_{min\,limit_i}$ is the limiting absolute magnitude of the object i at which it would fall out of the sample, because it is beyond the observation limit. $z\left(M_{min\,limit_i}\right)$ is the redshift, at which an object of this magnitude could still be detected. M_{max} is the absolute magnitude of the brightest object in the sample and $z\left(M_{max}\right)$ the redshift at which an object of that magnitude is included in the sample.

The $M_{min\,limit_i}$ can directly be derived from the simulation of section 2.2.3.3. In this work we used bins of one magnitude to derive the data points for the plots. This binning is widely used in the literature. Bins less than 1^{m} would result in high uncertainties at the bright end due to low number statistics.

Under the assumption of a Poisson distribution, the error of each data point is the reciprocal of the square root of the number of objects in the corresponding bin.

Describing the luminosity function, the Schechter function has become a widely used and accepted form [Schechter, 1976, Lin et al., 1999, Ellis et al., 1996, Binggeli et al., 1988, Felten, 1977]

$$\begin{aligned} \Phi\left(x\right)dx &= \phi^{*}x^{\alpha}e^{-x}dx \\ \text{with} \quad & x = \frac{L}{L^{*}} \end{aligned}$$

The Schechter function looses its simple appearance when the luminosity L is transformed into the a logarithmic scales of magnitude via $\log_{10}(L/L^{*}) = 0.4\left(M^{*} - M\right)$:

$$\Phi\left(M\right)dM = \phi^{*}0.4\log_{10}\ 10^{0.4(M^{*}-M)(\alpha+1)}\ e^{-10^{0.4(M^{*}-M)}} \tag{3.1}$$

The parameters to fit are

- ▷ ϕ^{*}, the normalization of space density
- ▷ M^{*}, the break–off luminosity at the bright end of the function. The density decreases rapidly for brighter objects
- ▷ α, the steepness of the slope at the faint end, which represents the density of faint galaxies

The form of the Schechter function and the influence of the different parameters is shown in figure 3.1. The parameters are not independent but influence each other, because the function cannot be decomposed into linearly independent components (illustrated in section 3.1.1.3 on page 46) [Efstathiou et al., 1988]. This makes the fitting a non–trivial problem.

A Schechter function was fitted to the data points using the Levenberg–Marquard method within an IDL[1] subroutine [Press et al., 1994]. Each data point is weighted by the reciprocal of its error.

---

[1] **IDL**: **I**nteractive **D**ata **L**anguage

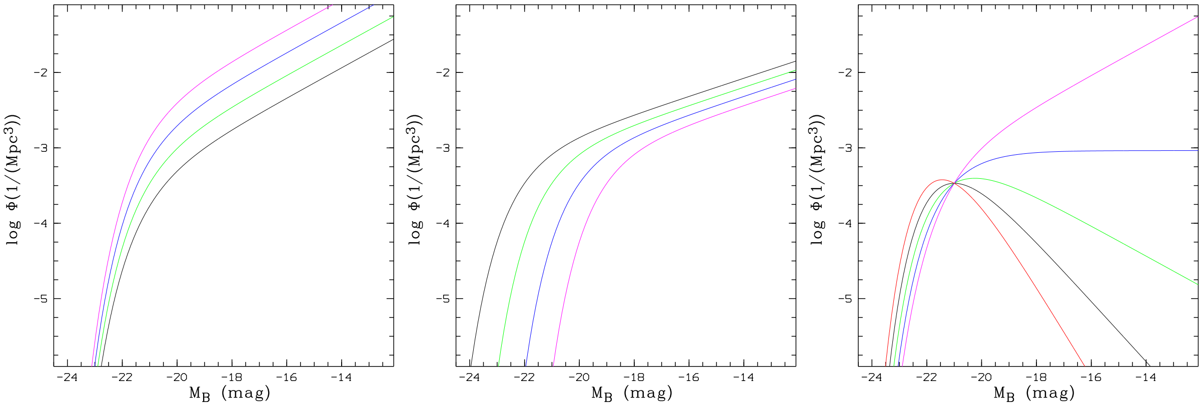

Figure 3.1: Schechter function and the influence of its parameters.
a) [left] Different ϕ^* (normalization parameter): black $\phi^* = 0.0005$ 1/Mpc^3, green $\phi^* = 0.0010$ 1/Mpc^3, blue $\phi^* = 0.0020$ 1/Mpc^3, magenta $\phi^* = 0.0040$ 1/Mpc^3 ; $M^* = -21^{\mathrm{m}}$; $\alpha = 1.5$
b) [center] Different M^* (bright end break–off): black $M^* = -22^{\mathrm{m}}$, blue $M^* = -21^{\mathrm{m}}$, green $M^* = -20^{\mathrm{m}}$, magenta $M^* = -19^{\mathrm{m}}$; $\phi^* = 0.001$ 1/Mpc^3; $\alpha = 1.3$
c) [right] Different α (faint end slope): red $\alpha = 0.5$, black $\alpha = 0.0$, green $\alpha = -0.5$, blue $\alpha = -1.0$, magenta $\alpha = -1.5$; $\phi^* = 0.001$ 1/Mpc^3; $M^* = -21^{\mathrm{m}}$

3.1.1.2 Maximum likelihood estimation (STY)

Another way to derive the luminosity function from an observed data sample uses a statistical approach via a maximum likelihood estimation.
The procedure is to test a set of fitting function parameters by computing the probability that this set of parameters is correct for each data point, and then search for the parameter set with the highest overall probability.
The maximum likelihood method is known as an unbiased estimation for the luminosity function and has a reliably determined error [Marzke et al., 1994, Efstathiou et al., 1988]. This is a parametric estimate and can only be used when the form of the fitting function is known. It provides estimates of the parameters and their associated errors but no information about the quality of the fit or how good the fitted function represents the data. To control the quality of the fit, we compare the resulting function of the maximum likelihood method with the density points derived by the Vmax method.

We use a modified version of the maximum likelihood method, which was introduced by **S**andage, **T**ammann and **Y**ahil [Sandage et al., 1979, Tammann et al., 1979] and is commonly referred to as the **STY**–method. Its usage is widely spread with different modifications [Fried et al., 2001, Marzke et al., 1994, Efstathiou et al., 1988]. A detailed description of the method is given by Lin et al. [Lin et al., 1996]. We just show a brief overview of the procedure here:

Assuming a differential luminosity function $\Phi(M)$ the probability that a galaxy has an absolute magnitude M_i is given by

$$p_i = \frac{\Phi\left(M_i\right)}{\int_{M_{min\,limit_i}}^{M_{max}} \Phi\left(M\right)\, dM} \tag{3.2}$$

We then can express the likelihood function $\mathcal{L}$ of a set of N galaxies, given by

$$\mathcal{L} = \prod_{i=1}^{N} p_i$$

with equation 3.2

$$\ln \mathcal{L} = \sum \left(\ln \Phi\left(M_i\right) - \ln \int_{M_{min\,limit_i}}^{M_{max}} \Phi\left(M\right)\, dM \right) \tag{3.3}$$

Thus, the optimal parameter set for the function $\Phi\left(M\right)$ to a given data set is given by maximizing $\mathcal{L}$. Errors can be derived by finding the contours around the maximum, because $\ln \mathcal{L}$ is a chi–square statistic, with $\Delta\chi^2$ being the contour levels of $\ln \mathcal{L}$. For a χ^2 value with the appropriate degree of freedom the corresponding error contour is given by:

$$\ln \mathcal{L} = \ln \mathcal{L}_{max} - \frac{1}{2}\Delta\chi^2$$

As input function we use the Schechter function (3.1) with its three parameters (ϕ^*, M^*, α). As can easily be seen from equation 3.2 and 3.3, the normalization factor ϕ^* of the Schechter function cancels out. Thus we have two degrees of freedom left and obtain the following confidence limits [Press et al., 1994]:

	1σ	2σ	3σ
p	68.3%	90%	95.4%
$\Delta\chi^2$	2.30	4.61	6.17

The parameter ϕ^* of the Schechter function has to be determined by normalization of the observed number of galaxies N divided by the estimated number of galaxies with a Schechter function with the optimal parameters M^*_{max} and α_{max}. ϕ^*_{max} is then simply the number counts over integral of the Schechter function:

$$\phi^*_{max} = \frac{N}{\omega \int_{z_1}^{z_2} \int_{-\infty}^{\overline{M}_{max\,limit}(z)} \Phi\left(M^*_{mag}, \alpha_{max}\right) \frac{dV}{d\Omega dz}\, dM\, dz}$$

with $\overline{M}_{max\,limit}$ being the average limiting absolute magnitude of all galaxies at a certain redshift z.

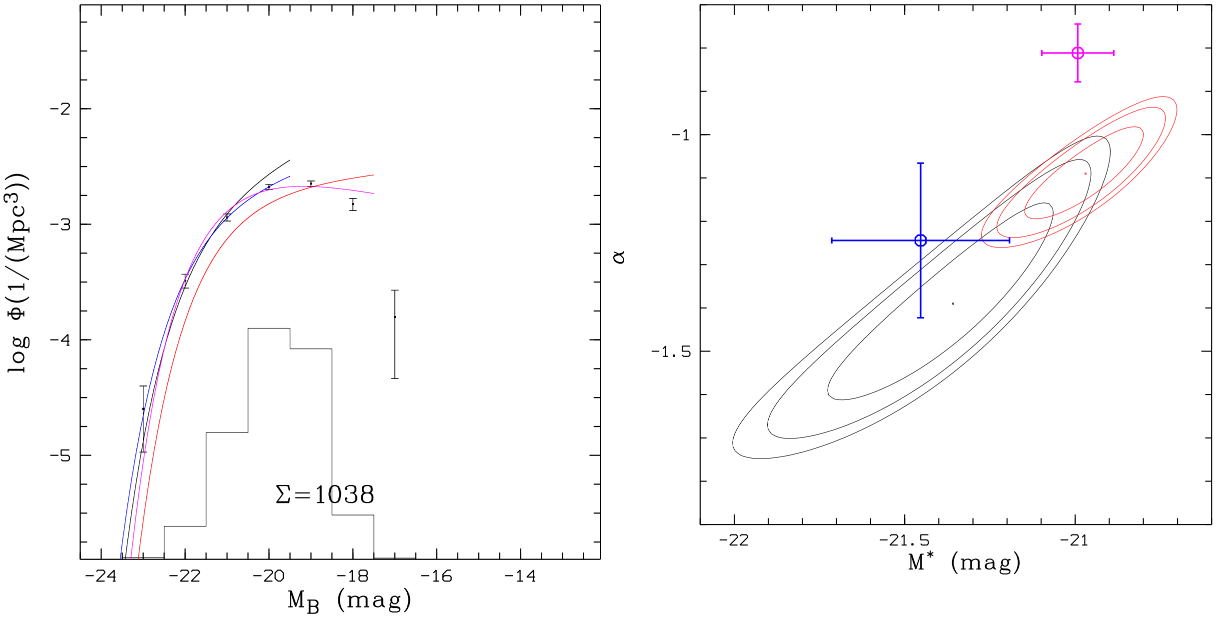

Figure 3.2: Comparison of two fitting methods for the luminosity function illustrated for starburst galaxies at a redshift of 0.5 to 0.75
STY luminosity fit in **black down to a limit of** $M_{\mathrm{B}} = -19.5^{\mathrm{m}}$ and red down to $M_{\mathrm{B}} = -17.5^{\mathrm{m}}$
Vmax luminosity fit in blue down to a limit of $M_{\mathrm{B}} = -19.5^{\mathrm{m}}$ and magenta down to $M_{\mathrm{B}} = -17.5^{\mathrm{m}}$
a) [left] Luminosity function, and underlaid is a linearly scaled histogram of the data distribution.
b) [right] Error ellipses with 1σ central contour, 2σ medium contour and 3σ outer contour around the maximum for the STY–method
plotted on top are the results from the Vmax with the standard deviation error (1σ)

3.1.1.3 Comparison of the two methods

As an example we show in figure 3.2 the derived Schechter functions for a subset of galaxies, which are classified as starburst (SED > 60) in a redshift range from 0.5 to 0.75. As we will use this form of plot frequently thoughtout this work, some explanation will be given in the next paragraph.

The black data points in figure 3.2a correspond to the density derived from the Vmax calculations. The density (abscissa) is calculated per magnitude bin (M-$0.5^{\mathrm{m}} < M < M$+0.5^{m}) in a volume of one Mpc^3, shown on a logarithmic scale. Additionally a histogram of the number counts is over plotted, illustrating the distribution of the number of galaxies in the magnitude bins. The total number of galaxies (i.e. the integral over the histogram) is also given. The scale of the histogram is linear to display the proportion of the counts. Its maximum gives an idea of the completeness limit of the sample. Overlaid in color are the fitted Schechter functions with the following parameters:

			ϕ^* $\left(\frac{1}{\mathrm{Mpc}^3}\right)$	1σ error	M^* (mag)	1σ error	α	1σ error
black:	STY–fit	$< -19.5^{\mathrm{m}}$	0.00240	-	-21.36	±0.26	-1.09	±0.20
blue:	Vmax–fit	$< -19.5^{\mathrm{m}}$	0.00215	±0.00072	-21.45	±0.26	-1.24	±0.18
red:	STY–fit	$< -17.5^{\mathrm{m}}$	0.00227	-	-20.97	±0.17	-1.39	±0.12
magenta:	Vmax–fit	$< -17.5^{\mathrm{m}}$	0.00382	±0.00041	-20.99	±0.10	-0.811	±0.067

The plotted function ends at the faintest object taken into account for the fit. As mentioned above, in the STY-fitting ϕ^* cancels out and so no error estimation for ϕ^* is provided by this method. The errors in the remaining two dimensions M^* and α are shown in figure 3.2b as 1σ, 2σ and 3σ contours. In the case of independent parameters, concentric circles around the maximum can be expected. We see that the parameters M^* and α are not independent. With increasing α, M^* is rising as well. The plot shows also that the error ellipses get smaller with increasing number of included data points. The final independent errors for the fitting parameters M^* and α are derived by projecting the χ^2 in figure 3.2b into one dimension and deriving the 1σ level from a fitted gaussian distribution. We cross–checked the error calculation with the bootstrapping method [Barrow et al., 1984]. The bootstrapping error agreed within 10% with the errors derived from the STY and Vmax methods.

In figure 3.2b we added the data points and errors of the Vmax-fits and can see a nearly perfect overlap of the measurements in the M^* dimension. A slight offset in the α dimension is found. This offset in α reflects one of the differences of the two fitting methods.

The derived parameters for the Schechter functions are in good agreement and give functions fitting to the Vmax data points. The main advantage of the STY method is the possibility to fit small data sets. The Vmax-fits tend to follow the underlying data points as is expected from this method. The STY-method does not use the binning of the data and so often shows a slightly different turn–off at the bright end. The STY–fit is more influenced by a high agglomeration of data points. For example, at the faint end of the function where the error bars becomes larger it is less *bent down* then the Vmax-fit because of the lower number of data points. This is the region where we additionally lose completeness.
We perform a completeness correction in the STY fit, which will be introduced in the next section. That additionally steepens the fits at the faint end of the function.

3.1.1.4 Completeness correction

As we know about focusing effects in M, z and SED due to the classification (compare section 2.2), and the incompleteness of the detection and the classification limit. Therfore, we perform a completeness correction for our analysis. The correction takes mainly care of the incompleteness at the faint end of the data sample. The faint end of our observations is defined by the classification procedure. This gives us the possibility to study the completeness at the faint end simulations. We generate a galaxy sample with decreasing

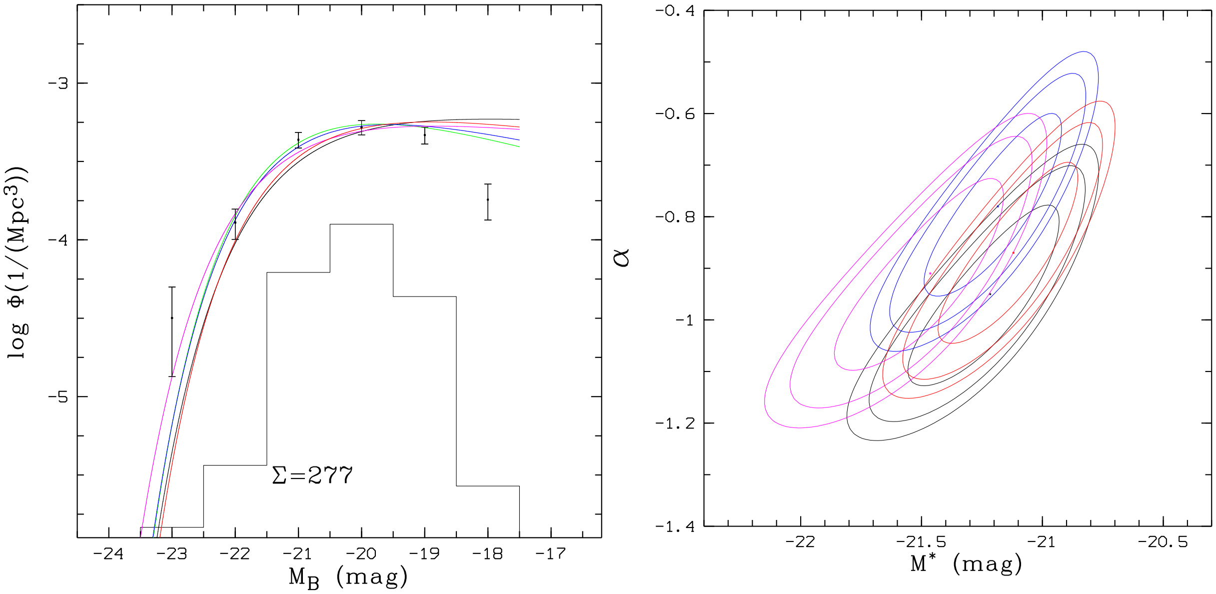

Figure 3.3: Comparison of different completeness corrections on the example of the Sb\Sc galaxies at a redshift of 0.5 to 0.75
Vmax luminosity function fit in green with
$\phi^* = 0.00118\, 1/_{\mathrm{Mpc}^3},\ M^* = -21.20^{\mathrm{m}},\ \alpha = -0.589$
STY fit without completeness correction in blue with
$\phi^* = 0.00118\, 1/_{\mathrm{Mpc}^3},\ M^* = -21.20^{\mathrm{m}},\ \alpha = -0.589$
STY fit with completeness with distribution correction one in red with
$\phi^* = 0.00118\, 1/_{\mathrm{Mpc}^3},\ M^* = -21.20^{\mathrm{m}},\ \alpha = -0.589$
STY fit with Schechter completeness correction in magenta with
$\phi^* = 0.00118\, 1/_{\mathrm{Mpc}^3},\ M^* = -21.20^{\mathrm{m}},\ \alpha = -0.589$
STY fit with random completeness correction in black with
$\phi^* = 0.00118\, 1/_{\mathrm{Mpc}^3},\ M^* = -21.20^{\mathrm{m}},\ \alpha = -0.589$
a) [left] Luminosity function
b) [right] Error ellipses with 1σ, 2σ and 3σ limits

magnitudes, scattered in magnitude with the error in the magnitude and classify this artificially generated sample. The completeness can then be calculated by comparing the number of classified galaxies to the number of input galaxies. The classification dependents on the SED, redshift (z) and magnitude (observed in I = B815) of the object. The completeness $C(SED, z, m)$ then is calculated via

$$C\left(SED, z, m\right) = \frac{N_{class}(SED, z, m)}{N_{input}(SED, z, m)}$$

Such a completeness calculation was already shown in figure 2.16 exemplarily for two different SEDs.
With this definition, C > 1 means more objects are classified in that bin than there really should be. This is connected with the crowded or focused region in the M–z diagram

(figure 2.21).
C < 1 shows that the classification is not complete in that bin, because less objects are classified than generated in that bin. In this case the object within a given bin should be weighed higher in the analysis. We can now correct equation 3.2 to obtain a completeness corrected maximum likelihood probability with

$$p_i = \frac{\Phi\left(M_i\right)}{\int_{M_{min\,limit_i}}^{M_{max}} \Phi\left(M\right)\,dM}\,\frac{1}{C(SED,z,m)} \tag{3.4}$$

It is not necessary to include the completeness in the normalization integral, because we use the exact detection limit of each individual object, which we derived in section 2.2.3.3. The completeness correction was derived in bins of ΔSED $= 3$ ($0\cdots 99$; in 34 bins) $\Delta z = 0.05$ ($0.0\cdots 2.0$; in 40 bins) and $\Delta m = 0.5$ ($16^{\mathrm{m}}\cdots 27.6^{\mathrm{m}}$; in 58 bins). We checked three different approaches to generate the completeness correction function:

- ▷ Use a set of 10 galaxies with the equivalent SED, redshift and luminosity (I / B815) in each bin of the completeness function, scatter them by the magnitude error according to the brightness of the object and classify this set of 305 659 galaxies.
- ▷ Use a representative set of 250 000 galaxies distributed according to the CADIS data set:
  - 25% early type (SED < 50) distributed in luminosity by a Schechter function ($M^* = -21.0^{\mathrm{m}}$, $\alpha = -0.7$) down to 25^{m} in I (B815)
  - 75% late type (SED > 50) distributed in luminosity by a Schechter function ($M^* = -21.0^{\mathrm{m}}$, $\alpha = -1.4$) down to 25^{m} in I (B815)
- ▷ Use 40 galaxies at each redshift and SED (overall 804 000) and assign them a randomly generated (Monte Carlo) apparent I (B815) magnitude between 15^{m} and 25^{m}

The different behavior of the three completeness functions is tested for the luminosity function of Sb–Sc galaxies ($37 <$ SED < 60). The different results are illustrated in figure 3.3. The blue curve with no completeness correction has naturally the lowest slope at the faint end of the distribution. With each of the three completeness corrections the faint end of the luminosity function slope is increased.
The completeness correction based on the Schechter function distribution tends to correct to more luminous M^*. The reason for this can be found in the low statistics in the completeness correction function at the bright end. In the error plot (figure 3.3b), it can be seen that the error ellipse of the random distribution and the dot distribution are on top of each other, and so the influence on the results of these two completeness corrections is nearly the same.

In this work we decided to use the *random* completeness correction because all SEDs and redshifts are equally represented and have the largest statistics.

The completeness correction in the following parts is only incorporated into the STY fits. The data points and the Vmax fit are left without a completeness correction to give an idea about the influences of the incompleteness.

3.1.1.5 Influence of the observational limit

In section 2.2.3.3 we mentioned the effect of an imprecise magnitude limit on the luminosity function. Now we analyze this problem more carefully. In figure 3.4 the luminosity function for starburst galaxies in the redshift range of 0.3 to 0.5 is plotted with different limiting magnitudes. The black data points were calculated with the limiting magnitude derived from simulations for each individual observed object (as described in section 2.2.3.3). Those limiting apparent magnitudes range from 22^{m} to 24^{m} and are depended on redshift, SED, the 17 measured filter–fluxes and the errors in each flux measurement.
By setting the limiting magnitude to a low general limit of 22.5^{m} we obtain the results shown in green. The survey volume is underestimated and we notice a density that is too high at the faint end of the luminosity function. On the other hand the red plotted symbols show a too high survey volume, because the I–band (B815) limit was set to 25^{m}. This causes the density to be underestimated.

The fitted luminosity function using the Vmax method follows the data points, but the faint end parameter α differs from reality because of incompleteness. In the case of the STY–fit we can see that an overestimation of the limiting magnitude does not influence the fit. This is shown by the closed error ellipses in figure 3.4c. This effect is due to the completeness correction, which cuts off the incompletely surveyed volume at the faint end. In contrast the STY–fit method is influenced heavily by an overestimation of the limiting magnitude at the faint end of the data set, as was used in previous publications [Fried et al., 2001, Lin et al., 1999, Lilly et al., 1995].

Thus in this analysis we have taken care of the lower limit of the faint end of the luminosity function with completeness correction and the individual limiting magnitude. Nevertheless a steeper end of the luminosity function is still possible.
This is due to the fact that our completeness function is a good approximation but still differers slightly from reality because the artificially generated spectra does not behave exactly like real galaxies in the multi-color classification. With fainter magnitudes the difference between artificially generated galaxies color indices and real galaxies spectra increases and the incompleteness function loose accuracy.
Anyway we must be careful with every statement about slope at the faint end of the luminosity function and will concentrate on conclusions obtained from the bright end (M^*).

3.1.1.6 Field to field variation

To test the homogeneity of the data sample, we subdivided all galaxies in the redshift range from 0.1 to 0.3 into the 4 different CADIS fields and compared the luminosity functions.

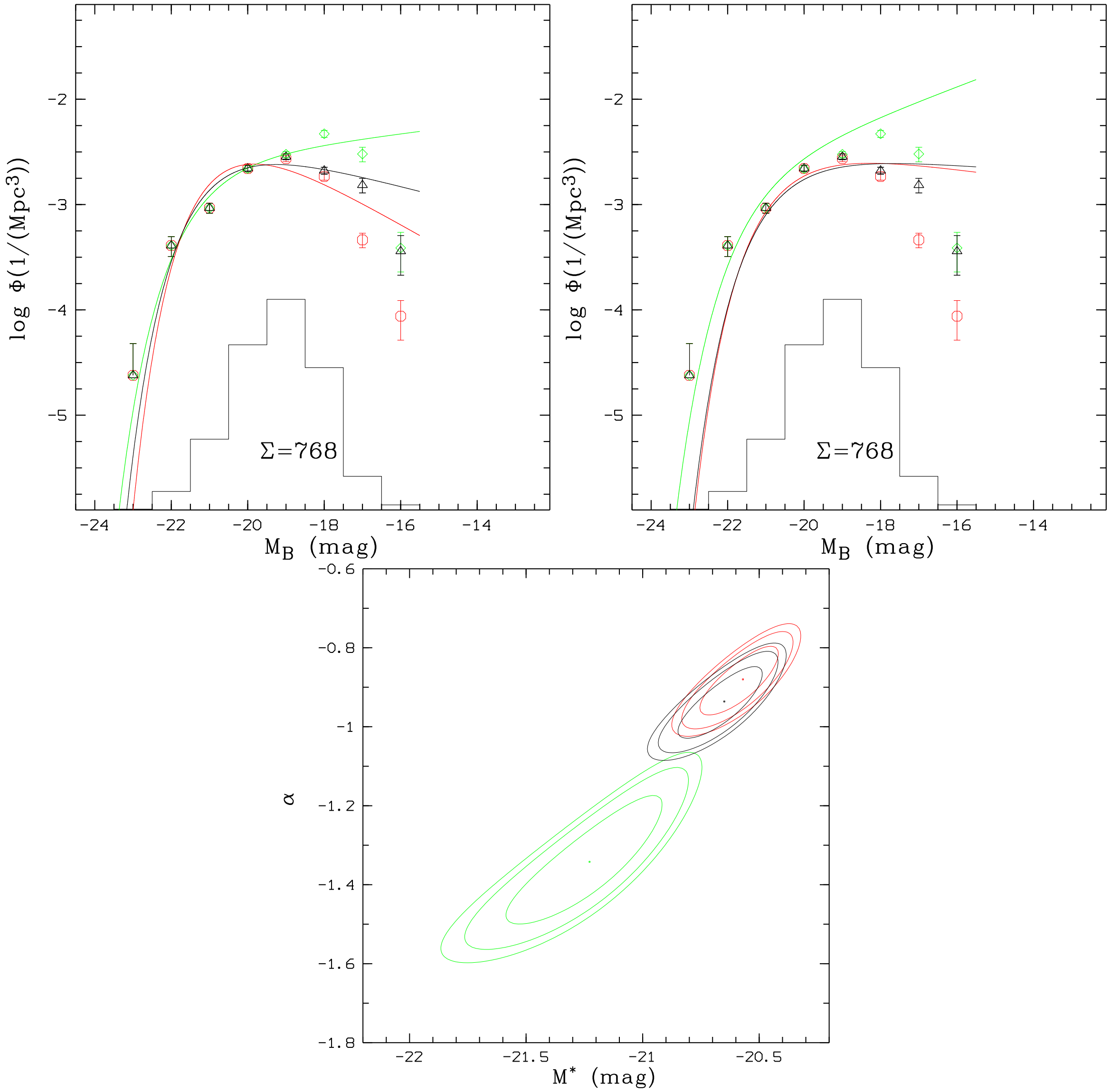

Figure 3.4: Comparison of the luminosity function fits with different limiting magnitudes. As an example starburst galaxies at a redshift of 0.3 to 0.5 are used. Underlaid is a linear scaled histogram of the distribution of the data.

black with individual computed limits Vmax

$\phi^* = 0.0046\, 1/_{\mathrm{Mpc}^3},\ M^* = -20.82^{\mathrm{m}},\ \alpha = -0.76$

STY: $\phi^* = 0.0034\, 1/_{\mathrm{Mpc}^3},\ M^* = -20.65^{\mathrm{m}},\ \alpha = -0.93$

green with an underestimated limit in I (B815) of 22.5^{m} Vmax:

$\phi^* = 0.0029\, 1/_{\mathrm{Mpc}^3},\ M^* = -21.18^{\mathrm{m}},\ \alpha = -1.11$

STY: $\phi^* = 0.0028\, 1/_{\mathrm{Mpc}^3},\ M^* = -21.23^{\mathrm{m}},\ \alpha = -1.34$

red with an overestimated limit of 25^{m} in I (B815) Vmax:

$\phi^* = 0.0062\, 1/_{\mathrm{Mpc}^3},\ M^* = -20.54^{\mathrm{m}},\ \alpha = -0.48$ STY:

$\phi^* = 0.0039\, 1/_{\mathrm{Mpc}^3},\ M^* = -20.57^{\mathrm{m}},\ \alpha = -0.88$

a) [top] Luminosity functions with Vmax fit

b) [bottom left] Luminosity functions with STY fit

c) [bottom right] Error ellipses with 1σ, 2σ and 3σ limits

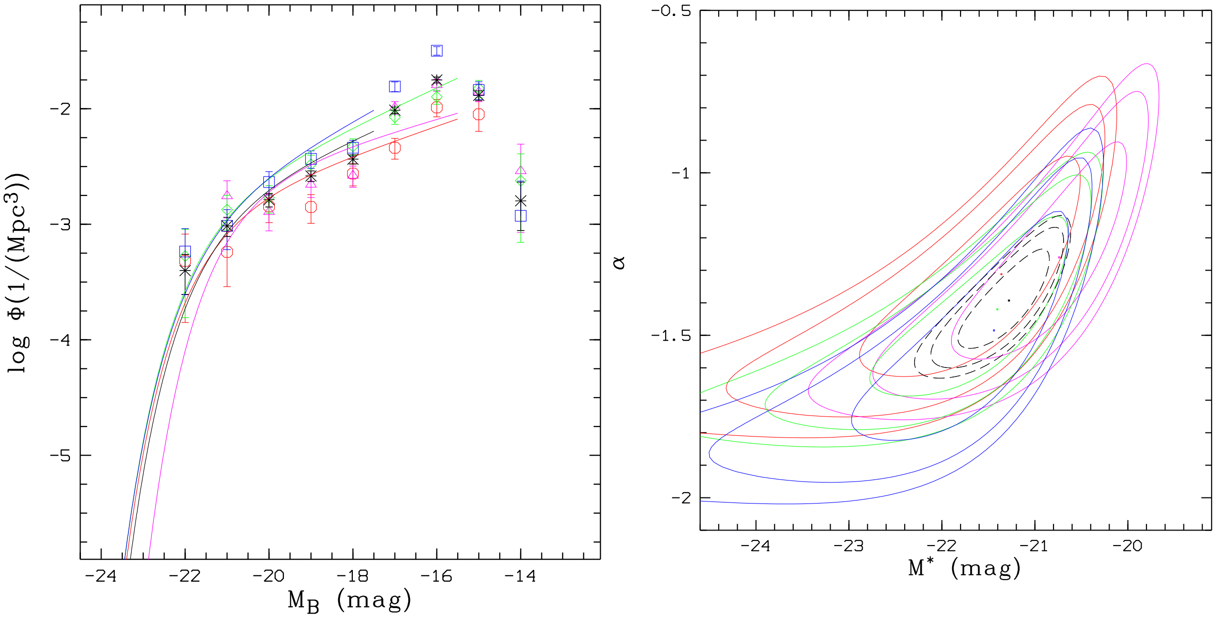

Figure 3.5: Comparison of the luminosity function of the different CADIS field exemplary for of all galaxies at a redshift of 0.1 to 0.3.
red 01h CADIS field with $\phi^* = 0.0017\,1/_{\mathrm{Mpc}^3}$, $M^* = -21.36^{\mathrm{m}}$, $\alpha = -0.78$
magenta 09h CADIS field with $\phi^* = 0.0029\,1/_{\mathrm{Mpc}^3}$, $M^* = -20.74^{\mathrm{m}}$, $\alpha = -1.26$
green 16h CADIS field with $\phi^* = 0.0020\,1/_{\mathrm{Mpc}^3}$, $M^* = -21.40^{\mathrm{m}}$, $\alpha = -1.42$
blue 23h CADIS field with $\phi^* = 0.0019\,1/_{\mathrm{Mpc}^3}$, $M^* = -21.44^{\mathrm{m}}$, $\alpha = -1.49$
black all fields combined with $\phi^* = 0.00181/_{\mathrm{Mpc}^3}$, $M^* = -21.28^{\mathrm{m}}$, $\alpha = -1.39$
a) [left] Luminosity function
b) [right] Error ellipses with 1σ, 2σ and 3σ limits

In figure 3.5 we show the luminosity function and error ellipse coded in different colors. The error ellipses are in good agreement, with the maximum of each STY–fit falling into the 2σ limit of the overall fit (black). It is clear from figure 3.5b, that the error ellipse of all fields together is the smallest because of the highest statistics.
For the fit of the 23h field we use a limit of -17.5^{m} because the density of galaxies fainter than-17.5^{m} is higher than n the other fields. It seems that the observed pencil beam of the 23h field hits a filament in the structure of the universe within redshifts of 0.1 to 0.3. In order not to influence the results by this local density maximum, the fit for all fields had to be limited to -17.5^{m} as well.

3.1.2 Luminosity functions of the CADIS data set

We subdivide the CADIS data set into four redshift bins to analyze the evolution of the galaxy population:

- ▷ Local redshift bin with $0.1 < z < 0.3$: we expect here problems with statistics because of the pencil beam effect as well as problems of missing the bright end of the population because of the selection of the CADIS fields
- ▷ A low redshift bin with $0.3 < z < 0.5$
- ▷ A medium redshift bin with $0.5 < z < 0.75$
- ▷ A high redshift with $0.75 < z < 1.1$

Analysis below redshifts of 0.1 is not performed because the number of objects is too low (pencil beam effect).

For higher redshifts several problems in the data set occur. At $z > 1.1$, the 4000Å break is shifted towards the infrared where CADIS observed only two filters and so the accuracy of the classification has to be considered as being critical. Additionally more than 50% of the objects at redshifts of $z > 1.1$ are beyond 23^{m} in B815 (I). The third point is that the accuracy of the classification process is not yet tested with spectroscopically redshifts.

The luminosity functions of the galaxy population in the redshift bins are plotted in figure 3.6. The fitting parameters are summarized in table 3.1. On pages 55, 56 and 57 in figures 3.7, 3.8 and 3.9 luminosity functions of starburst (SED > 60), Sb–Sc ($37.3 <$ SED < 60) and E–S0–Sa (SED < 37.5) galaxy subsamples are shown.

Not all subsamples show a density distribution, which can be described by a Schechter function. Especially in the low redshift ranges $0.1 < z < 0.5$, the E–S0–Sa as well as Sb–Sc galaxies show a distribution in luminosity which is not explained yet and probably due to low statistics.

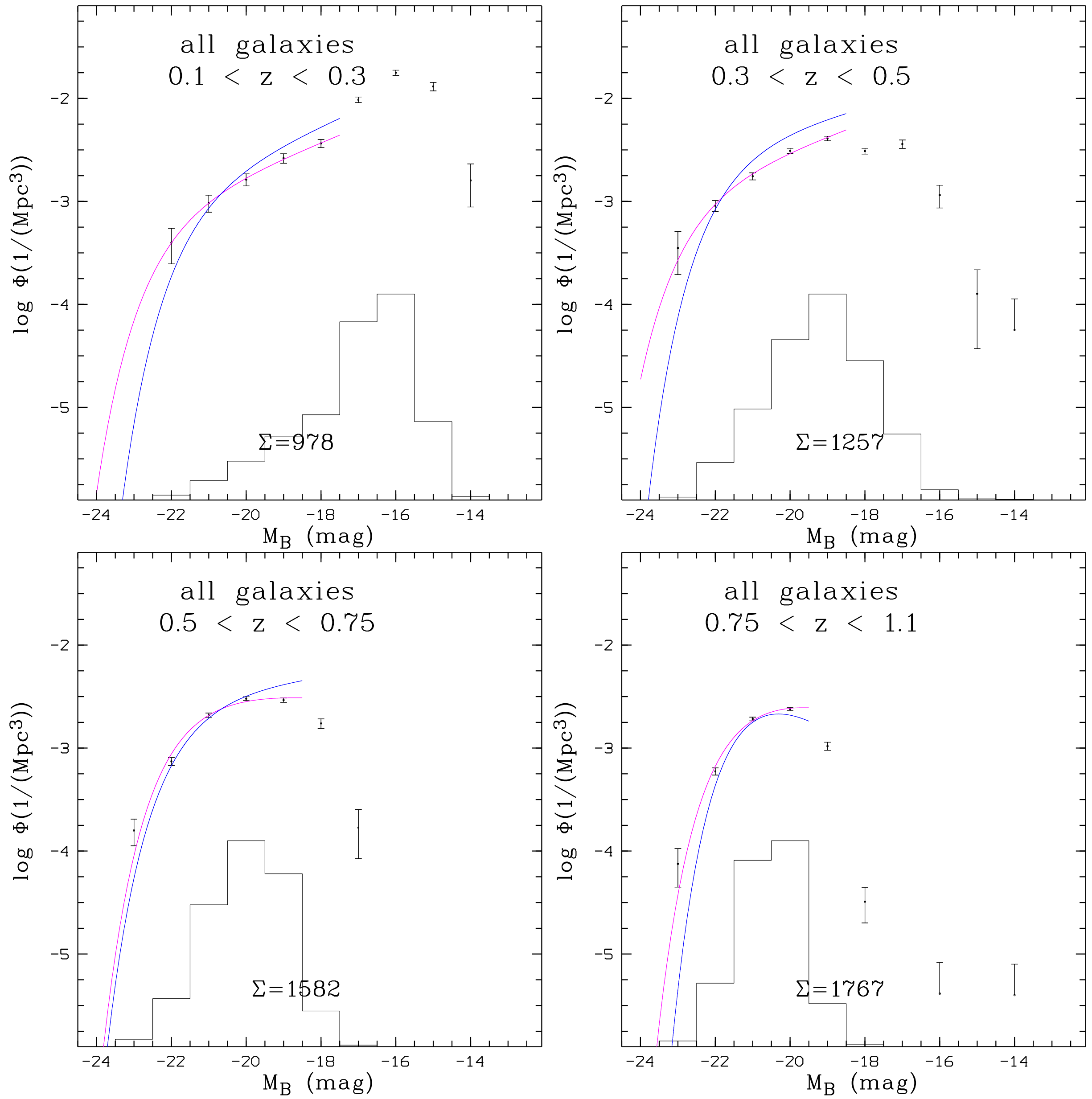

Figure 3.6: Luminosity function of all spectral types in magenta Vmax–fit and in blue STY–fit. Fitted parameters are given in table 3.1. A linear scaled histogram of the distribution of the data is underlaid. Error ellipses are presented in figure 3.12

a) [top left] Local redshift $(0.1 < z < 0.3)$
b) [top right] Low redshift $(0.3 < z < 0.5)$
c) [center left] Medium redshift $(0.5 < z < 0.75)$
d) [center left] High redshift $(0.75 < z < 1.1)$

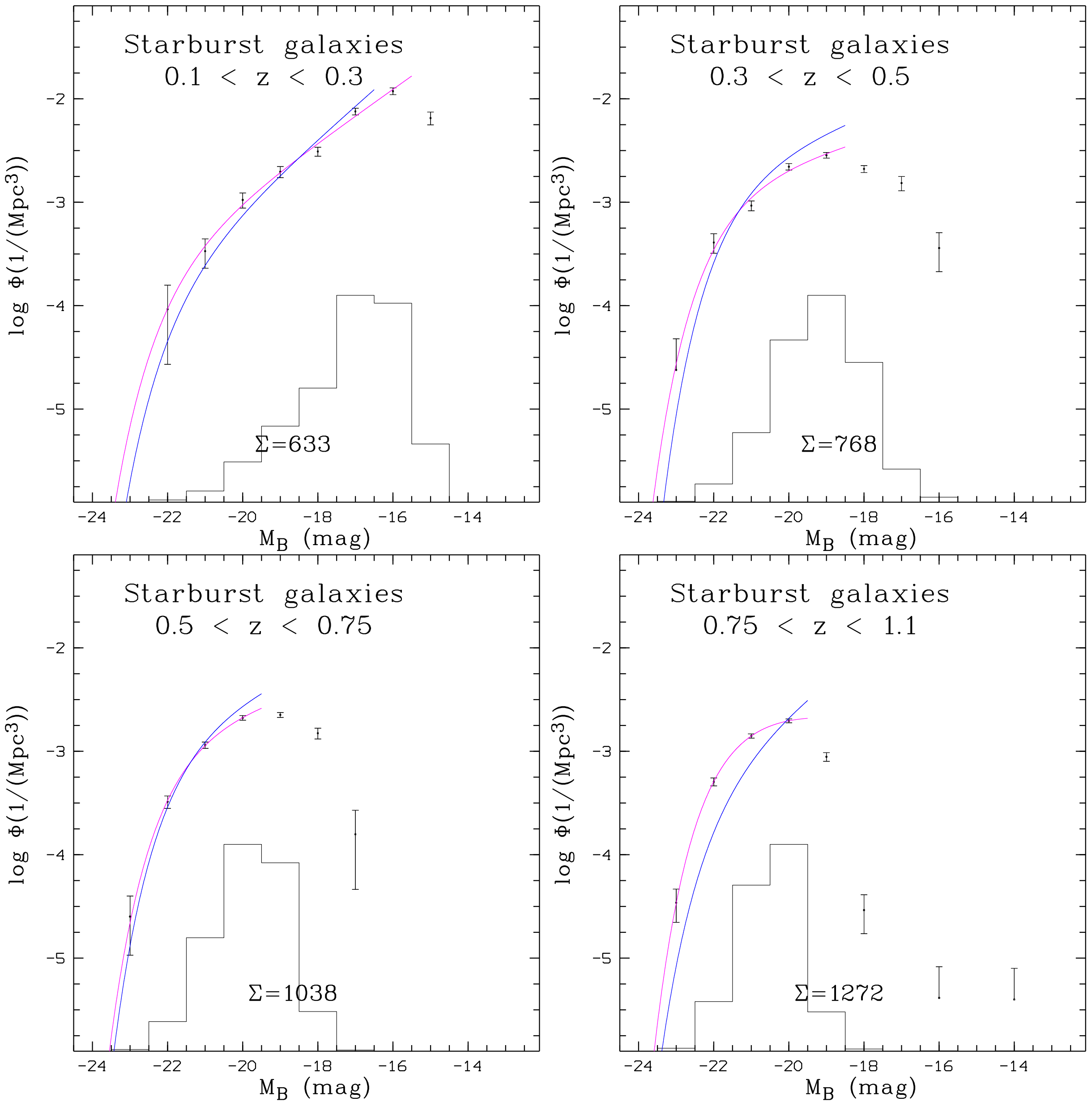

Figure 3.7: Luminosity function of starburst galaxies in magenta Vmax–fit and in blue STY–fit. Fitted parameters are combined in table 3.1. A linear scaled histogram of the distribution of the data is underlaid. Error ellipses are presented in figure 3.12

a) [top left] Local redshift ($0.1 < z < 0.3$)

b) [top right] Low redshift ($0.3 < z < 0.5$)

c) [center left] Medium redshift ($0.5 < z < 0.75$)

d) [center left] High redshift ($0.75 < z < 1.1$)

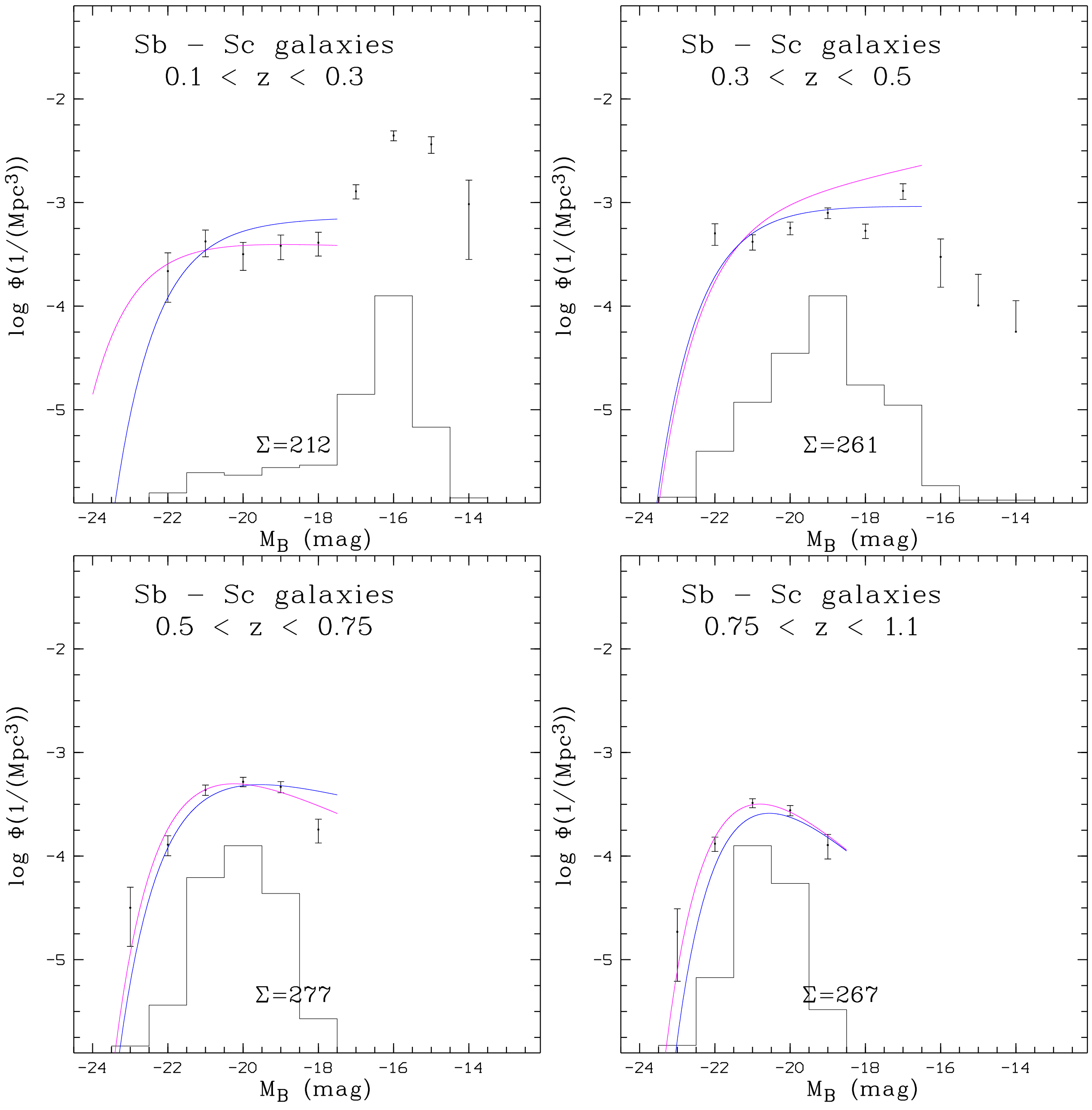

Figure 3.8: Luminosity function of Sb–Sc galaxies in magenta Vmax–fit, and in blue STY–fit. Fitted parameters are combined in table 3.1. A linear scaled histogram of the distribution of the data is underlaid. Error ellipses are presented in figure 3.13
a) [top left] Local redshift ($0.1 < z < 0.3$)
b) [top right] Low redshift ($0.3 < z < 0.5$)
c) [center left] Medium redshift ($0.5 < z < 0.75$)
d) [center left] High redshift ($0.75 < z < 1.1$)

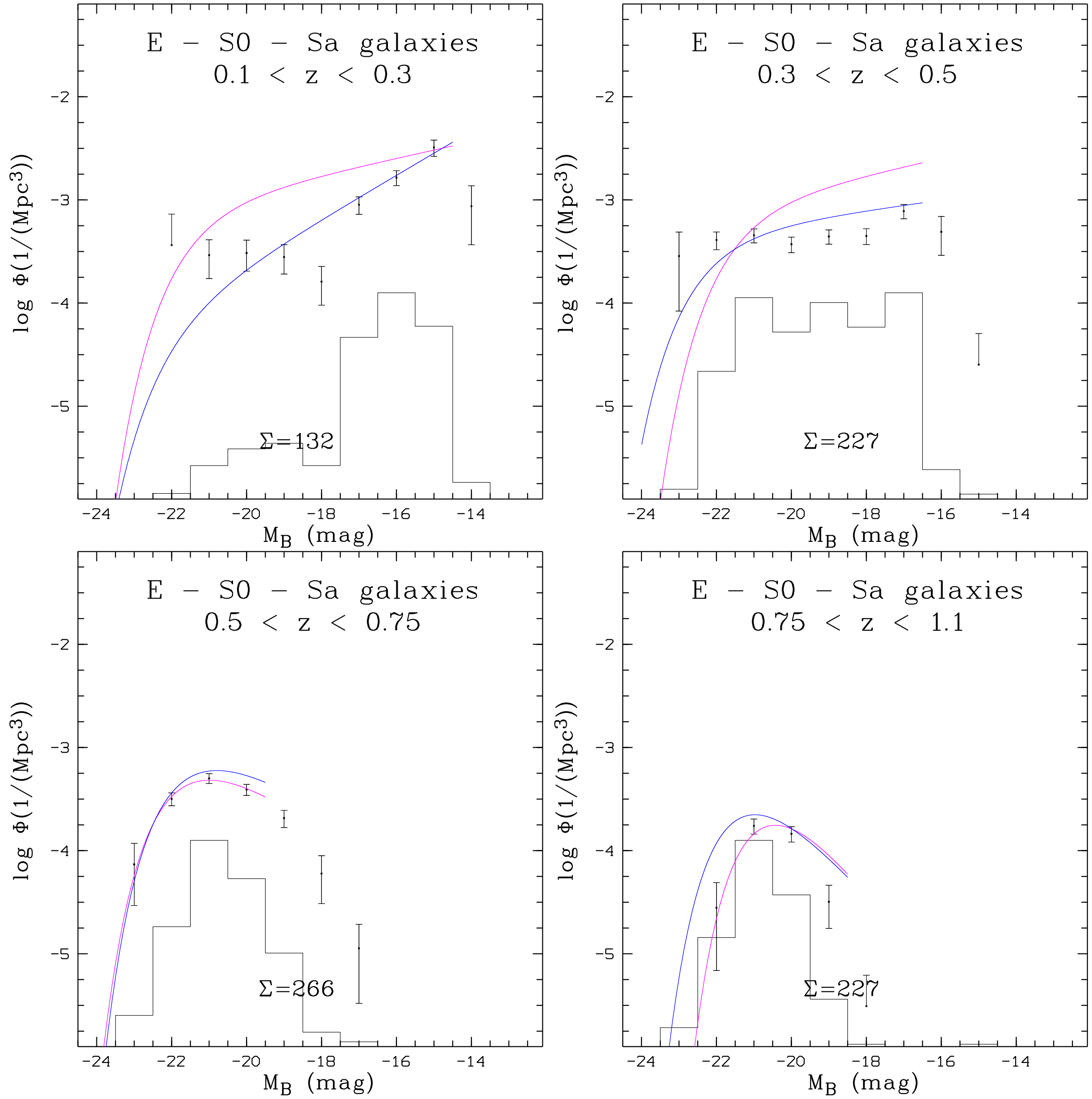

Figure 3.9: Luminosity function of E–S0–Sa galaxies in magenta Vmax-fit and in blue STY–fit. Fitted parameters are combined in table 3.1. A linear scaled histogram of the distribution of the data is underlaid. Error ellipses are presented in figure 3.13
a) [top left] Local redshift ($0.1 < z < 0.3$)
b) [top right] Low redshift ($0.3 < z < 0.5$)
c) [center left] Medium redshift ($0.5 < z < 0.75$)
d) [center left] High redshift ($0.75 < z < 1.1$)

			local redshift $0.1 < z < 0.3$	low redshift $0.3 < z < 0.5$	medium redshift $0.5 < z < 0.75$	high redshift $0.75 < z < 1.1$
all	Vmax	ϕ^*	0.00106 ± 0.00069	0.00163 ± 0.00037	0.00143 ± 0.00050	0.00474 ± 0.00059
		M*	-22.08 ± 0.80	-22.51 ± 0.27	-21.53 ± 0.12	-21.22 ± 0.13
		α	-1.36 ± 0.12	-1.33 ± 0.05	-0.929 ± 0.061	-0.768 ± 0.12
	STY	ϕ^*	0.00182	0.00426	0.00379	0.00608
		M*	-21.28 ± 0.58	-21.59 ± 0.34	-21.49 ± 0.22	-20.65 ± 0.15
		α	-1.39 ± 0.20	-1.23 ± 015	-1.12 ± 0.12	-0.27 ± 0.18
starburst	Vmax	ϕ^*	0.000468 ± 0.00028	0.00193 ± 0.00065	0.00215 ± 0.00072	0.00332 ± 0.000010
		M*	-21.68 ± 0.67	-21.54 ± 0.31	-21.45 ± 0.26	-21.23 ± 0.042
		α	-1.64 ± 0.05	-1.26 ± 0.12	-1.24 ± 0.18	-0.882 ± 0.034
	STY	ϕ^*	0.000346	0.00276	0.00240	0.00115
		M*	-21.50 ± 0.78	-21.23 ± 0.40	-21.36 ± 0.42	-21.51 ± 0.36
		α	-1.80 ± 0.14	-1.34 ± 0.16	-1.39 ± 0.35	-1.66 ± 0.30
Sb–Sc	Vmax	ϕ^*	0.000496 ± 0.00016	0.00100 ± 0.000068	0.000118 ± 0.00018	0.000922 ± 0.000064
		M*	-22.63 ± 1.18	-22.50 ± 0.11	-21.20 ± 0.18	-21.02 ± 0.086
		α	-0.966 ± 0.094	-1.20 ± 0.03	-0.966 ± 0.12	-0.178 ± 0.086
	STY	ϕ^*	0.000741	0.00104	0.000924	0.000749
		M*	-21.41 ± 0.85	-21.48 ± 0.56	-21.18 ± 0.45	-20.79 ± 0.32
		α	-1.01 ± 0.44	-0.922 ± 0.25	-0.780 ± 0.34	-0.196 ± 0.47
E–S0–Sa	Vmax	ϕ^*	0.00100 ± 0.000098	0.00100 ± 0.000073	0.000130 ± 0.000010	0.000514 ± 0.00018
		M*	-21.50 ± 0.32	-21.5 ± 0.09	-21.54 ± 0.01	-20.27 ± 0.17
		α	-1.20 ± 0.02	-1.20 ± 0.03	-0.387 ± 0.008	-0.156 ± 0.20
	STY	ϕ^*	0.0000983	0.000519	0.00155	0.000657
		M*	-22.02 ± 1.10	-22.36 ± 0.58	-21.47 ± 0.39	-20.96 ± 0.38
		α	-1.53 ± 0.27	-1.13 ± 0.15	-0.464 ± 0.47	-0.0119 ± 0.41

Table 3.1: Parameters of the luminosity function for the CADIS data set; ϕ in $\frac{1}{\mathrm{Mpc}^3}$ and M^* in mag.

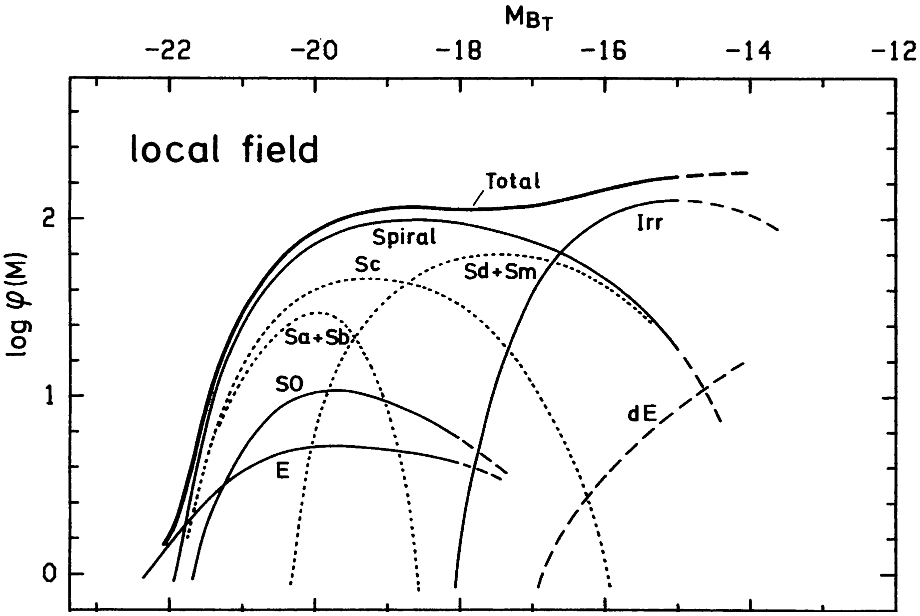

Figure 3.10: The general luminosity function of the local field and its composition of luminosity functions of different morphological types from Binggeli (H_0 = 100 km/(sec Mpc)) [Binggeli et al., 1988]

3.1.3 Luminosity function for different galaxy types

Binggeli showed in his review about luminosity functions of galaxies the luminosity function of the local field and its composition of different morphological types (figure 3.10) [Binggeli et al., 1988, Zucca et al., 1997]. The figure 3.10 shows that the faint end of the luminosity function is dominated by irregular galaxies. The bright end is dominated by spiral galaxies and E–S0, which contribute a small fraction of the population. We map this composition of the luminosity function with the CADIS data set at different redshifts in figure 3.11.

Figures 3.11a-d show that in the brightest bin of the data sample at all redshifts the earlier type galaxy population is dominant. As this is valid only in the brightest bin, thus it is a very small effect.
Figure 3.11 shows that the luminosity functions for E–S0–Sa and Sb–Sc galaxies have similar shapes in all redshift bins. Although the spiral population in the local field [Marinoni et al., 1999] falls off at a certain magnitude, we do not find this effect in the CADIS data set. Of course, the observational limit causes the luminosity function to fall off at the faint end in the distant redshift bins, but this is due to a remaining error in the completeness (section 3.1.1.4). In the low redshift bins, there is no such decline.
In contrast to the irregular galaxies in the local field, the starbursting galaxies are present at all luminosities and not only at the faint end of the population.
This can be explained by the different selection criteria: a morphologic selection for the

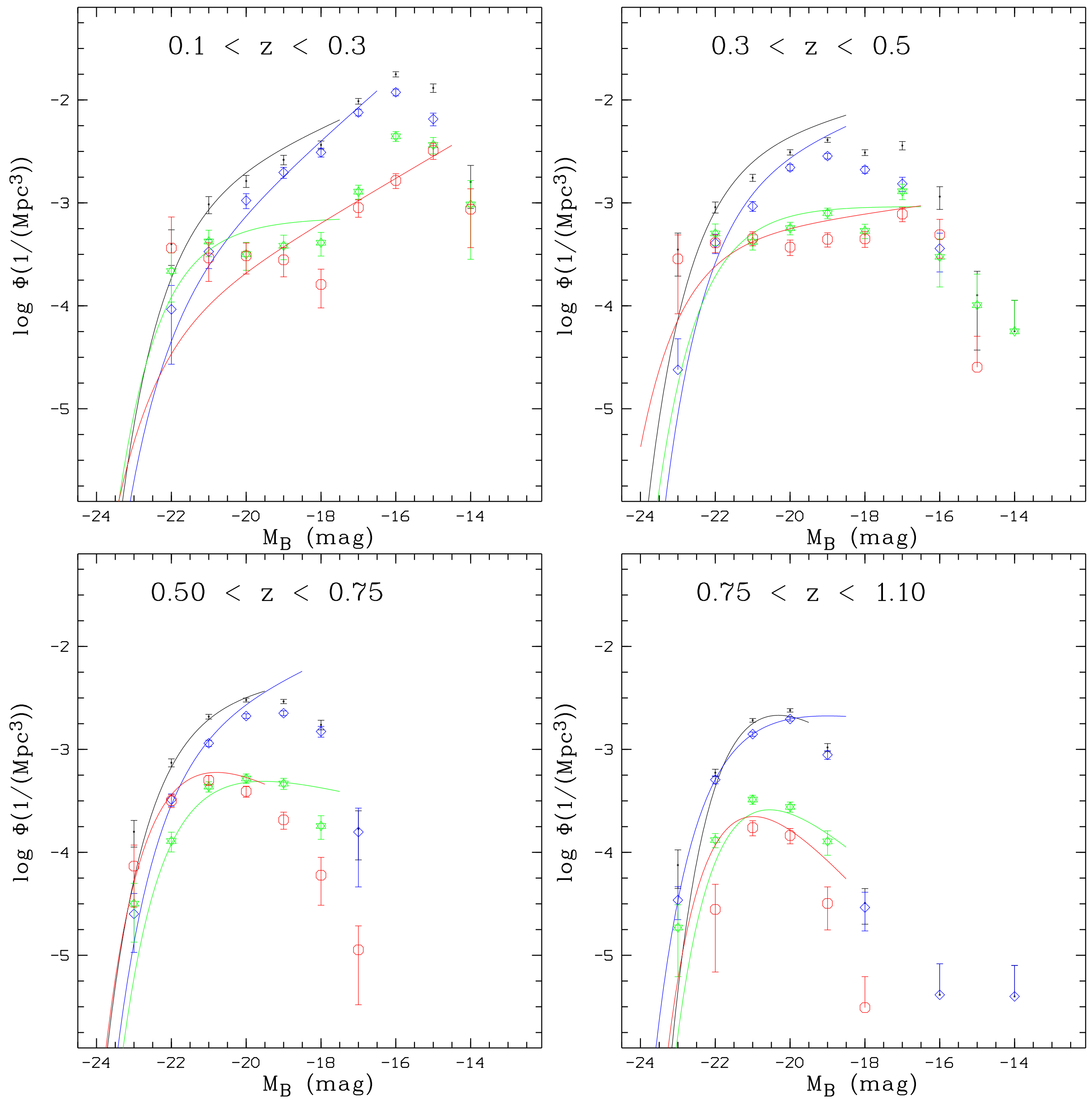

Figure 3.11: Luminosity function for different galaxy types at different redshifts: **black all galaxies**, red E–S0–Sa galaxies, green Sb–Sc galaxies and in blue starburst galaxies. Fitted STY parameters are combined in table 3.1.
a) [top left] Local redshift ($0.1 < z < 0.3$)
b) [top right] Low redshift ($0.3 < z < 0.5$)
c) [center left] Medium redshift ($0.5 < z < 0.75$)
d) [center left] High redshift ($0.75 < z < 1.1$)
error ellipses are shown in figure 3.6 3.7 3.8 and 3.9

local field luminosity function [Binggeli et al., 1988], and on the other hand the spectral classification scheme used in CADIS. Thus, a morphological spiral galaxy can be classified as a starburst galaxy when it had a minor merger or a triggered burst of starformation in its recent history.

Note that due to the increasing space density of galaxies at higher redshifts, the merger rate and thus triggering events have been much more frequent than in the local universe. The high number of starformation galaxies seen in CADIS, supports the triggered star formation scenario.

3.1.4 Evolution of the luminosity function

The evolution of the galaxy luminosity function is of cosmological importance. In figures 3.12 and 3.13 the evolution of the luminosity function at different redshifts is superposed and the corresponding error ellipses are plotted. Evolutionary effects can best be traced by analyzing the figures with the error ellipses.

Studying the M^* dimension we find evolution in the bright end of the luminosity function. We have to take into account that in the local bin we miss the bright end of the population because the CADIS–fields are selected by the absence of luminous objects. This is represented in a large error ellipse in the M^* direction (plotted in red). Taking this into account there is a trend recognizable in M^* evolution for all galaxies.

In contrast, the starburst population (figure 3.12b) shows no evolution in brightness (M^*). All M^* measurements fall within 0.3^{m}, thus the galaxy population does not brighten significantly. Though it is possible that the single galaxies change luminosity over time, there is a natural upper limit to the increase in luminosity, leading to a constant balanced distribution in time.

Concerning the early type galaxies (figure 3.13) there is a weak but significant trend over time. M^* is evolving from high redshift until today to larger values, showing that the population becomes more and more luminous. In the E–S0–Sa population, this evolution is even larger and more pronounced than within the Sb–Sc galaxies.

There are different explanations where this increase of luminous galaxies comes from. The E–S0–Sa–Sb–Sc galaxies can brighten by triggered starburst or by accreting more material or new bright galaxies where formed by merging.

Another possibility is that this population is newly formed by mergers of large progenitor form the luminous E–S0–Sa–Sb–Sc or starburst population. Interesting is that as in galaxies cluster populations the lage elliptical form within the last 30% of the age of the universe.

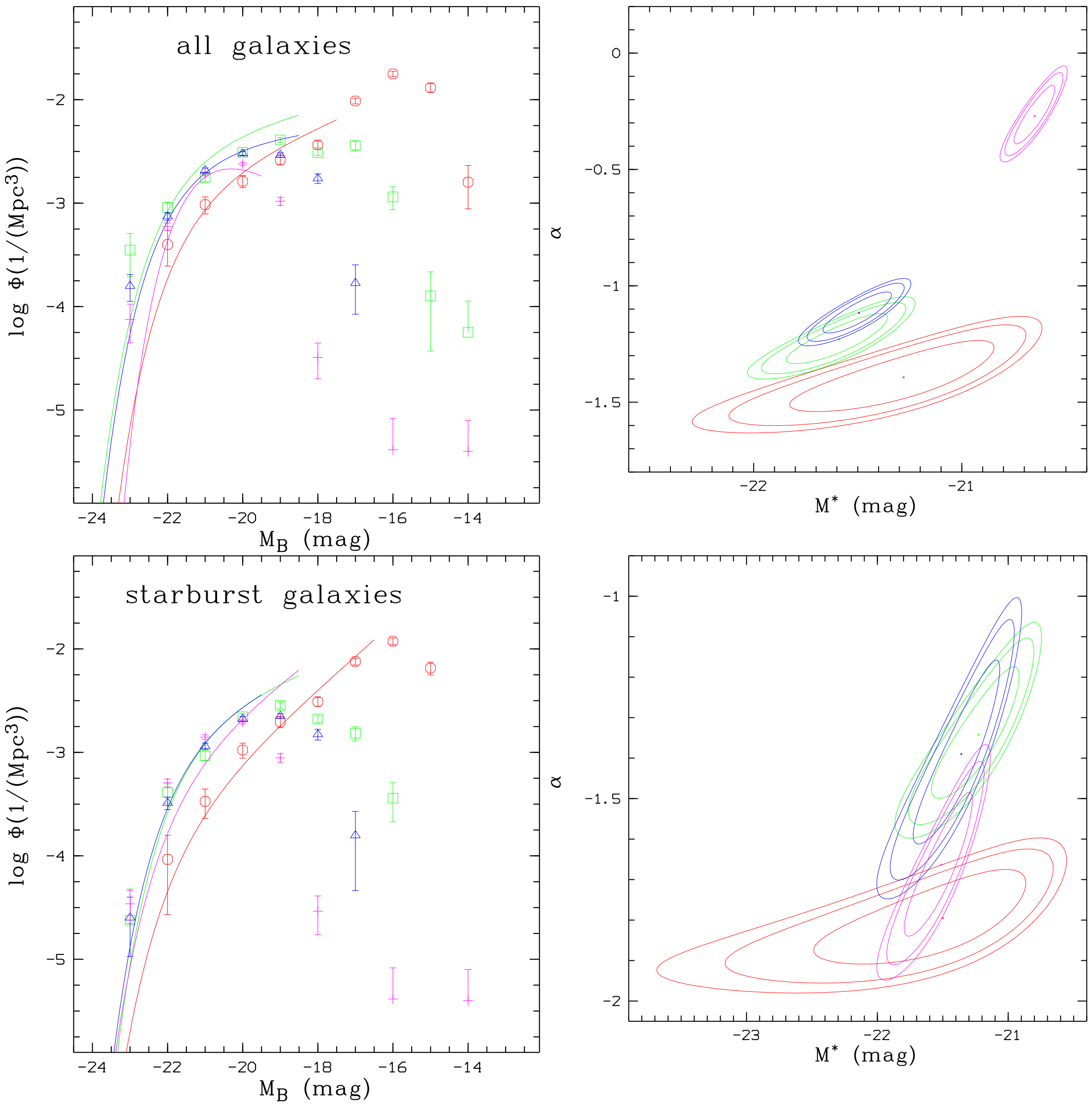

Figure 3.12: Evolution of the luminosity functions of different galaxy types: red local redshift ($0.1 < z < 0.3$), green low redshift ($0.3 < z < 0.5$), blue medium redshift ($0.5 < z < 0.75$) and magenta high redshift ($0.75 < z < 1.1$). Fitted STY parameters are combined in table 3.1.
a) [top left] All galaxies
b) [top right] Error ellipses for all galaxies with 1σ, 2σ and 3σ limits
c) [bottom left] Starburst galaxies (SED > 60)
d) [bottom right] Error ellipses for starburst galaxies with 1σ, 2σ and 3σ limits

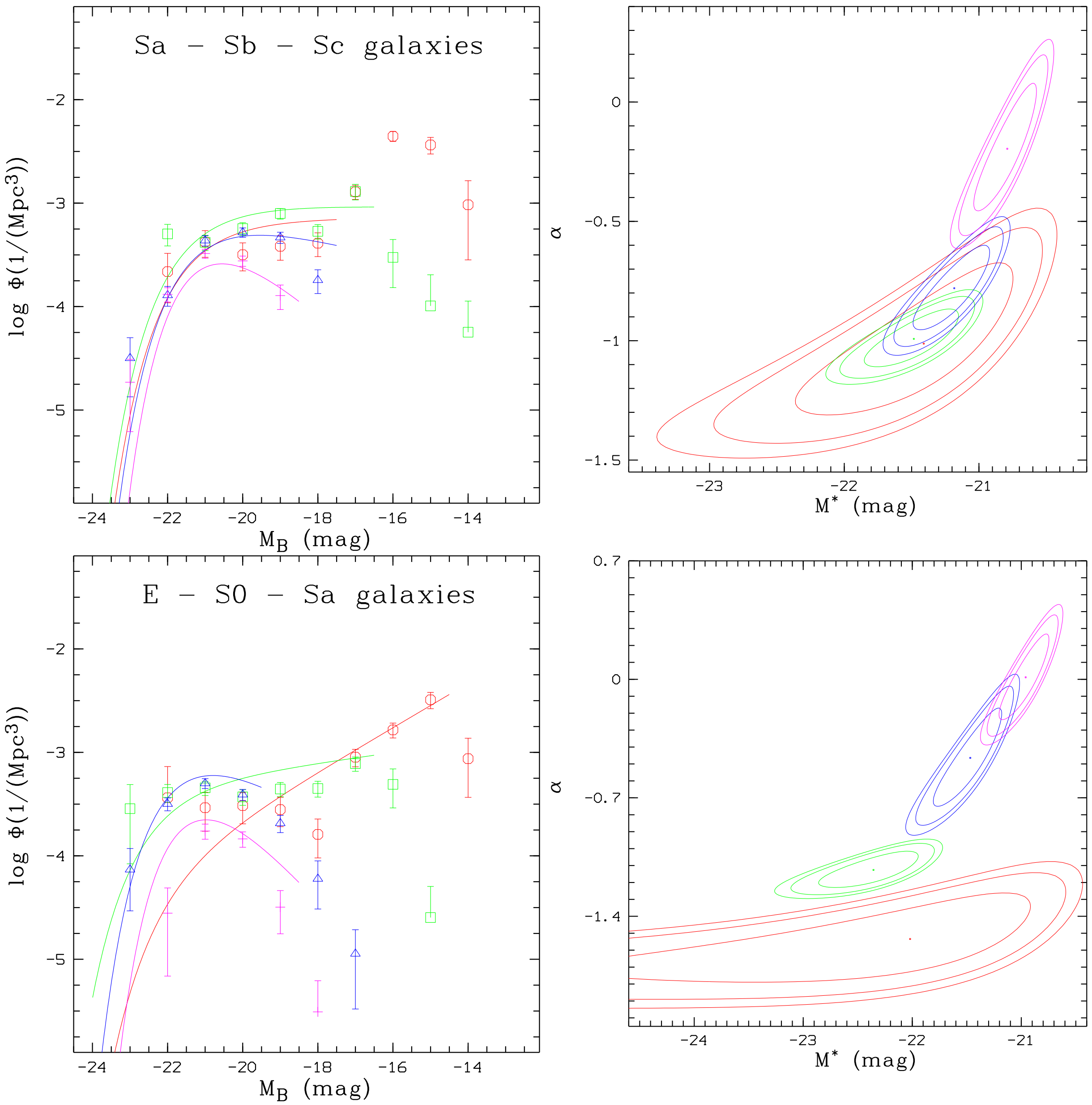

Figure 3.13: Evolution of the luminosity functions of different galaxy types: red local redshift ($0.1 < z < 0.3$), green low redshift ($0.3 < z < 0.5$), blue medium redshift ($0.5 < z < 0.75$) and magenta high redshift ($0.75 < z < 1.1$). Fitted STY parameters are combined in table 3.1.
a) [top left] Sb–Sc galaxies ($37.5 <$ SED < 60)
b) [top right] Error ellipses for Sb–Sc galaxies with 1σ, 2σ and 3σ limits
c) [bottom left] E–S0–Sa galaxies (SED < 37.5)
d) [bottom right] Error ellipses for E–S0–Sa galaxies with 1σ, 2σ and 3σ limits

3.1.5 Comparison with other work

Efstathiou [Efstathiou et al., 1988] and Binggelli [Binggeli et al., 1988] compared five magnitude limited redshift surveys (AARS, KOS, KOSS, RSA and CfA) and found a common luminosity function of $\phi^* = 0.0156 \pm 0.000341/_{\mathrm{Mpc}^3}$, $M^* = -19.68^{\mathrm{m}} \pm 0.01$, $\alpha = -1.07 \pm 0.05$ for $H_0 = (100\,\mathrm{km}/(\mathrm{sec\,Mpc}))$ with no evidence for differences in morphological types earlier than Sc. The luminosity function parameters of Efstathiou are in agreement with our results concerning M^*. Our determined α is higher than the one of Efstathiou et al. (-1.0 to -1.25), which is an effect of incompleteness in his survey data and due to the fact that Efstathiou et al. used an R–band selected sample.

Evolution in the luminosity function was already suggested by Lilly et al. based on a sample of 730 galaxies in CFRS [Lilly et al., 1995, Le Fèvre et al., 2000, Schade et al., 1999, Kauffmann et al., 1996]. Lilly et al. concluded that the evolution is strongly differential with color. They found a brightening from $0.2 < z < 0.5$ to $0.5 < z < 0.75$ by one magnitude for blue galaxies. Lilly et al. saw that the evolution saturates at the brightest magnitude at $1.0 < z < 1.3$ but continues at the faint end. We cannot find a change in the luminosity function at the bright end. All the luminosity functions of the three higher redshift bins from $0.3 < z < 1.1$ have the same slope and the error ellipses in the M^* dimension overlap. Lilly et al. used typically 90 galaxies in his bins (a maximum of 124 and at least 15) to derive the luminosity function. Our sample is by a factor of 4 to 5 larger. His luminosity function was fitted on 5 to 8 density points with a bin width of 0.25 magnitudes. Lilly et al. did not calculate any error ellipses or other error estimates, and made no statements about the statistical significance of their derived evolution.
For the red galaxies Lilly et al. found very little change in luminosity. The trend in evolution we found in CADIS data is significant for E–S0–Sa–Sb–Sc type galaxies.

In the CNOC2 survey Lin et al. [Lin et al., 1999] pointed out that the luminosity function depends on galaxy types, a conclusion which is supported by our analysis. No evolution for the blue galaxy luminosity function is found in their analysis. This is in agreement with our analysis.
Lin et al. derived a luminosity evolution for early types galaxy. Their evolution shows a brightening to high redshifts. In contrast to that we found a brightening towards low redshifts. For early type galaxies Lin et al. found an increasing density at the faint end with higher redshifts. We argue that completeness effects at the faint end are not yet solved, thus we do not make statements about the faint end slope α.
They used an R–band selected sample, and we interpret the difference found as a problem of this selection effect. By selecting in the R–band less early type galaxies are selected at higher redshifts. Unfortunaly, there are significant differences between the selection criteria for the determination of the luminosity function based on deep surveys. As emphasized by Ferguson and Mc Gaugh [Ferguson and McGaugh, 1995], these can lead to differences in the luminosity function parameters. Lilly also pointed out the importance of an I band selected sample [Lilly et al., 1995].

Lin et al.'s sample extends to a redshift of 0.55. He concluded from that data set a brightening of the early type luminosity function. When we analyze our data sample to that redshift only we obtain the same impression (figure 3.5). This is an effect of low number statistics and the absence of bright foreground objects in the selected CADIS fields. Lin et al. derived the Schechter function parameter M^* to be about half a magnitude fainter than ours which strengthens the impression that Lin et al. missed the bright end of the population. Another probable cause for differences are the K–corrections they applied. The fact that CADIS does not need a K–correction, and that we did not use any selection in the sample for this analysis, is one of the major advantages of the survey. Although, the differences between CNOC2 and CFRS results are discussed in Lin's publication, the true reasons for the differences remain unknown and could only be revealed by deeper and more homogenous statistical complete samples.

Ellis et al. found in the Autofib redshift survey an evolution of star forming–galaxies and no evolution of their quiescent galaxies. They found a faint end slope of α =–1.1 at low redshift and at $z = 0.5$ an $\alpha = -1.5$. [Ellis et al., 1996]. We already can find in the bin of $0.1 < z < 0.3$ an $\alpha = -1.8$ and argued before that this is a lower limit. Thus, we have strong evidence that previously measured slopes are too low because of incompleteness and improper estimation of the limiting magnitude.

In a previous analysis of the CADIS data set we found differing results [Fried et al., 2001]. The luminosity function of early type galaxies were within the error ellipses constant. A rising faint end population of the starburst galaxies was found, which was interpreted into overlapping error ellipses and a best fit of α =–1.282±0.209 at $0.3 < z < 0.5$; α =–1.857±0.168 at $0.5 < z < 0.75$ and α =–1.7271 at $0.75 < z < 1.04$.
The differences between the two analysis are:

- ▷ Today we have four CADIS–fields analyzed and this increased the statistics by 30% and produces smaller error ellipses.
- ▷ Previously, we used an B815 (I) magnitude limit of 23^{m}. Here we do not use any limit, such that all classified objects are taken into account.
- ▷ Different completeness corrections were used with different software solutions.
- ▷ We derived an individual observational limit for each object. In the former analysis this was done with the completeness correction, which was based on artifical spectra. Those spectra were identical with the template spectra of the classification with additional luminosity dependent noise.
- ▷ Different binnings in the sample in the SED dimension were used to represent E–S0–Sa, Sb–Sc and starburst galaxies. Today the bins are SED 0–37.3, 37.5–60, 60–99 in contrast to 0–30, 30–75, 75–99.
- ▷ Changes and improvements were implemented to upgrade the multi–color classification.

The reasons for the difference are not identified yet in detail and need further investigation.

Differences to other publications can also be due to the fact, that we use a spectral classification and other groups use a morphological classification of their objects. Thus, spiral galaxies can have the shape of a spiral, but had a minor merger and so is classified in our sample as a starburst galaxies, which can lead to different classification.

All this disagreement in the publications leads to the conclusion that there is still no common result found due to uncertainties in the analysis. We recommend that conclusions should be treated carefully until a larger data sample is available.

3.2 SED distribution

With the analysis of the luminosity function in section 3.1 we started to look at two dimensions of our data sample: the redshift z and the rest frame luminosity (M_{B}) of the galaxies. The information about the galaxy type, which is given in our data sample as well, was neglected or reduced to bins of E–S0–Sa, Sb–Sc, or starburst galaxies. We will now look at the SED in our observed galaxy sample in more details.

In figure 3.14a-c shows the dependence of the SED on redshift. In figure 3.14b we plotted the density of the data points from figure 3.14a in bins of $\Delta z = 0.1$ and $\Delta SED = 5$. It can be seen in the figure that the number of objects at high z (z > 1.2) decreases. This is due to the fact that we are reaching the observational limit at high z. In addition, there is a small decrease in numbers at lower redshift bins (z < 0.3) because of the pencil beam effect of the survey. To address the question whether the composition of the galaxy population changes with time (redshift), we have to normalize the population in each redshift bin in figure 3.14c to analyze the fraction of galaxy types for different redshifts.

Analyzing the normalized distribution in figure 3.14c shows that at every z we find that late type/starburst galaxies (SED 75 to 100) make up the main part of the field galaxy population. The small population of early type galaxies (SED < 45) is decreasing with higher redshift. In terms of time, the early type galaxy population is slowly developing and their percentage in the galaxy population is increasing with time.

When we look at the proportion of galaxies (P) as a function of look–back time ($t \propto \frac{z}{z+1}$), we see a decreasing proportion of early type galaxies in the past of our universe.
We find time dependencies (figure 3.15) of E–S0, Sa and Sb galaxies of the form:

$$\begin{aligned}
P\left(\frac{z}{z+1}\right) &= 5.92(\pm1.7) - 6.46(\pm4.4)\tfrac{z}{z+1} && \text{for E and S0 galaxies} \\
P\left(\frac{z}{z+1}\right) &= 12.0(\pm2.1) - 3.63(\pm3.5)\tfrac{z}{z+1} && \text{for Sa galaxies} \\
P\left(\frac{z}{z+1}\right) &= 22.1(\pm2.4) - 24.6(\pm6.0)\tfrac{z}{z+1} && \text{for Sb galaxies}
\end{aligned}$$

For this calculation we use the data points from figure 3.15. For the linear fit, we exclude the redshift bins z < 0.15 and z > 1.15, because our statistics are too low in these redshift bins (for illustration see the histogram over redshift — figure 3.16).

This decrease is neither new nor unexpected, because it needs time, several mergers and interior evolution to form early type galaxies. Naturally, the increase in formation of massive regular galaxies emphasizes the hierarchical models and stands in contrast to the classical *monolithic collapse* theory.

We will now study the luminosity of the different galaxy types (figure 3.17). Having normalizing each galaxy type (Δ SED = 5) with the total number of galaxies in that bin

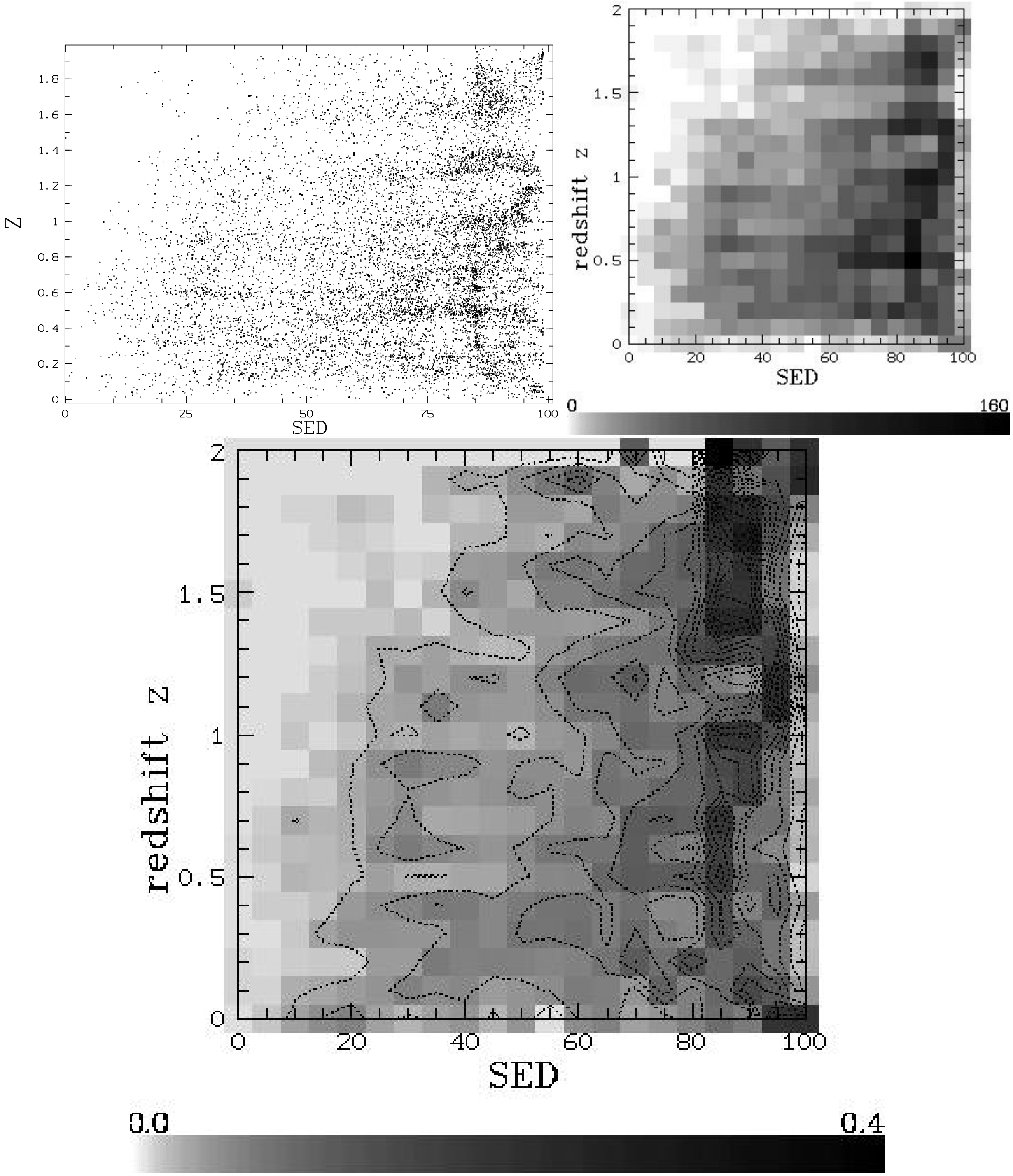

Figure 3.14: Spectral energy distribution (SED) versus redshift z
a) [top left] Simple assembly of the data points
b) [top right] Density of the data points from sub-figure a intensity is coded according to the bar from 0 to the maximal number of object in one bin (160)
c) [bottom] Density from b normalized to $\int = 1$ for each row (redshift bin of 0.1) intensity is coded according to the shown bar from 0 to 0.4

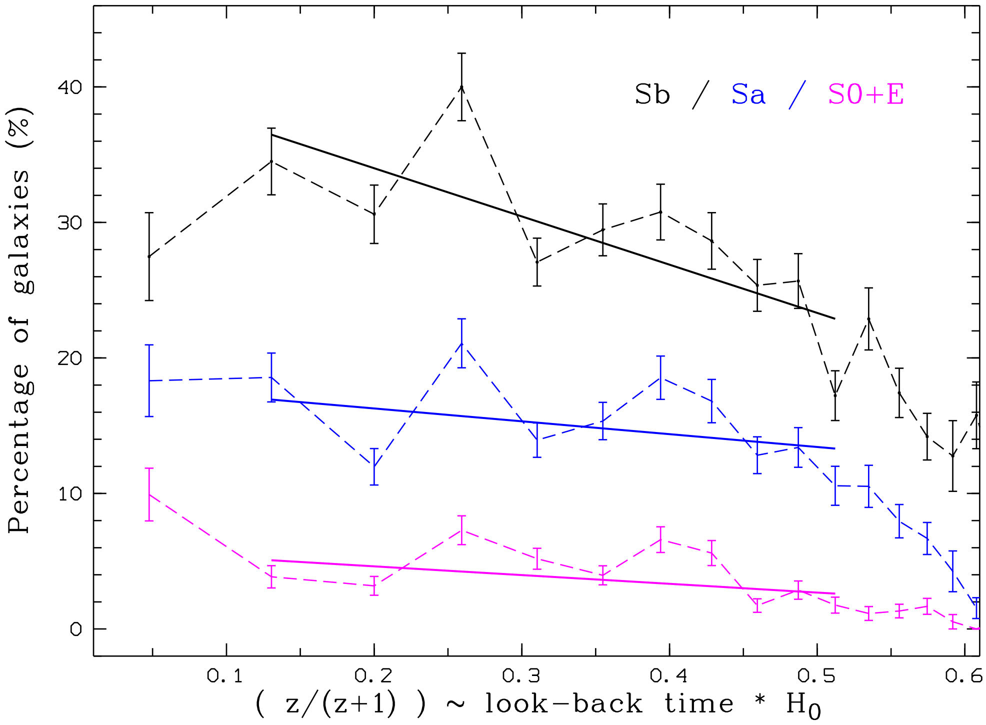

Figure 3.15: Percentage of E,S0, Sa and Sb galaxies in the galaxy population depending on look–back time ∼ (z/(z+1))

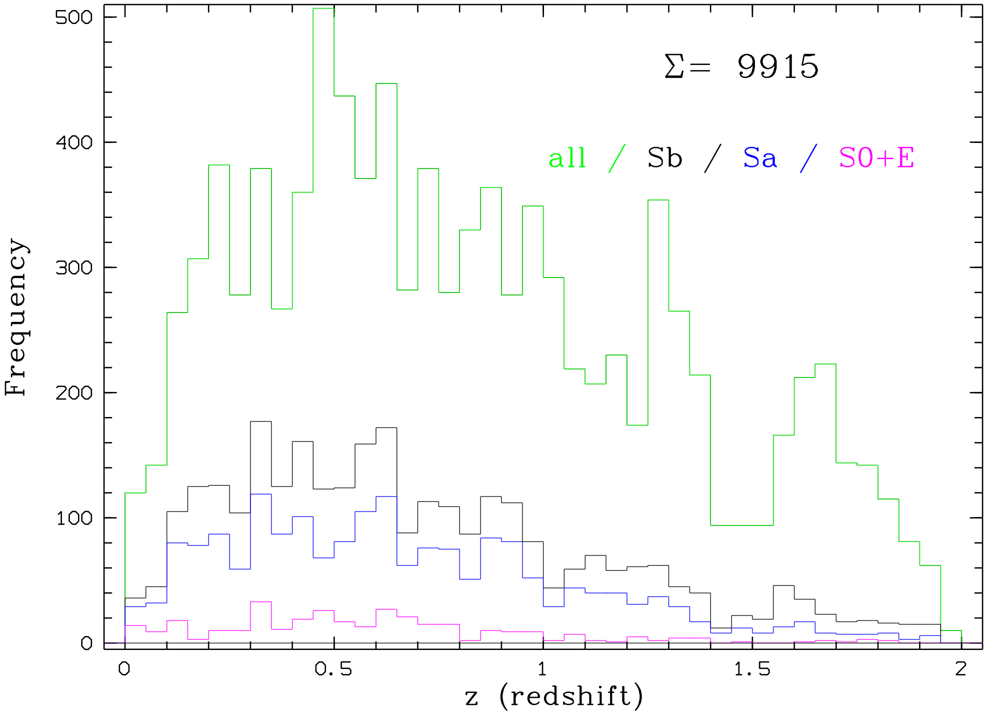

Figure 3.16: Histogram of the population of galaxies at different redshifts

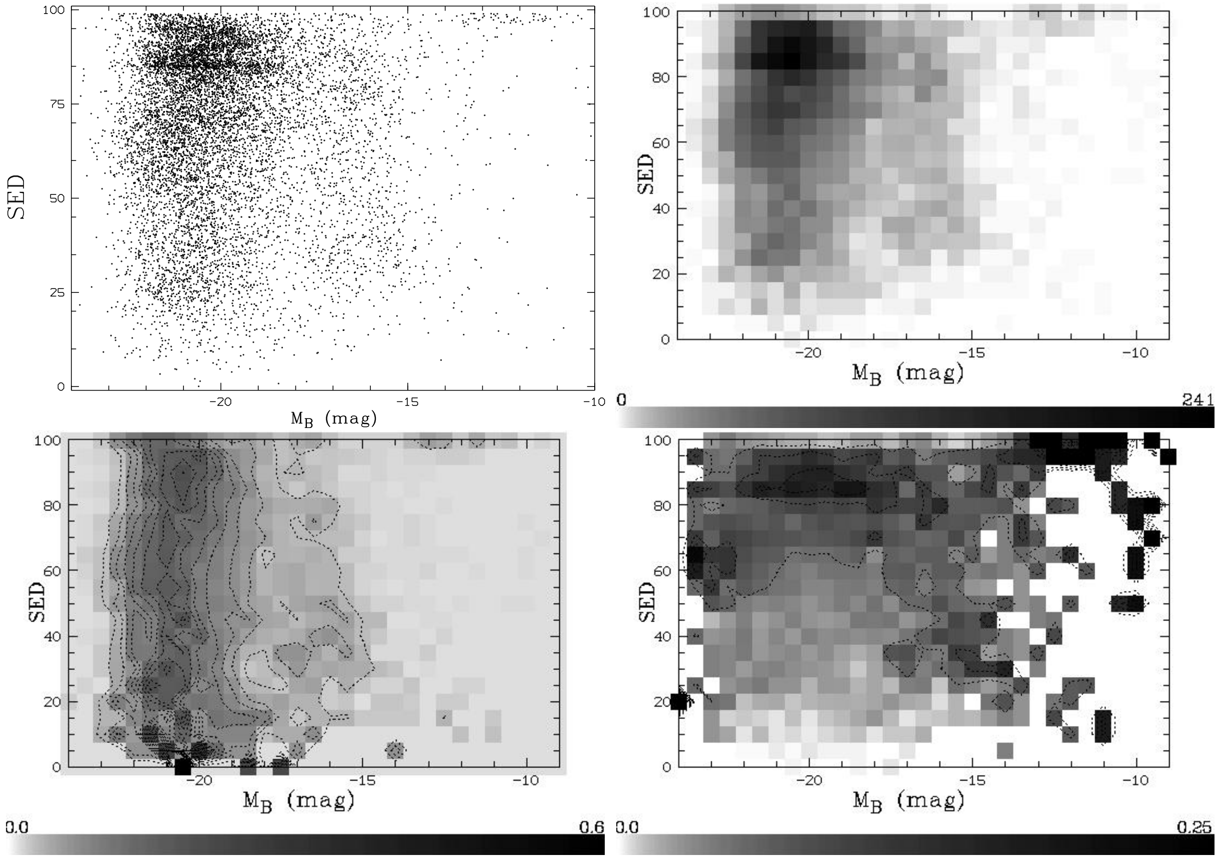

Figure 3.17: Spectral energy distribution (SED) versus absolute magnitude
a) [top left] Simple assembly of the data points
b) [top right] Density of the data points from sub-figure a ; intensity is coded according to the bar from 0 to the maximal number of object in one bin (241)
c) [bottom left] Density from b), normalized to $\int = 1$ for each row (SED bin of 5); intensity is coded according to the shown bar from 0 to 0.6
d) [bottom right] Density from b), normalized to $\int = 1$ for each column (magnitude bin of 1^{m}); intensity is coded according to the shown bar from 0 to 0.25

we derive figure 3.17 c. The largest number within each galaxy is found at amplitude of $M_{\mathrm{B}} = -21^{\mathrm{m}}$. The distribution is similar for each galaxy type. Absolute statements are in this context very difficult, because it has not been taken into account that the observational limit in the different redshift bins affects the data sample. But the appearance of the distribution remains the same even with absolute magnitude limited subsamples. The observational limit affects the counts for each galaxy type in a similar way, such that the peak in the luminosity population within each galaxy type remains around M^*. In figure 3.17d the population is normalized over each luminosity bin ($\Delta M = 0.5^{\mathrm{m}}$). In bins from magnitude -24^{m} to -9^{m} all redshift bins in the sample show a similar distribution. The majority of the galaxies has a SED around 85. This means that starburst galaxies dominate this population. At lower luminosities, there are as much early type galaxies

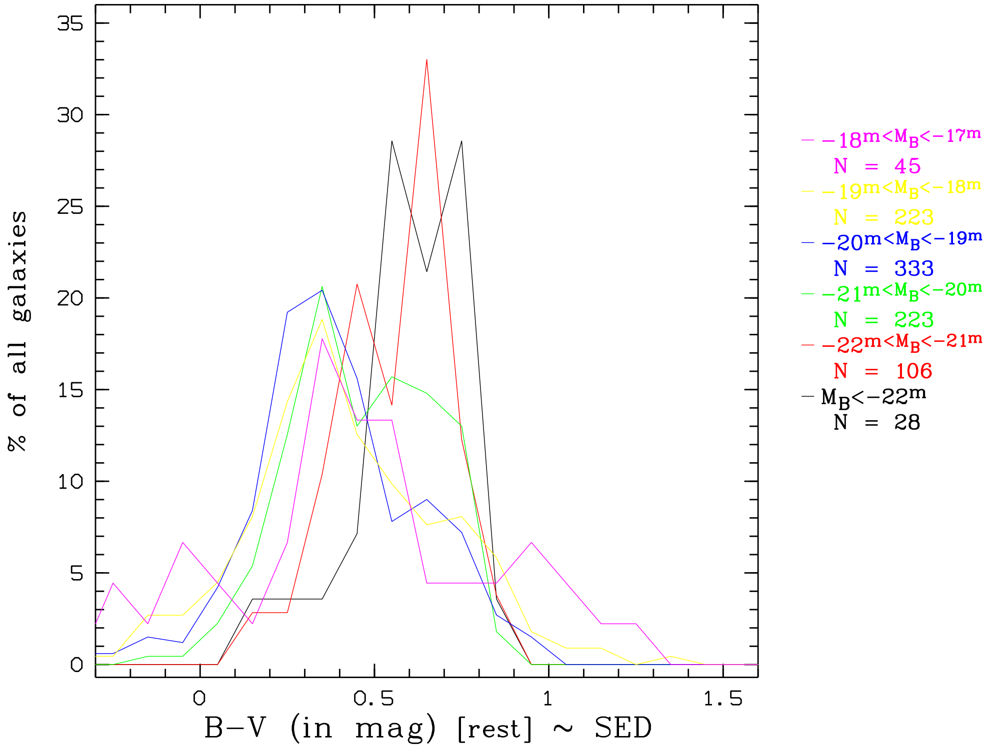

Figure 3.18: Color index B–V distribution at different luminosities in the redshift bin $0.3 < z < 0.5$

(SED 0–45) as late type galaxies (SED 75–99). This feature is an artefact, produced by the observational limit, as we miss many of starburst galaxies at high redshift.

We will finally analyze the SED distribution in dependence on absolute magnitude for a certain redshift bin. In figure 3.18, all galaxies between redshift 0.3 and 0.5 are taken into account. In the figure the rest frame color index of B–V is chosen to represent the SED. In the bins with high absolute magnitude most of the galaxies are red (E, S0, Sa, Sb, early type galaxies). At lower luminosity, the peak of the distribution is shifted towards blue color index. This is not unexpected, because according to theory of hierarchical galaxy formation, redder galaxies will thus tend to be larger and more luminous.

3.3 Color index

Another way to study galaxy evolution is to use the star formation activity as an indicator of the history of the galaxies. Therefore, we analyze the rest frame color index in our data set, because only with the rest frame magnitudes conclusions on the galaxy properties as stellar composition are possible. In the CADIS data sample the calculated rest frame filter magnitudes become less accurate as soon as the central wavelength is shifted into the infrared (compare section 2.2.2), we use a filter as blue as possible for the analysis. We

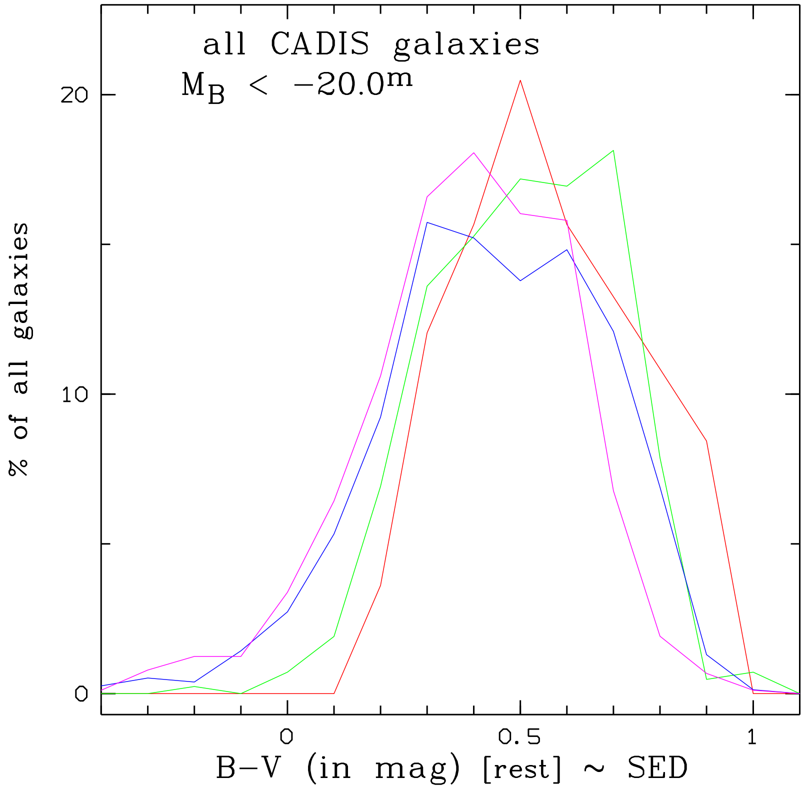

Figure 3.19: Distribution of B–V rest frame color index in different redshift bins (red $0.123 \leq z \leq 0.315$, green $0.315 \leq z \leq 0.539$, blue $0.539 \leq z \leq 0.799$, magenta $0.799 \leq z \leq 1.095$) in the CADIS data sample

choose the B–V rest frame color index. By analyzing the rest frame B–V magnitude we are just collapsing the detailed SED information in our data set to a single significant number. When the galaxy spectral template library is sorted from the most red to the most blue spectrum, a rest frame color index is an indicator for the SED.

3.3.1 B–V color index evolution

Rest frame Johnson B and V magnitudes were calculated using the interpolation method presented in section 2.2.2.1. From these rest frame magnitudes B–V color indices were derived. As we are working with a large sample, we are able to interpret the distribution of color indices within our observed galaxies. To avoid effects of incompleteness at the faint end of the population we use a limit in absolute magnitude of $M_B = -20^m$. This investigation is limited to redshifts lower than 1.1, because of uncertainties in the calculation of the V magnitude (compare table 2.5). The distribution is plotted in bins of 0.1 and normalized to the number of galaxies in each redshift bin (figure 3.19).

We can see in figure 3.19a shift in the B–V color index distribution in our galaxy sample with increasing redshift. In the subsamples with bins of $-21^m < M_B < -20^m$, $-22^m <$

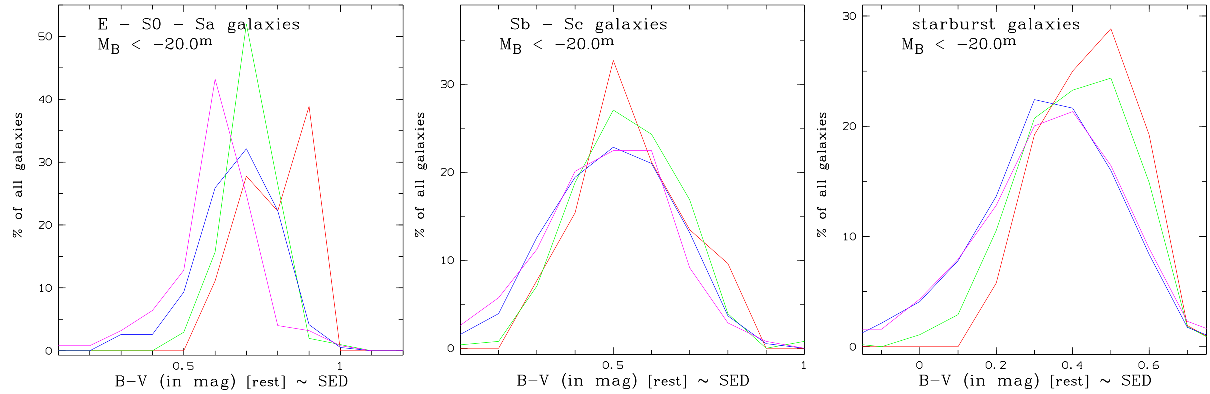

Figure 3.20: Distribution of B–V rest frame color index in different redshift bins (red $0.123 \leq z \leq 0.315$, green $0.315 \leq z \leq 0.539$, blue $0.539 \leq z \leq 0.799$, magenta $0.799 \leq z \leq 1.095$) separated in different galaxy types
a) [left] E–S0–Sa galaxies b) [center] Sb–Sc galaxies c) [right] starburst galaxies

$M_{\mathrm{B}} < -21^{\mathrm{m}} < M_{\mathrm{B}} < -21^{\mathrm{m}}$ and $-23^{\mathrm{m}} < M_{\mathrm{B}} < -22^{\mathrm{m}}$ the same results are found. This is interpreted as if galaxies become on average redder (larger B–V) in the continuum with age (more galaxies with smaller B–V at redshift around 1 and a shift of the distribution to higher B–V at redshift of 0.2.). This is not unexpected, because a young population of stars in the galaxies evolves into an older red stellar population in the present universe. It underlines the development of a population, dominated by blue starburst galaxies, to a population with galaxy types as E, S0, Sa, Sb and Sc.

Lilly et al. [Lilly et al., 1998] already noticed this trend in the CFRS[2] and LDSS[3] redshift surveys. He used a sample of 341 disk–dominated star forming galaxies that seems to get bluer (U–V) color with increasing redshift. To derive further information we divide the CADIS galaxy sample into E–S0–Sa (SED < 37.5), Sb–Sc ($37.5 <$ SED < 60) and starburst galaxies (SED > 60) and look at the B–V evolution in this three subsamples (figure 3.20). Most obviously is the E–S0–Sa galaxy subsample becomes blue with higher redshift. Nearly no trend can be observed in the Sb–Sc galaxy sample. An interpretation for this is, that the Sb–Sc galaxies since redshift one are in a status where the blue young star component has a constant fraction. In contrast to that the E–S0–Sa galaxies undergo in this period of the universe (redshift 1.1 to 0.1) a change and lose their blue young star component, because not enough dust is present to form new stars. Similarly do the starburst galaxies, but they undergo a less dramatic change. The starburst subsample is probably the best comparable to Lilly's results. We can confirm his conclusion that those galaxies were bluer at high redshifts.

Besides the presence of a blue stellar component another interpretation is possible. Interstellar medium within the observed galaxies can influence the color of a galaxy, thus different dust ratios within the galaxies can be the reason for different absorption effects.

---

[2] **C**anada–**F**rance **R**edshift **S**urvey named after the Canada-France-Hawaii Telescope

[3] A redshift survey using the multi slit LDSS-2 spectrograph on the William Herschel Telescope

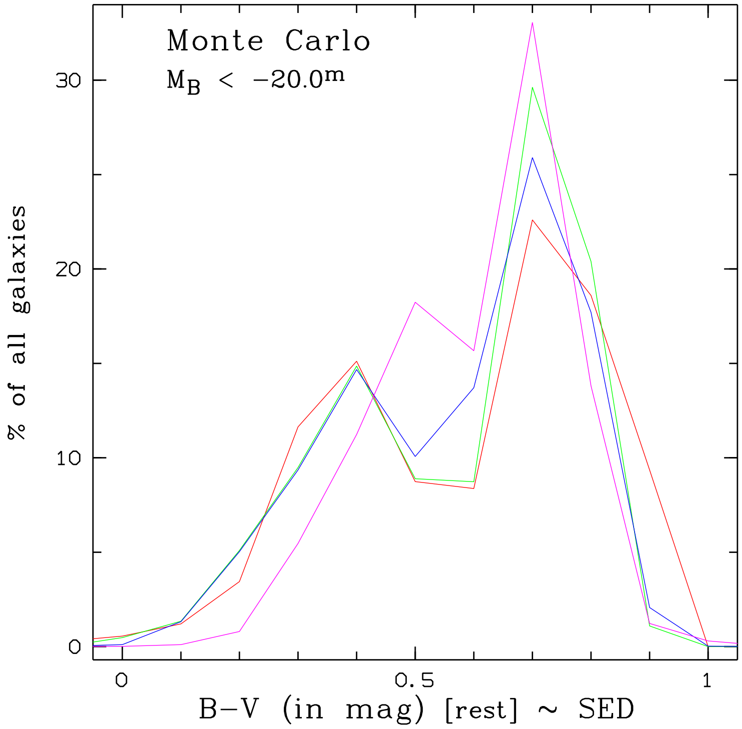

Figure 3.21: B–V rest frame distribution in a Monte Carlo set of galaxies at different redshifts coded in different colors (red $0.123 \leq z \leq 0.315$, green $0.315 \leq z \leq 0.539$, blue $0.539 \leq z \leq 0.799$, magenta $0.799 \leq z \leq 1.095$)

3.3.2 Test of the significance in B–V color index evolution

In this section we try to analyze possible artefacts in the B–V color index evolution found in the last section. Such a change in color index can be due to absorption effects in the interstellar medium of the Milky Way. The CADIS fields are located in IRAS minima (compare section 2.1 page 7) and in different directions of the sky so that such an effect should be minimized and canceled out. The effect has to be general as this reddening of the spectra can be recognized in subsamples of all single fields.

We also suspect our multi–color classification to pretend such color shift. To analyze this feature we used a Monte Carlo simulation of the multi–color classification. A sample of galaxies was generated homogeneously in redshift and absolute magnitude, consist of 30% E–Sc galaxies and 60% starburst galaxies. The simulated sample was classified in the same way as the CADIS data set, and the derived B–V color at different redshifts is plotted in figure 3.21. No evolution or shift to the blue of the distribution can be seen in the figure. The dual distribution in figure 3.21 represents the presence of equally distributed of early and late type galaxies in the simulated sample. Thus, we conclude, that the classification cannot pretend a reddening of the galaxies.

Chapter 4

Comparison with formation and evolution modeling

The CADIS data set contains a large number of galaxies with a wide range in redshift. This makes it ideal for comparison with simulations of galaxy evolution. To compare our observed data with theoretical models of galaxy evolution a collaboration with Mrs. Kauffmann was initiated.

In the first section we describe the semianalytically modeled galaxy sample, and then we describe the comparison of different aspects of model and observations in section 4.2.

4.1 Semianalytic models

In hierarchical theories of structure formation, galaxies, galaxy groups, and galaxy clusters form by continuous aggregation from small scale into larger and larger units. This scenario of structure formation in the universe is studied with computationally expensive numerical simulations. Galaxies are assumed to form by fragmentation and cooling of residual gas within the potential wells of dark matter haloes.

Kauffmann and White developed a semianalytic hierarchical method that efficiently simulates the structure–forming–process in the universe [Kauffmann and White, 1993, Kauffmann et al., 1993]. Based on the Press–Schechter formalism [Press and Schechter, 1974], circular velocity fields of haloes are used to trace the progenitor of a single halo. Thus, the algorithm starts with a statistical local (present) distribution of circular velocities of dark matter haloes and derives a progenitor distribution of dark matter haloes with a probability distribution [Bower, 1991] in steps of $\Delta z \approx 0.1$. The galaxies are positioned in space with a special algorithm according to their size. With the next step back in time the next generation of progenitors follows. Kauffmann et al. [Kauffmann et al., 1993] derive galaxy merging history trees based on the probability of possible assembly, valid only for ensemble statistics. Detailed descriptions can be found in Kauffmann et al. [Kauffmann et al., 1993, Coleman et al., 1980].

These non analytic steps were cross checked by Kauffmann et al. against analytic top to bottom hierarchical simulations which are computationally more expensive.

These simulations can thus model from circular velocities of local dark matter haloes galaxy evolution in a semianalytic way.
The free parameters after the initial dark matter circular velocity are in the simulations:

- Efficiency of star formation,
- Feedback efficiency of supernovae influence on the interstellar cold gas,
- Fudge factor in the dynamical friction merging rate,
- Ratio of the mass of the satellite galaxy to that of the central galaxy if an elliptical merger remnant is to be produced,
- Cosmological parameters $\Omega_0, \Omega_b, b, \Lambda$ and H_0.

Stellar population models [Rocca-Volmerange and Guiderdoni, 1988] with the merging the history tree of each galaxy give an estimation for the spectrum of the simulated galaxies. Gas content and cooling function, chemically consistent star formation, and feedback as well as passive evolution were incorporated to finally provide a code for simulating galaxy shapes and colors as well as large scale evolution for various environments [Kauffmann and White, 1993].

From Mrs. Kauffmann we obtained a data set with field galaxy populations in a volume of 125000Mpc^3. The tables contain apparent magnitudes BB, V522, R2, B815, B909 and BKp for the evolving population at different redshifts. The *snapshots* were taken at redshifts of $z = 1.02$, 0.87, 0.73, 0.60, 0.48, 0.37, 0.26, and 0.17. To ensure best consistency, we split the CADIS–observed data set in bins centered around these redshifts. The simulations were done for an Einstein–de Sitter universe ($\Omega_\mathrm{m} = 1$; $\Omega_\Lambda = 0$; $q_0 = 0.5$) and a Hubble constant of $H_0 = 50\,\mathrm{km/(sec\,Mpc)}$.

4.2 Comparison with CADIS data

4.2.1 Density of galaxies

In order to compare the density of galaxies we consider a subsample in which the CADIS data set is more than 96% complete in all redshift bins. Therefore, a rest frame magnitude

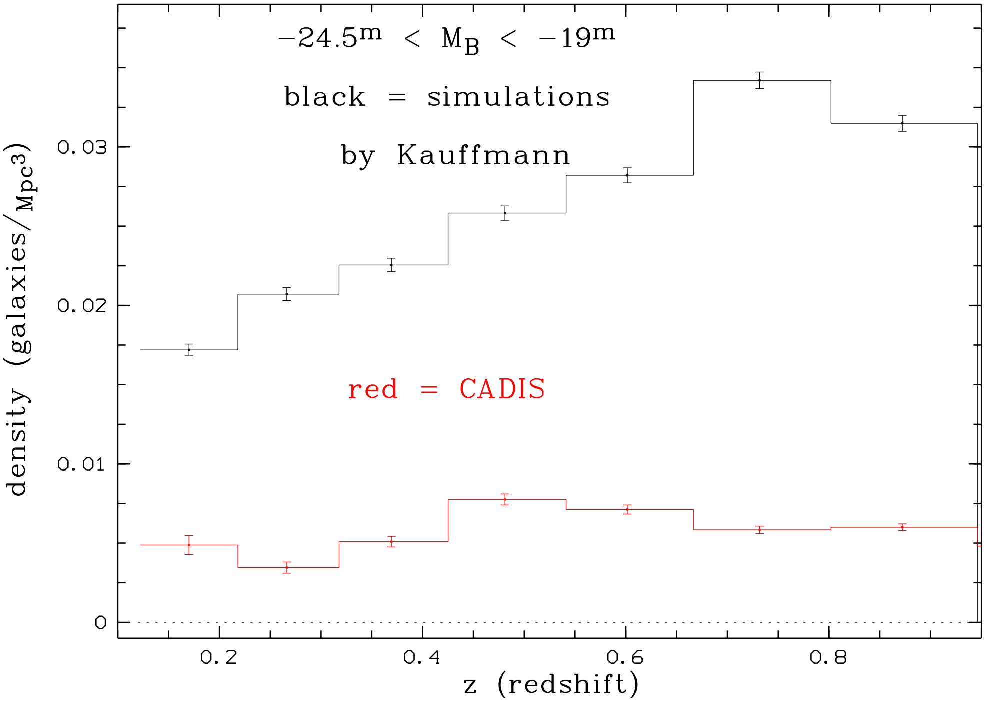

Figure 4.1: Density of galaxies in the comoving volume at different redshifts; black – Kauffmann simulated galaxy population
and red – the CADIS data set with an absolute magnitude limit

limit of $M_B = -19^{\mathrm{m}}$ was set. For the CADIS data the comoving volume of the pencil beam and for the simulated data a fixed volume of 125 000 Mpc^3 was used.

In the local redshift bin ($0.123 \leq z \leq 0.217$) the CADIS data set has a lower than average density, because the CADIS fields were chosen to be free of bright objects. Thus, the bright end of the population at nearby redshifts is not present in the CADIS sample. In addition, the statistics of the local population are small because of the small observed volume (pencil beam effect). The galaxy density in the Kauffmann simulations are a factor of four to five higher than in the CADIS observations at al. redshifts (figure 4.1). In the literature measurements are only available at the low redshift. Therefore we try to compare the densities with local measurements from the literature.
Lin et al. [Lin et al., 1996] found a local density of $\overline{\rho} = 0.029 \pm 0.002$ galaxies$\cdot h^3/\mathrm{Mpc}^3$ in a data sample of 18 678 galaxies of brightness $-23.0^{\mathrm{m}} \leq M \leq -17.5^{\mathrm{m}}$ (with $H_0 = 100\,\mathrm{km/(sec\,Mpc)}$).
Converting Lin's observation into our cosmology $H_0 = 50\,\mathrm{km/(sec\,Mpc)}$ yields, $\overline{\rho} = 0.0036 \pm 0.0003$ galaxies 1/Mpc^3. We find 66 galaxies in CADIS within $-24.5^{\mathrm{m}} \leq M \leq -19.0^{\mathrm{m}}$ at low redshifts ($0.123 \leq z \leq 0.217$). Thus, we compute a density of $\overline{\rho} = 0.0048 \pm 0.0006$ galaxies/Mpc^3 which is of the same order of magnitude, but do not agrees within the error bars. The differences can be due to cosmic scatter because of different observed regions in the sky. Also the fact that Lin et al. used an R–band selected sample can

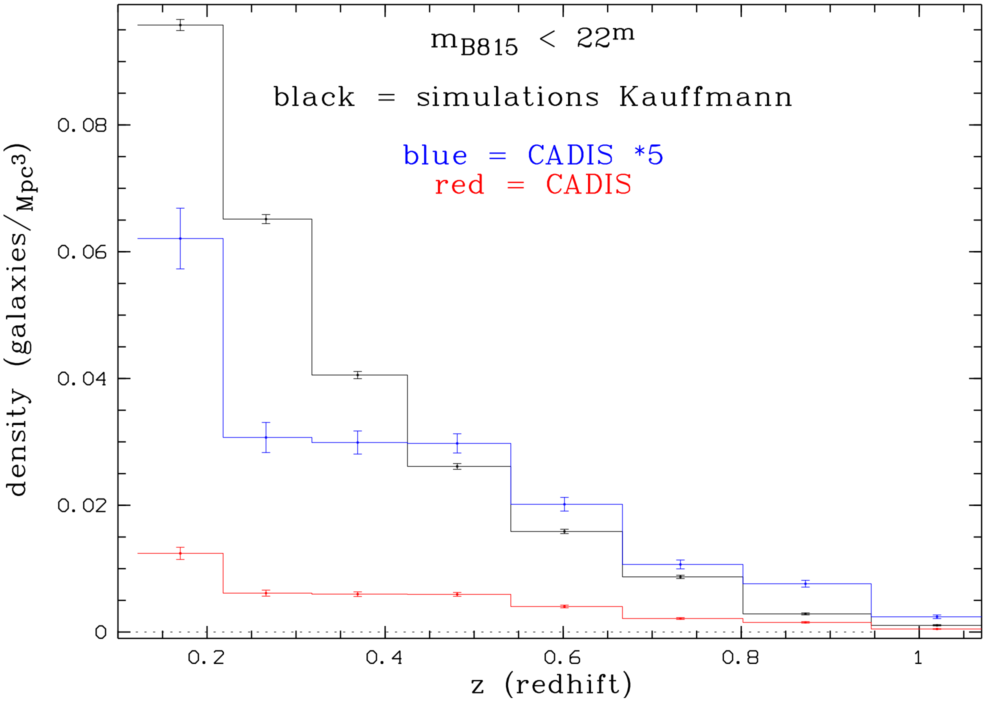

Figure 4.2: Density evolution in comparison:
CADIS observations (red) and scaled by a factor of 5 (blue),
Kauffmann simulations (black),
down to observed magnitude of $m_{B815} = 22^{m}$

be a reason for the different results. In the Kauffmann simulation, there are 2149 galaxies in the closest redshift bin (z = 0.17). This corresponds to a density of $\overline{\rho} = 0.0172 \pm 0.0004$ galaxies/Mpc^3 which is a factor of four higher than the observation.

4.2.2 Evolution in density

To compare the evolution of the density, we plotted the CADIS density and the density from simulations of Mrs. Kauffmann with a limiting apparent magnitude of $m_{B815} = 22^{m}$ in figure 4.2. The CADIS density was scaled by a factor of five in order to see the difference in the slope.

The slopes differ considerably. It seems that the frequency of merging is underestimated in these semianalytic model.

4.2.3 Luminosity function

In figure 4.4a-d we compare the luminosity function of the simulations with the CADIS data in the same bins. We plotted the Vmax data points with the corresponding fit. The bright end of the population is missing in the simulations and the population at the faint

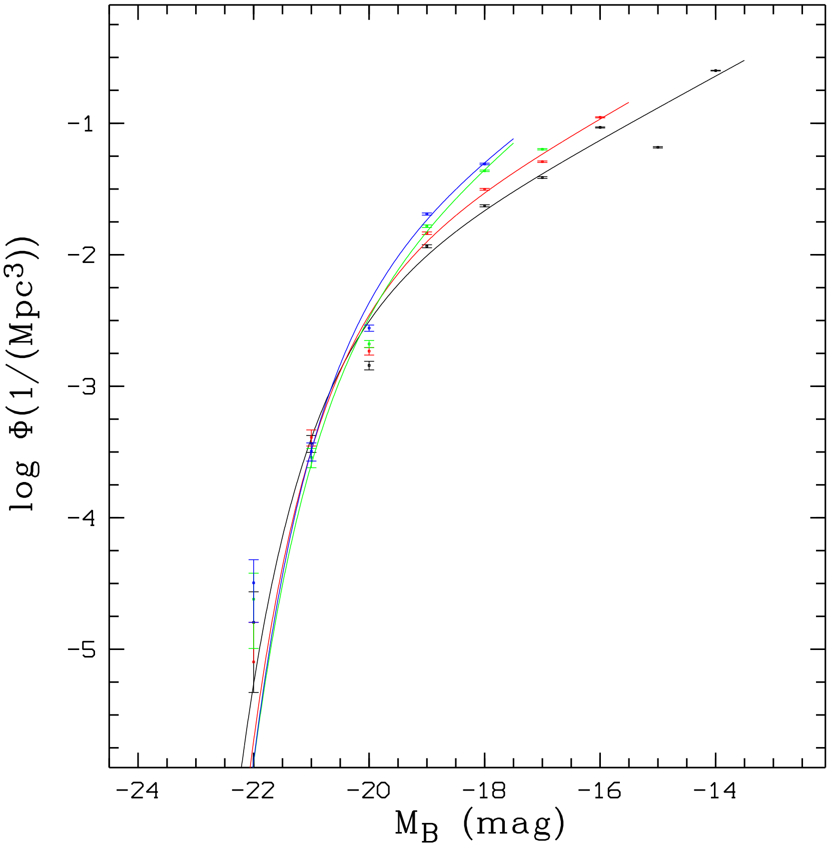

Figure 4.3: Evolution of the luminosity function in the hierarchical simulations by Mrs. Kauffmann
(**black** $0.123 < z < 0.315$, red $0.315 < z < 0.539$, blue $0.539 < z < 0.799$, green $0.799 < z < 1.095$)

end is overestimated at all redshifts. Differences to the observed CfA data set at the faint end has already been found by Kauffmann et al. [Kauffmann et al., 1993]. Small differences at the faint end could be due to low surface brightness galaxies missing the observations.

If we try to observe the evolution in the luminosity function in the simulated data (figure 4.3) we see an evolution in the faint end slope, getting steeper with higher redshifts. This is expected due to merging processes. The Density decrease at the bright end, has not yet to been explained.
In CADIS the evolution of the luminosity function is differential in galaxy types. However, we do not have information about different spectral types in the simulation. Therefore, a detailed comparison of the evolution cannot be done.

There is poor agreement with the Kauffmann simulations and the observed luminosity evolution in the CADIS data. Certainly, improvements have to be made to enhance physical understanding in the process involved in galaxy evolution.

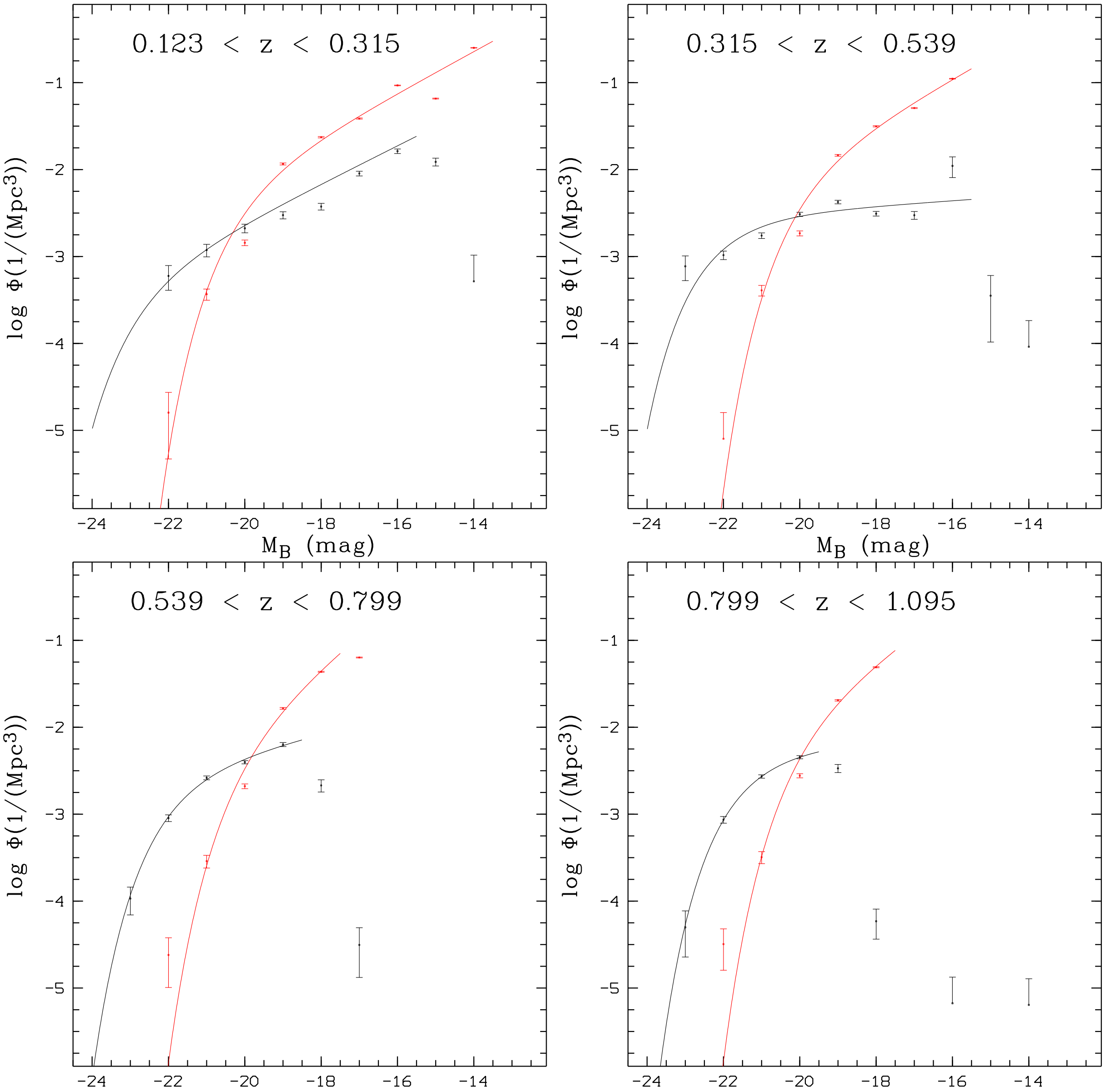

Figure 4.4: Comparison of luminosity function of hierarchical simulations (red) by Mrs. Kauffmann and **CADIS observations (black)**
a) [top left] Local redshift ($0.123 < z < 0.315$)
b) [top right] Low redshift ($0.315 < z < 0.539$)
c) [bottom left] Medium redshift ($0.539 < z < 0.799$)
d) [bottom left] High redshift ($0.799 < z < 1.095$)

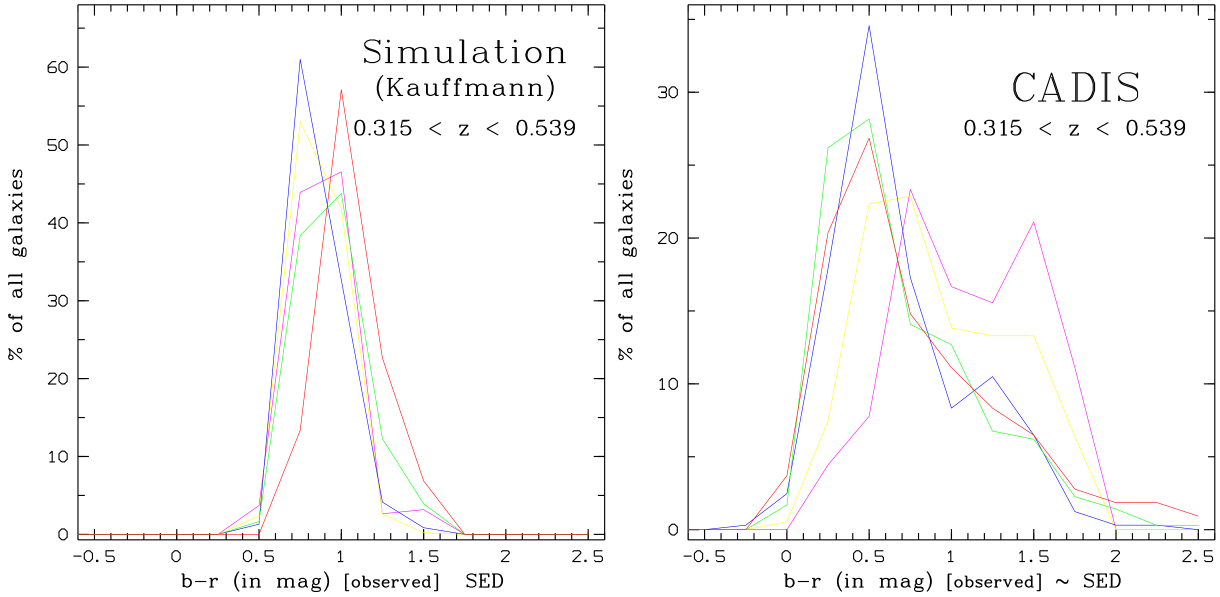

Figure 4.5: Distribution of the apparent color index b–r of
a) [left] Kauffmann simulation and
b) [right] CADIS observations
for different magnitude bins (magenta $M_B < -21.5^m$; yellow $-21.5^m < M_B < -20.5^m$; blue $-20.5^m < M_B < -19.5^m$; green $-19.5^m < M_B < -18.5^m$; red $-18.5^m < M_B < -17.5^m$)

4.2.4 Distribution of the apparent color index b–r

The distribution of the color index b–r of the apparent magnitude for the simulated population of galaxies and CADIS observations at redshifts of 0.429 (which means $0.315 < z < 0.539$) is shown in figure 4.5a. About 50 to 60 % of the simulated galaxies fall into a single bin (±0.125), meaning that they all have the same color index. In contrast, the CADIS observations show a large variety of color indices which represent a wide range of color indices, SEDs and galaxy types at that period of time in the universe. The CADIS observations show that at higher absolute magnitude the population is dominated by red galaxies with higher b–r (figure 4.5b). High b–r indicates a red galaxy and can be identified with early type galaxies E, S0, Sa, Sb. In the bins with lower luminosity more and more starburst galaxies are present in the population (lower b–r).

We classified the simulated data set with the multi–color classification algorithm used for the CADIS data (section 2.1 page 7). We obtain that the distributions of galaxy types are different in simulation and observation for several redshift bins, for example at redshifts of 0.945 to 1.095 (figure 4.6a and b). The population of early type galaxies is underestimated in the model. The observed starburst population in CADIS is wider in range ($70 <$ SED $<$ 99) and does not accumulate at a single SED (here 75). A solution for this problem would

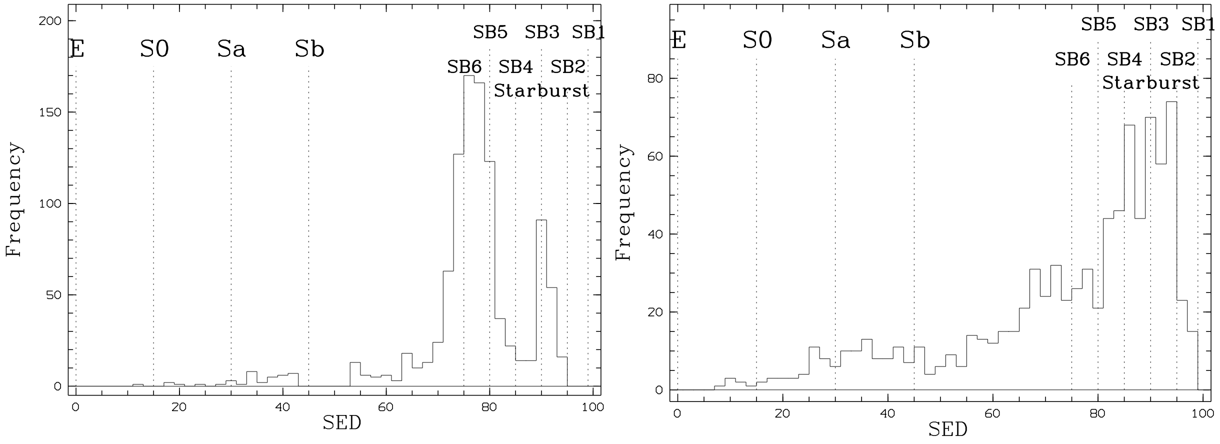

Figure 4.6: Distribution of the SED of galaxies at redshifts 0.945 to 1.095 (histogram)
a) [left] in Kauffmann simulations
b) [right] in CADIS observations

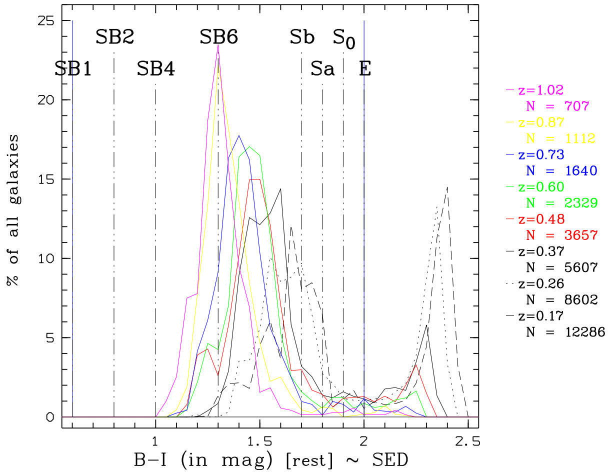

Figure 4.7: Rest frame color index B–I of the simulated data set for different redshift bins and, in comparison, the B–I color indices of Kinney et al. spectra [Kinney et al., 1996]

either be a variation of the fixed time steps in the galaxy generation model, or the definition of wider range of input velocities to allow a wider spread in the resulting evolutionary state of the modeled galaxies. Such that not 90% of the galaxies being in the same evolutionary state. The galaxies in certain redshift bins would then not all have the same age and stellar population, and thus would show different spectra.

4.2.5 Rest frame color index B–I

In figure 4.7 we see the distribution of the rest frame color index B–I. This index is used because it has the largest wavelength baseline across the spectrum, and effects of different galaxy spectra can be identified best by differences in their B–I color index.
The simulated galaxies show a color index (B–I) ranging from 1 up to 2.5 (color curves in figure 4.7). A bimodal distribution can be found in the galaxy population. The starburst galaxies in populations at high redshifts (magenta at z = 1.02 a peak around B–I = 2.4^{m}) evolve to a bimodal population at z < 0.4 with comparable high numbers of early type galaxies (high B–I) and starburst galaxies (low B–I).
But the population of early type galaxies in CADIS at z = 1.03 is not zero as shown in figure 3.15. It extends up to a redshift of 1.5. This is in contradiction to the simulated data set.

It can also be seen from figure 4.7 that neither in CADIS nor in the spectra of Kinney et al. there are observed galaxies with a B–I higher than two (E galaxy). The whole population in the simulation seems to be shifted towards a higher B–I color index by 0.5 magnitudes.

This can be due to an overestimation of the color index B–I in the simulated galaxies in general, because the stellar population in the galaxies was not evaluated correctly. An overestimate of dust reddening in the simulated galaxies may be another explanation for this effect.

4.2.6 Rest frame color index B–V

In the CADIS data set we analyzed the B–V rest frame color index (section 3.3.1 page 72). We performed the same analysis in the simulations to compare the results.

One way to determine the composition of the galaxy population is to use the B–V rest frame color index as in section 3.3.1. In the simulated data set we have the possibility to calculate the Johnson B and V absolute magnitudes with the interpolation procedure described in section 2.2.2. A rest frame B magnitude limited sample was selected in the same way as in the CADIS analysis in figure 3.19. The same magnitude limit ($M_{\mathrm{B}} < -20.0^{\mathrm{m}}$) as in section 3.3.1 was chosen to eliminate effects of incompleteness at the faint end of the distribution at higher redshift.

Figure 4.8 shows the distributions of the B–V color index at different redshifts in the simulations. An evolution of the population towards a redder galaxy population at lower redshifts is observable within the three colored redshift bins. We find the same trend as in the observed data (section 3.3.1), but the bin with redshift, $0.315 < z < 0.539$ (black dotted line) breaks that trend.

Determining the absolute V and B magnitude without the observed V522 filter as an interpolation point for the absolute magnitudes, the reddening effect of the galaxy population

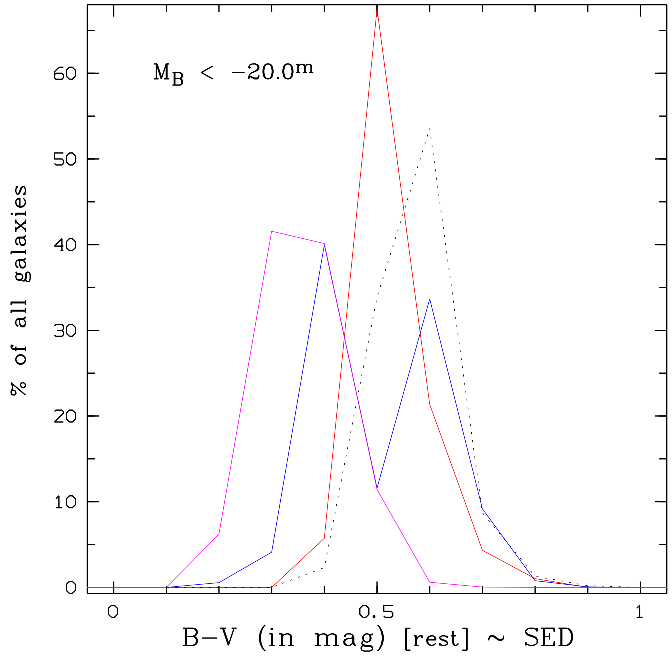

Figure 4.8: Evolution of the distribution of the simulated galaxies rest frame color index B–V in simulations of Kauffmann et al. (red $0.123 < z < 0.315$; **black dashed** $0.315 < z < 0.539$; blue $0.539 < z < 0.799$; magenta $0.799 < z < 1.095$)

can be confirmed (figure 4.9b). This brings ups to the conclusion that the analysis of the V522 filter measurements have a not yet identifiable problem in the simulations and should be taken out of the analysis.
Additionally, we try to find a evolution of the B–I filter index. Not forgetting the low confidence level in the rest frame Johnson I calculation, we analyzed the B–I rest frame magnitude in the simulations (figure 4.9a). This figure underlines the trend towards a redder galaxy population at lower redshift.

We come to the conclusion that the simulated data of Mrs. Kauffmann confirm the observation that galaxies have a smaller young blue stellar component at low redshifts, or that the blue galaxies tend to die out in the local universe.

4.3 Conclusions

Semianalytical modeling by Kauffmann et al. can provide clues to some effects in galaxy evolution, but is still far from reproducing the observed galaxy population at medium redshifts. The trend that the galaxy population get redder at lower redshift can be found in CADIS observations and simulations of Kauffmann et al.. Properties like local density, density evolution, luminosity function and variety of spectral energy distribution show differences. Comparison with the CADIS data revealed that the Kauffmann simulations

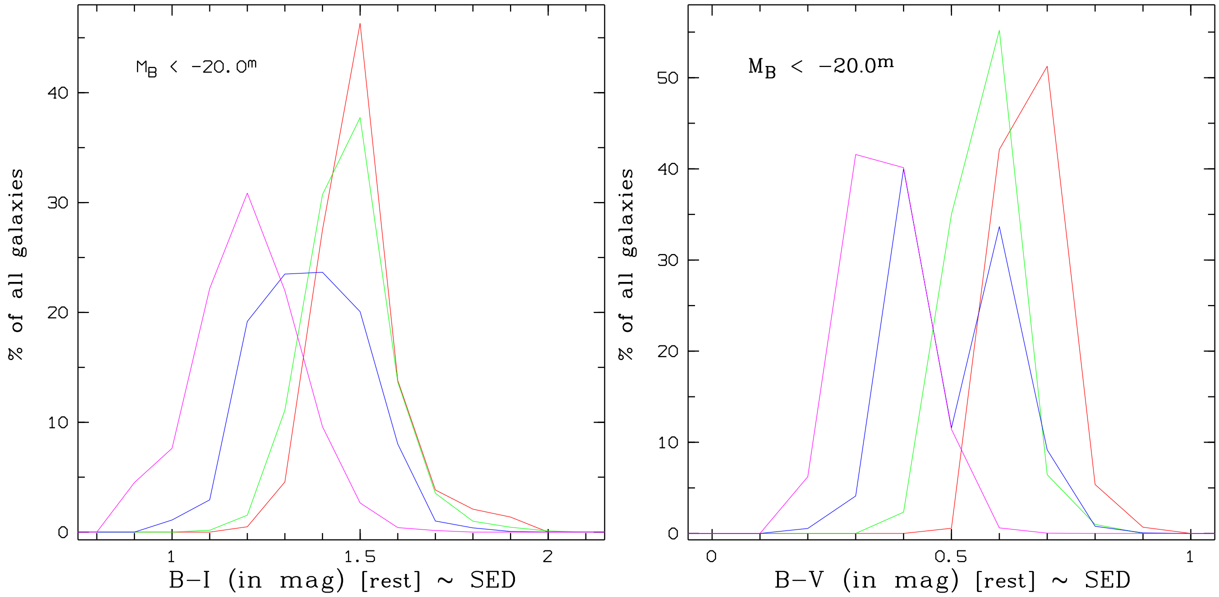

Figure 4.9: Evolution of the distribution of the simulated galaxies rest frame color indices
a) [left] Distribution of the simulated galaxies rest frame color index B–I (Johnson) at different redshifts
b) [right] Distribution of the simulated galaxies rest frame color index B–V calculated without using observed filter Johnson V for interpolation. (magenta $0.799 < z < 1.095$; blue $0.539 < z < 0.799$; green $0.315 < z < 0.539$; red $0.123 < z < 0.315$)

do not seem yet to be appropriate for describing galaxy evolution.
For further analysis a set of simulated data must be produced which are more similar to the observation. No conclusions on luminosity function evolution of different types of galaxies can be drawn with an acceptable confidence level without this.

Chapter 5

Comparison with modeled spectral evolution of galaxies

5.1 Chemically consistent evolutionary galaxy models

Recently, many efforts have been made in developing theoretical models of galaxy evolution and deriving spectra for evolving star systems. However, modeling galaxy spectra is a challenging work due to the high complexity of these systems. Many parameters are involved, for instance: star formation history (triggering and feedback), gas distribution, absorption and cooling, or dark matter component. Furthermore, environmental influences and stellar dynamics do not allow a general solution.

An approach has been developed by the group around C. S. Möller and U. Fritze-von Alvensleben [Möller et al., 2001] at the University of Göttingen. In a collaboration they provided us with their latest chemically consistent spectrophotometric evolutionary synthesis models. Their derived spectra are a step towards a more realistic modeling of galaxies. We used them as templates for our classification (section 5.2). Here we will first discuss their spectra and compare them to the observational ones of Kinney et al. [Kinney et al., 1996].

Figure 5.1 shows a subsample of the evolutionary spectra in the range of 1 to 18 Gyears in steps of 1 Gyear.E\ S0, Sb and Sd galaxies are presented. A depletion of the young blue stellar component with increasing age of the galaxies is clearly visible. There is no additional trigger for star formation, like merging processes, included in the calculation. The star formation histories taken into account for the different spectra are:

▷ An exponential decrease in star formation for elliptical galaxies

$$SFR\,(t) = \frac{M_t}{7.8 \cdot 10^8 \, e^{\frac{t}{1 \cdot 10^9}}}$$

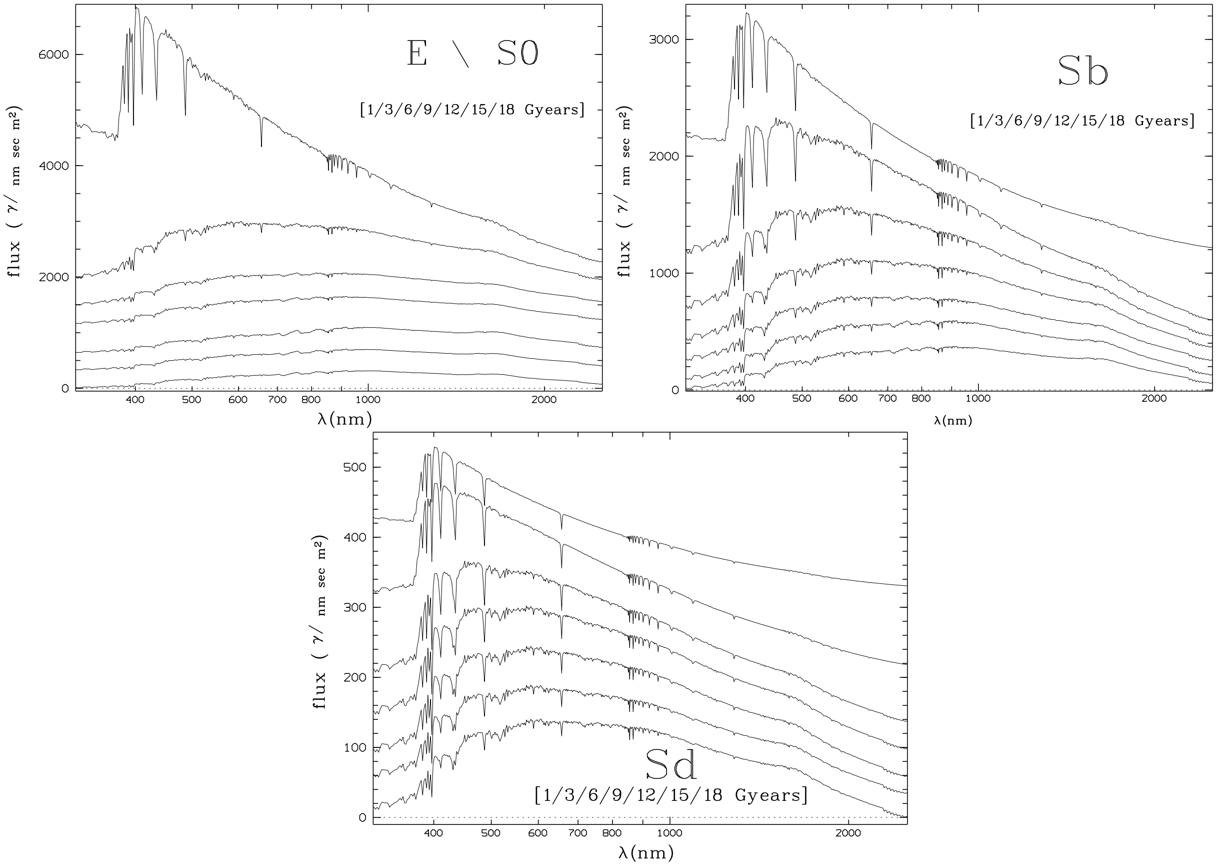

Figure 5.1: a-c Spectral evolution of galaxies according to the chemically consistent spectroscopical evolutionary synthesis model of C. S. Möller et al. in various time steps. The evolution of the galaxies is plotted from top to bottom.
(The flux values are shifted with a constant offset to provide a clear view on the full spectra and exclude overlap, thus this does not represent absolute brightness evolution.)
a) [top left]E\ S0 galaxies
b) [top right] Spiral Sb galaxies
c) [bottom center] Sd galaxies

▷ A gas dependent star formation for spiral galaxies:

$$SFR\,(t) = \frac{x}{1 \cdot 10^9 \cdot M_G(t)}$$

▷ A constant star formation for Sd galaxies:

$$SFR = \frac{7 \cdot 10^{-2}}{1 \cdot 10^9 \cdot M_t}$$

with

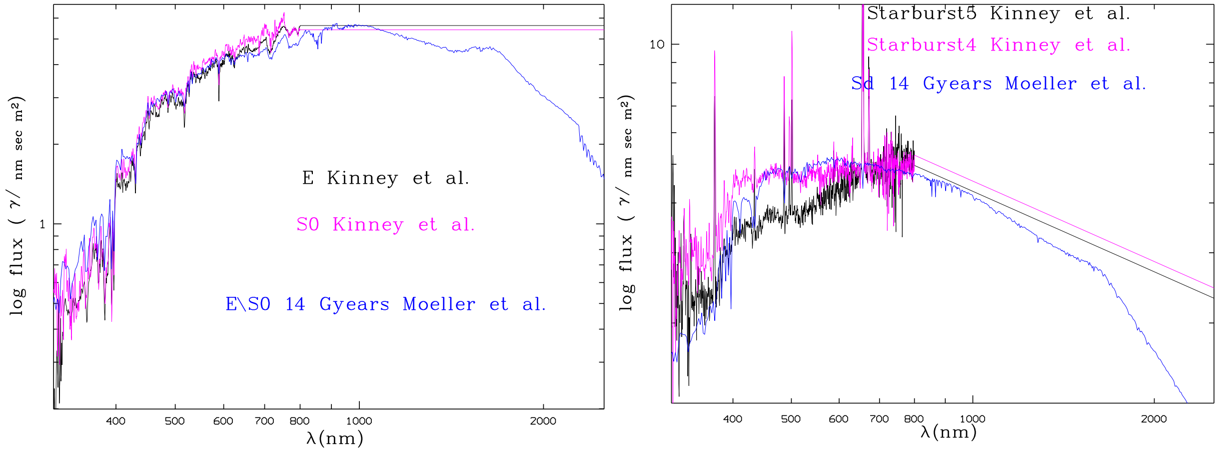

Figure 5.2: Comparison of observed averaged Kinney et al. spectra and synthetic model of C. S. Möller et al. [Kinney et al., 1996, Möller et al., 2001]
a) [left] A 14 Gyears old E\S0 synthetic modeled spectrum compared to observed E and S0 galaxies
b) [right] A 14 Gyears old Sd galaxy compared to a starburst 4 and starburst 5 galaxy spectrum of Kinney et al.

- ▷ ***SFR:*** star formation rate in solar Masses per year,
- ▷ ***t:*** time in Gyears since the initial star formation period in the galaxies,
- ▷ $\boldsymbol{M_t}$**:** total mass in solar Masses,
- ▷ $\boldsymbol{M_G}$: gas mass in solar Masses,
- ▷ $\boldsymbol{x}$**:** $x = 1$ for S0; $x = 0.2$ for Sb.

However, the synthetic spectra are calculated for complete galaxies [Möller et al., 2001], whereas our observed intensities are central magnitudes and limited to the fixed aperture of the CADIS photometry (section 2.2.1 page 15). At lower redshift the angular dimensions of the galaxy exceed the fixed aperture. Therefore, we have to restrict our sample to higher redshift to ensure that we collect all the light of the observed galaxies. At a redshift of 0.1 galaxies larger than 6kpc extend our aperture [Kayser et al., 1997]. But at $z = 0.3$ our aperture covers 14kpc and so 90% of the derived fluxes should represent the whole galaxies.

Although the spectra of C. S. Möller et al. were already checked against the observations of Kinney et al. [Möller et al., 2001], we compare the slopes in figure 5.2. By plotting the simulated E\S0 against the Kinney E and S0 spectra (figure 5.2a) we find a similar slope in the ultraviolet and optical wavelengths. In the infrared discrepancies are increasing. This is not unexpected, if we recall that the extensions into the infrared of Kinney spectra as used in CADIS data analysis were based on a simple approximation (section 2.1 page 13), because the infrared has a low impact on the classification (section 2.1). Reviewing

the spectra of CADIS objects in figure 2.11b the calculated spectrum of C. S. Möller is a better fit to the data.
The Sd galaxies spectrum of C. S. Möller et al. can not be well fitted by observed spectra of Kinney et al.. The 4000Å break is not well reproduced in the simulation. This may be due to the fact that starburst galaxies are not described by constant star formation only and an additional recent starburst is necessary to reproduce those spectra.

5.2 Multi–color classification with evolving galaxy spectra

The aim is to gather further information on the observed galaxies by fitting their ages. We classified the observed objects with a new template set. This template set has as redshift, SED, and as an additional dimension, the age of the galaxies. Of course, we have less information in the dimension of SED, because only 3 different galaxy types exist in the calculations from Göttingen. We treated the provided Sd spectrum as a starburst spectrum from Kinney et al., but without the emission lines. As a first approximation, the difference is not critical, because the emission lines only affect one or two filters, which impact compared to the remaining 12 to 15 correct filters should be low.

We used the following setup to distribute the spectra in the template library:

Spectrum	E\S0	-	Sb	-	Sd
SED	0	-	5	-	10

Based on this setup we developed a set of 39 798 galaxy templates for multi–color classification with 200 redshifts (0 to 2.0 in steps of 0.01), 11 SEDs (0 to 10 see above), and 18 age steps (from 1 Gyear to 18 Gyears in steps of 1 Gyear).

We classified all 12 245 detected CADIS objects with this new template set. To check the confidence level of this classification, a subsample of 160 objects with spectroscopic redshifts was used, similar to the test of the multi–color classification procedure described in section 2.1. Note that the same steps for the classification with Kinney spectra were done in section 2.1, figure 2.18 page 35. The spectroscopic redshifts compared to the derived photometric redshifts are shown in figure 5.3a. We find a standard deviation in z of 0.14, but not a central peak around zero in the histogram of the deviation in z (figure 5.3b).
The existing data show a problem in the classification mainly at low redshifts ($z < 0.3$). There are three major possible reasons: classification of objects in the wrong redshift bin because of misidentification with a wrong SED, or problems with the template library. The library could be incomplete or the spectra are different from the observed photometric spectra. Finally the influence of the Of course a better statistics would be necessary in this context.

For further conclusions we compare the results of the two classifications with each other (figure 5.4a and b). A well–determined correlation in the two z estimates provides a high

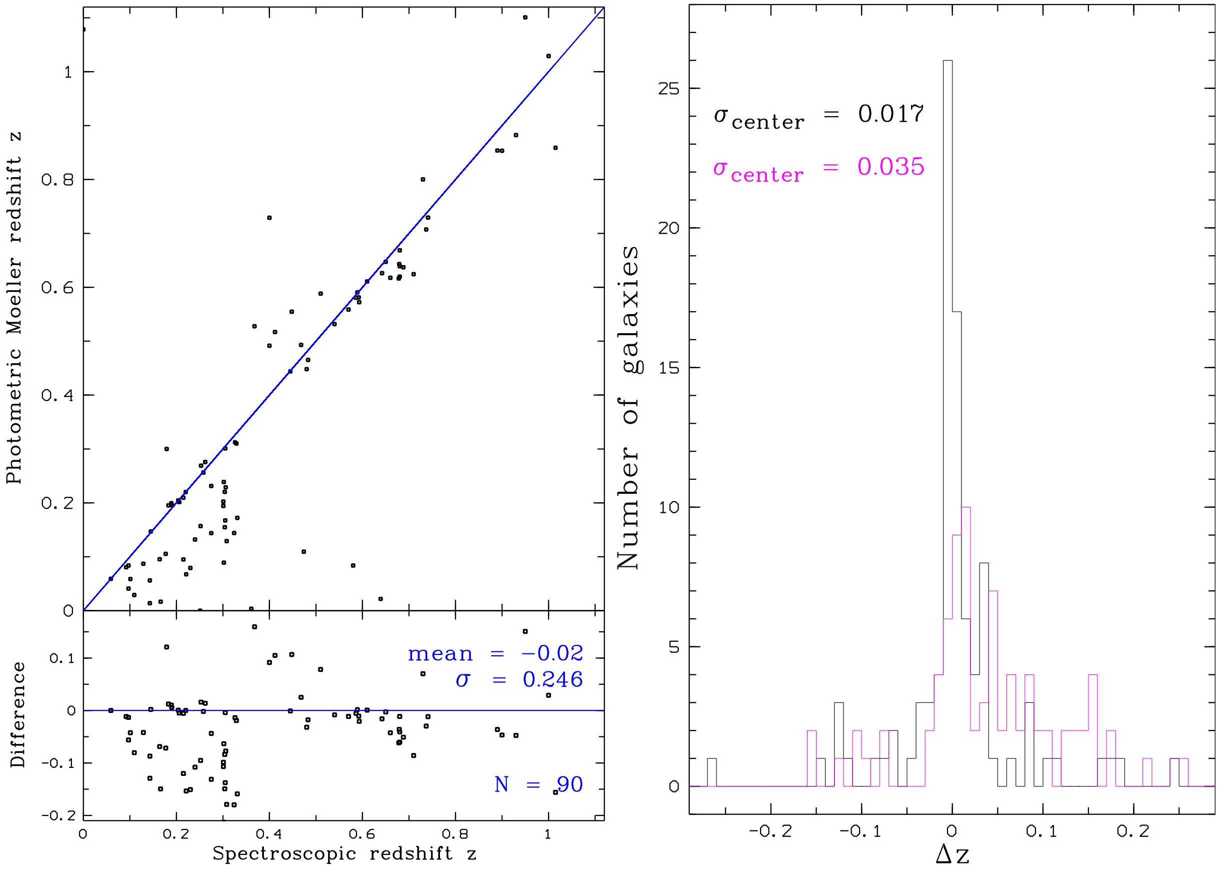

Figure 5.3: a) [left] Accuracy of redshift classification with C. S. Möller templates compared with spectroscopically measured redshifts
b) [right] Histogram over the redshift difference: black classification with Kinney spectra and red classification with C. S. Möller spectra

confidence level – except at low redshifts ($z < 0.3$). Not only do the faint objects differ, but also the bright (magenta) objects are classified differently. This can be due to the fact that at lower redshifts the flux of the galaxy edges are not measured (fixed aperture).
To compare the SED derived by the classification the SED of the library by C. S. Möller has been multiplied with a factor of 10 to obtain an SED classification from 0 to 100 like the one of the CADIS multi-color classification. We can see some shifts, but still a strong correlation (figure 5.4b). A direct dependency was not expected, due to different sets of template spectra in the SED dimension.
In contrast to the classification using Kinney spectra at the margins (SED = 0 and 100) of the template library, spectra of Möller show a better fit for small SEDs. A low density in the E population (SED < 10) is observable by using the Kinney library (figure 5.4b). When we classify with the Möller spectra there is no under–density at small SED. This is a feature in the classification and shows that the spectra can found in the data. This effect is most probably due to additional dimension of age in the template set.

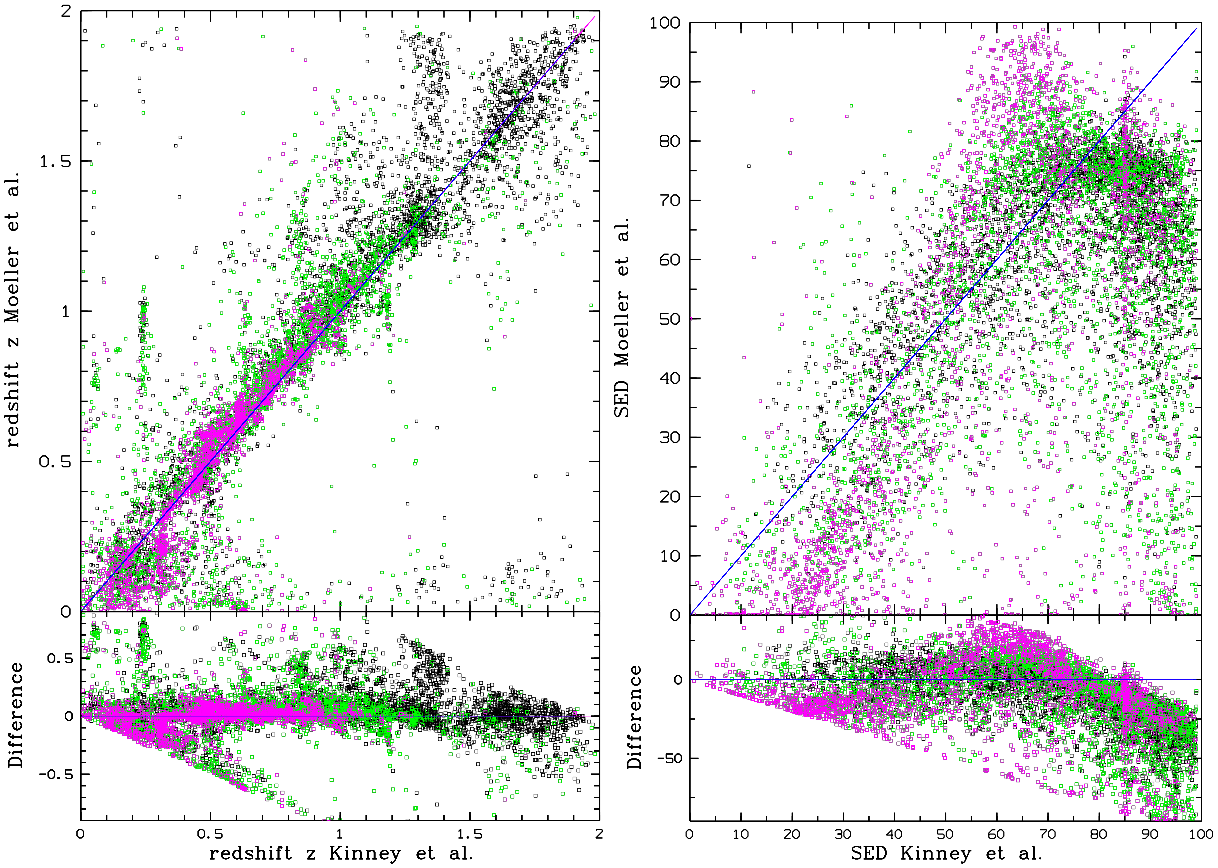

Figure 5.4: Comparison between classification with Kinney et al. templates and C. S. Möller et al. templates

Color coded brightness: **faint objects black $23^{\mathrm{m}} < \mathrm{m}_{\mathrm{B815}}$**; green $22^{\mathrm{m}} < \mathrm{m}_{\mathrm{B815}} < 23^{\mathrm{m}}$; bright objects magenta $\mathrm{m}_{\mathrm{B815}} < 22^{\mathrm{m}}$

a) [left] In redshift b) [right] In SED spectral energy distribution

A negative feature in the classification is the distribution of the starburst galaxies ($\mathrm{SED}_{\mathrm{Kinney}} > 60$). There is not only a shift between bright objects (red) and the faint populations (green and black), but also the high accumulation of objects between the spectra Sa and Sd (SED ≈ 75) of Möller SED dimension is still unexplained. A reason for this behavior might be that the template spectra are too similar because of a degeneracy of the age and SED. A few different classifications can be observed because of this additional dimension of age in the template set, but this cannot be the full reason for this large problem with starburst galaxy classification.

5.3 Time since last major star formation process

Nevertheless, in this classification with Möller et al. templates we gain a new dimension of information with this classification – the age of the galaxies. This age, or better time since the last major star formation process, is analyzed next in the CADIS galaxy sample.

In figure 5.5a the different ages of the galaxies are plotted for different epochs. We find that there is an inconsistency in the results. The whole top right corner of the diagram contains incorrect classified galaxies. For example, a galaxy at redshift one cannot have an age of 17 Gyears because it would have been formed before the Big Bang (compare figure 1.1). The maximum age at a redshift of one is about 5 Gyears (depending on the cosmology used).
We found that those objects are mainly starburst galaxies. When we exclude all the starburst galaxies – according to the Kinney classification SED > 60 – from the analysis, we obtain figure 5.5b, which is more realistic. According to the facts mentioned in the above section, it is not unexpected that we cannot use this classification for galaxy types later than Sc.

We conclude that the spectra of E\S0 and Sb by C. S. Möller et al. including aging processes are a good description of the observed population. The Sd spectrum cannot be fitted consistent to real objects and needs further investigation. A constant star formation rate does not describe sufficiently the observed spectra and probably a recent short starburst has to be added to the spectra.

For further interpretation we only use the early type galaxies E\S0 and Sb. We emphasize that the following interpretations are preliminary and further investigations are in progress.

According to the way the spectra are computed, the derived age has to be interpreted as the time when the last major star forming process took place in the galaxies. The reason for the starburst is not clear, but possible scenarios are major merger events or other processes triggering star formation.

With the given cosmology, we calculated at which redshift this process took place in every particular observed galaxy. Figure 5.6 shows how many galaxies had their major star forming process at a given redshift. For subsamples of every brightness limit the same trend can be observed. Even if we exclude the galaxies with a low classification confidence because of unknown classification features at $z < 0.3$, a peak remains around $z \approx 1.4$.

We conclude from figure 5.6 that there is a peak in star formation around $z = 1.4$, and we interpret this as a consistency with the peak in star formation in the Madau plot between redshift 1 and 2 (figure 1.3) [Madau et al., 1996]. However, a few remarks have to be made. First, in our analysis only early type galaxies are taken into account. Secondly, there is no normalization to a certain volume considered as in the Madau plots.
The starburst galaxies which are not analyzed above also have a peak in star formation between redshift of one and two [Blain, 2000, Madau et al., 1998]. Thus, this peak in star formation is present for all galaxies.

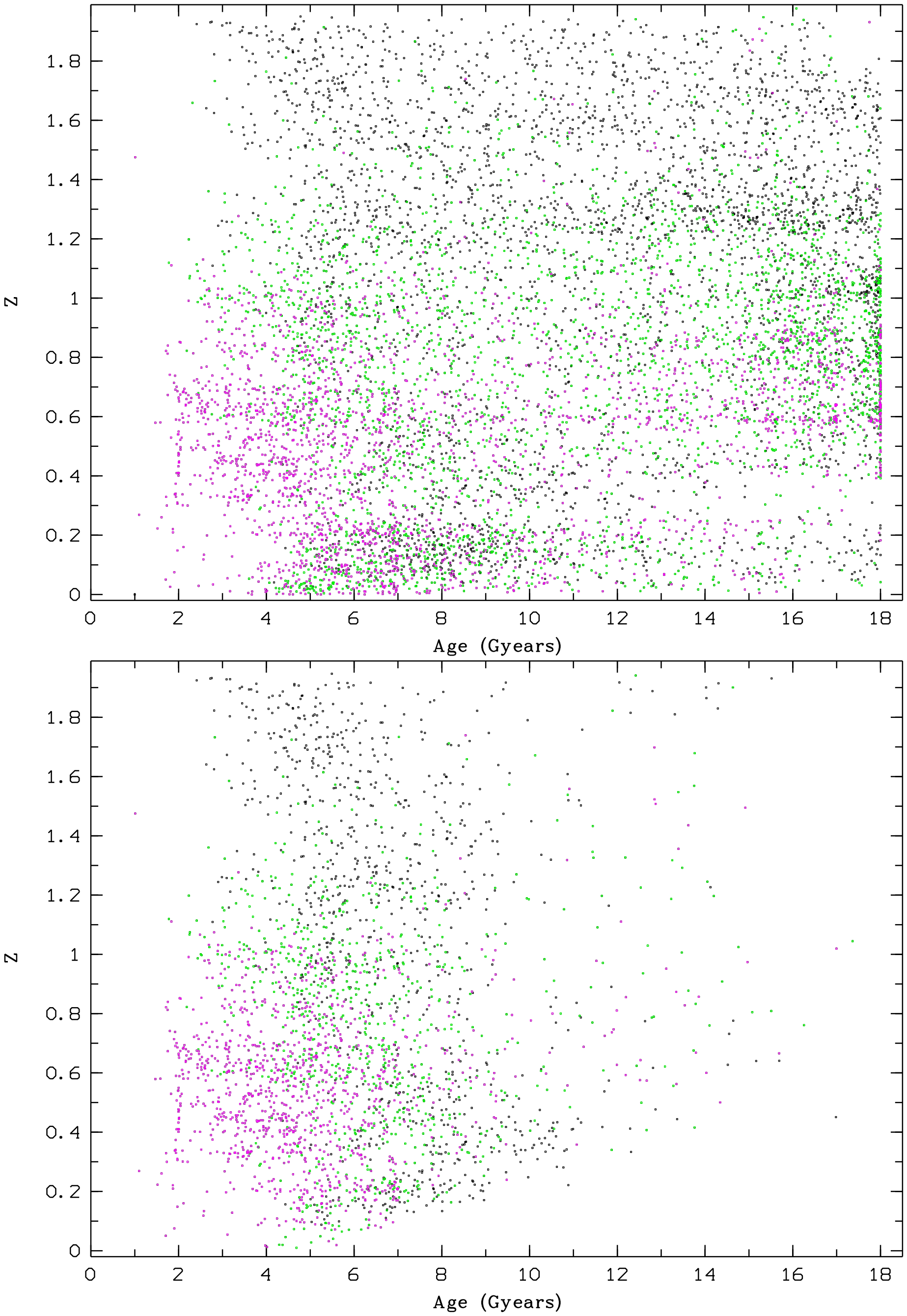

Figure 5.5: Age of the galaxies and its development during time (redshift z) color codes the brightness magenta $m_{B815} < 22^m$; green $22^m < m_{B815} < 23$; and **black** $23^m < \mathbf{m}_{B815}$
a) [top] All galaxies in the CADIS data sample
b) [bottom] Only E, S0, Sa, Sb and Sc galaxies of the CADIS data set (SED < 60) (starburst galaxies excluded)

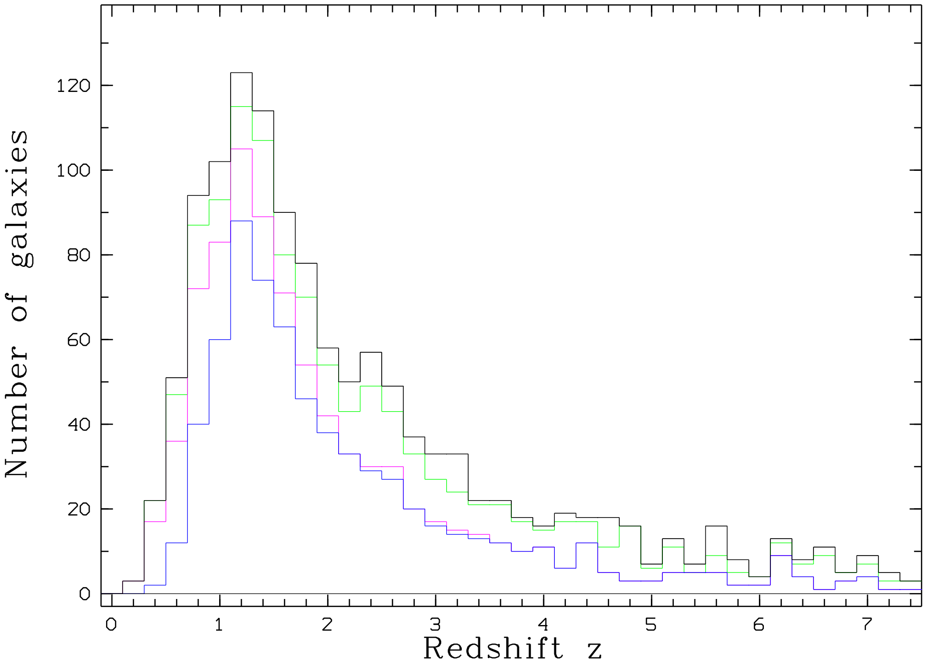

Figure 5.6: Histogram of last major burst of star formation at given redshift z; only E, S0, Sa, Sb and Sc galaxies
color code: **all galaxies black;** green $m_{B815} < 23^m$; magenta $m_{B815} < 22^m$; blue $m_{B815} < 22^m$ and securely classified with $z > 0.4$

The influence of the volume is much more difficult to estimate. It is obvious that at higher redshift larger volumes are covered by the observation (pencil beam effect). This should suppress wing of the peak at the higher redshifts side in figure 5.6.
More precisely, the observed volume in space where the galaxy is found (classified redshift) should be taken into account, which is different for each object with a major star burst in a certain redshift bin.

Thus, we interpret this as good evidence for a major star formation process in early type galaxies around a redshift of 1.4.

Chapter 6

Results and perspective

6.1 Results

This work describes the population of field galaxies at different epochs in a statistical way, and not the physical processes occurring in individual galaxies.

Using the CADIS data set of four analyzed fields, we examined the population of field galaxies at medium redshift and obtained the following results:

- We find a significant evolution for E–S0–Sa–Sb–Sc type galaxies by studying the luminosity function. The Schechter function parameter M^* shows a brightening of about 1.5^{m} from $z = 1.1$ to $z = 0.3$ for E–S0–Sa galaxies as well as for Sb–Sc galaxies. There is no evidence for an evolutionary change of M^* for starburst galaxies.

- The fraction of early type galaxies show a redshift dependent increase in the data set. Their fraction increases by a factor of 1.5 from redshift of 1.1 to a redshift of 0.3.

- Galaxies in the high redshift tend to be bluer in the B–V rest frame than in the local universe. This trend is most obvious for E–S0–Sa and starburst galaxies. Compared to Lilly [Lilly et al., 1998], who found this trend for starburst galaxies, we can confirm their result and expand their statement to early type galaxies (E–S0–Sa).

- We find that the semianalytical models of hierarchical galaxy formation of Mrs. Kauffmann et al. [Kauffmann and White, 1993] can reproduce the observed reddening of the galaxy population with time. However, they are not yet consistent with the properties and evolution of the field galaxy population. Many further iteration steps have to be performed to describe the observed medium redshift galaxy population with the simulations.

- We compared our measured galaxy spectra with the galaxy evolution model of C. S. Möller et al. [Möller et al., 2001]. From those models we derive for E–S0–Sa–Sb–Sc galaxies an estimation for the time at which the last major star forming epoch took place. We conclude that there was a major burst of star formation between redshift one and two.

In this thesis we find a change in the field galaxy population since $z = 2$. Between $1 < z < 2$ most of the early type galaxies underwent a large burst of star formation process probably due to merger events (E, S0, Sa, Sb, Sc). From z = 1 until today this population have brightened by a factor of 1.5 magnitudes and it have reddened.
With passive evolution those changes can not be explained, and thus passive evolution models are not longer tenable.

The large number of faint blue galaxies at medium redshift cannot be explained by this reddening effect alone. No change in the starburst galaxy luminosity function is observable at $0.3 < z < 1.1$. The fraction of low surface brightness galaxies in the galaxy population is still not exactly known and may influence our statements on galaxy population.

Valotto et al. [Valotto et al., 1997] found a cut–off at the bright end of $M^*= –20.0{\pm}0.1^{\mathrm{m}}$ in the luminosity function for galaxies in clusters for H_0 = 100 km/Mpc. In our cosmology this corresponds to $M^*= –21.5^{\mathrm{m}}$ which lies within the errors found in this work for the population of field galaxies up to a redshift of 0.75. Valotto et al. derived a faint end slope of $\alpha = -1.4 \pm 0.1$ from an analysis down to $M_{\mathrm{B815}} = -16^{\mathrm{m}}$. The only redshift bin in our data that reaches this limit is $0.1 < \mathrm{z} < 0.3$ where we also find a slope of $\alpha = -1.36 \pm 0.12$. This is the same within the errors, but our result is a lower limit because of remaining incompleteness.

We suggest that the faint end slope and the evolution found by other analysis is mainly due to incompleteness and selection effects. No differences in α can yet be found for field and cluster galaxy populations at different redshifts.

6.2 Perspective

The large CADIS data set offers many possibilities to study galaxy evolution. With the completion of all eight fields a data set will be collected, which allows to study smaller subsamples of galaxy types (SED) and of redshifts. New questions such as the influence of different cosmological models may be addressed. Additional questions may arise, when the multi–color classification is tested beyond z =1.1, and the luminosity function analysis can be extended to higher redshifts. Since the faint end of the luminosity function is dominated by emission line galaxies [Lin et al., 1996, Zucca et al., 1997], CADIS provides a unique possibility to determine the faint end slope (α) in the Schechter function, by using the emission line galaxies found in CADIS which have a fainter observational limit than the multi–color classified galaxies. Comoving density analysis and statements for different cosmological models can be addressed.

A further comparison of theoretical models with the CADIS data set will also be interesting. This can give further tuning for the simulation parameters and result in better agreement with the models, with the goal to derive more reliable conclusions about galaxy evolution at higher redshifts.

Upcoming large surveys as the SDSS[1] survey and COMBO–17[2] will provide immense data sets to investigate and quantify redshift trends. Such observations will further increase mankind's knowledge about the evolution of the universe.

---

[1] **S**loan **D**igital **S**ky **S**urvey (**SDSS**)

[2] **C**lassifying **O**bjects by **M**edium–**B**and **O**bservations in **17** filters: a spectrophotometric 17– filter survey (**COMBO 17**)

Appendix A

C-source-code

```
/*****************************************************************
 *                                                               *
 * NAME:    fit_lf_sty.c                                         *
 *                                                               *
 * VERSION: 1.0     first steps        BvK  DATE:   19.  May 1999   *
 *          2.0     reactivated        BvK          22.  Jun 2001   *
 *          2.1     limits incorporated             o8.  Oct 2001   *
 *                                                               *
 * AUTHOR:  BvK [Bernd von Kuhlmann], MPIA, Heidelberg           *
 *                                                               *
 * PURPOSE: Program to perform maximum likelihood fit for        *
 *           luminosity function in form of Schechter function   *
 *                                                               *
 *****************************************************************/

#include <stdio.h>      /* input output functions */
#include <math.h>       /* mathematical functions (log, foor...)  */
#include <midas_def.h>  /* Midas comunicationfunctions (optional) */

/* ******* Define Functions!  Code see at the end ********* */

#define FUNCTION schechter
   void schechter (float*, int, float*, float*);

int main(void)

{

/* ******* definitions ******* */

    /* help and loop variables */
    int    a, b;
    int    helpi = 0, helpi2 = 0;
    float  helpreal;
```

```
/* output variable:  1 = output yes; = 0 no output */
int    output = 0;

/* number of datapoints/objects */
int    ndata;

/* input data */
double input_abs_mag_b[ndata],     /* absolute magnitude */
       input_z[ndata],             /* redshift */
       input_limit[ndata],         /* limiting absolute
                                      magnitude */
       input_mag_i[ndata],         /* apparent in B815/I */
       input_sed[ndata];           /* SED */

/* dimension and steps for completeness array */
int   size_ref, number_z, number_mag, number_sed;
int   index[3];
float start_z, step_z, start_mag, step_mag, start_sed, step_sed;
float ref_array [number_z][number_mag][number_sed];

/* variables for the numerical integrals */
int    integ_steps = 200;
float  integ_min, integ_max, integ_width, integ;
float  integ_array_in[integ_steps], integ_array_out[integ_steps];

/* variables for the output array (only 2 dimensions used) */
int     size_out, npixel_out[3], dimensions = 2;
double  start_out[3], step_out[3];

double results [npixel_out[0]] [npixel_out[1]];
               /* dimension 0 <=> M* ;  dimension 1 <=> alpha */

/* variables for the likelihood loop */
int    runalpha, runmstar, objectnr;
float  alpha, mstar;
float  probobject, parafunction[3];

double likelihood;

/* variables to store the maximum */
int    max_pixel[3];
float  max_mstar = -1e38, max_alpha = -1e38, max_phy = -1e38;
float  maxlh = -1e38;

/* variables for phy star normalisation */
int objectcounts[5] = {0,0,0,0,0};
float  min_z_in, max_z_in, min_abs_mag, runr;
float  cuts_out[6]  = { -0.1, 0.0, 0.0, 0.0, 0.0, 0.0 };
float  intlimit[5]  = {0.0,0.0,0.0,0.0,0.0};
float  integnorm[5] = {0.0,0.0,0.0,0.0,0.0};
```

```
/* ******* INPUT routines for midas or ASCII tables

           SIMPLE AND THUS NOT DESCRIBED here ******* /

/* ************************************************************ */
/* ******* MAIN PROGRAM for STY fit (schechter) function ******* */

   alpha = start_out[1]-step_out[1];  /*start value for loop */
                   /* work along all possible(input) values of the
                      function runalpha; runmstar loop-index values
                      (integer)
                      alpha and mstar real-loop values (real) */
                   /* dimension 0 <=> M* ;  dimension 1 <=> alpha */

  for (runalpha=0; runalpha<npixel_out[1]; runalpha++)
    {              /* loop along dimension 1 = alpha */
    alpha = alpha + step_out[1];
    mstar = start_out[0]-step_out[0];

    for (runmstar=0; runmstar<npixel_out[0]; runmstar++)
      {            /* loop along dimension 0 = mstar */
      mstar = mstar + step_out[0];
      printf("\r * fit_lf_sty.c working on alpha:  = %6.3f (%3d/%3d) \
                        \tM* = %6.3f (%3d/%3d)\twith %4d objects *",
              alpha,runalpha,npixel_out[1],
              mstar,runmstar,npixel_out[0],ndata);

                   /* set schechter function parameter */
      parafunction[0] = 1.0;
      parafunction[1] = mstar;
      parafunction[2] = alpha;
                   /* initiales L */
      likelihood = 0.0;

      /* ****** now compute likelihood for
                current value of alpha and mstar ****** */
      for (objectnr = 0; objectnr < ndata; objectnr++)
        {          /* loop along all objects */

                   /* compute value of the (schechter) function
                      and divide by normalisation integral */

        probobject = 0.0;
```

```
helpreal = input_abs_mag_b[objectnr];
schechter (&helpreal,1,parafunction,&probobject);

if (output)
   printf("\n M_abs= %7.3e PHY=  %7.3e (%7.3e )",
   input_abs_mag_b[objectnr],probobject,log(probobject));

/* *** Integral (numerical) over the (Schechter) function
       from -oo till magnitude limit of the object *** */

           /* upper integration limit = minimal observed
              magnitude in the dataset */
integ_max  = - 8.0;

           /* lower integration limit = maximal observed
              magnitude in the dataset */
integ_min  = - 28.0;


           /* steps are set to (integ_steps)
              1000 numerical steps */
integ = 0.0;
integ_width = (integ_max-integ_min)/(integ_steps-1.0);
           /* fill input array */
for (a = 0; a < integ_steps; a++)
   integ_array_in[a] = integ_min + a * integ_width;
           /* compute function */
schechter (integ_array_in,integ_steps,parafunction,
           integ_array_out);
           /* sum up until integration limit */
for (a = 0; a < integ_steps; a++)
    {
    if ( integ_array_in[a] < input_limit[objectnr])
       integ = integ + integ_array_out[a]*integ_width;
    }

probobject = (float) (log((double)probobject) - log((double)integ));

/* *** find cell in completeness table *** */
           /* z start step npix; mag  start step npix;
              sed  start step npix; */
index[0] = (int) floor( (input_z[objectnr]     - start_z  ) / step_z );
index[1] = (int) floor( (input_mag_i[objectnr] - start_mag) / step_mag );
```

```
  index[2] = (int) floor( (input_sed[objectnr]   - start_sed) / step_sed );

             /* if not represented in completeness array
                 use completeness one */
  if      (index[0] < 0 || index[0] > number_z  )
    { if ( runalpha == 0 && runmstar == 0 )
       printf ("\n*** WARNING ! - fit_lf_sty.c - Object %5d   \
                  z outside COMP-table - use one!  ***",
              objectnr);}
  else if (index[1] < 0 || index[1] > number_mag)
    {if ( runalpha == 0 && runmstar == 0 )
       printf ("\n*** WARNING ! - fit_lf_sty.c - Object %5d   \
                  mag outside COMP-table - use one!  ***",
              objectnr);}
  else if (index[2] < 0 || index[2] > number_sed)
    { if ( runalpha == 0 && runmstar == 0 )
       printf ("\n*** WARNING ! - fit_lf_sty.c - Object %5d   \
                  sed outside COMP-table - use one!  ***",
              objectnr);}
  else
    {
     probobject = probobject / ref_array[index[0]][index[1]][index[2]];
    }

             /* add this object to the likelihood */
  likelihood = likelihood + (double) probobject;
  }          /* end loop objects */

             /* save likelihood in result array */
results [runmstar][runalpha] = likelihood;


/*  *** check if new maximum is reached *** */

if  (likelihood > maxlh)
  {
  maxlh = likelihood;
  max_mstar    = mstar;
  max_alpha    = alpha;
  max_pixel[0] = runmstar;
  max_pixel[1] = runalpha;
  }
```

```
      }            /* end loop mstar */

    }              /* end loop alpha */
  printf
("\r                                                                                                    \

                   /* output loop for result array (0,0 bottom left)*/
  if (output)
    {
    printf ("\n\n");
    for (b =  npixel_out[1]-1; b >= 0; b--)
      {            /* loop along rows   / dim1 / Y */
      for (a = 0; a <= npixel_out[0]-1; a++)
        {          /* loop along column / dim0 / X */
        printf (" %6.2e ",  results[a][b]);
        }
      printf ("\n");
      }
      printf ("\n\n");
      }

  /* ***** normalisation of phy star:
           integral over observed counts ***** */

  /* *** compute numerical integral *** */
  max_phy = 1.0;
  integ_min  = -28.0;
  integ_max  = -8.0;
  integ = 0.0;
  integ_width = (integ_max-integ_min)/(integ_steps-1.0);
                    /* fill input values for integral */
  for (a = 0; a < integ_steps; a++)
       integ_array_in[a] = integ_min + a * integ_width;
  parafunction[0] = max_phy;
  parafunction[1] = max_mstar;
  parafunction[2] = max_alpha;
                   /* compute values for the integral */
  schechter (integ_array_in,integ_steps,parafunction,
             integ_array_out);
                   /* sum up integral */
  for (runr = min_z_in; runr <= max_z_in; runr = runr + 0.01)
    {              /* compute integral in redshift steps of 0.01 */
    helpreal = 0.0;
```

```
  helpi    = 0;
                 /* find average luminosity limit in the data
                    of that redshift bin */
  for (objectnr = 0; objectnr < ndata; objectnr++)
    {            /* loop along the objects */
      if ( input_z[objectnr] < runr+0.02 &&
           input_z[objectnr] > runr-0.02)
        {
        helpreal = helpreal + input_limit[objectnr];
        helpi++;
        }
      intlimit[2] = helpreal/helpi;
    }

                 /* now integration of the (Schechter) function */
  for (helpi2 = 0; helpi2 < integ_steps; helpi2++)
    {
    if ( integ_array_in[helpi2] > min_abs_mag &&
         integ_array_in[helpi2] < intlimit[2])
       integnorm[2] = integnorm[2] + integ_array_out[helpi2]*integ_width;
    }

                 /* now counting number of objects in the sample */
  for (objectnr = 0; objectnr < ndata; objectnr++)
    {
    if ( input_z[objectnr] <  runr+0.005 &&
         input_z[objectnr] > runr-0.005)
      {
      if ( input_abs_mag_b[objectnr] < intlimit[2] )
         objectcounts[2]++;
      }
    }
  }              /* end loop zvalues */

                 /* compute phy max value */
  max_phy = objectcounts[2] / integnorm[2];

                 /* compute  L - Lmax ( to be correct it has to be
                    Lmax - L, but that is not nice to plot!  )  */

likelihood =  results [max_pixel[0]][ max_pixel[1]];

/* *** write out result array *** */
```

```
  if (output)
     {
     for (b = npixel_out[1]-1; b >= 0; b--)
                  /* loop along rows  / dim1 / Y */
         for (a = 0; a <= npixel_out[0]-1; a++)
         {        /* loop along columns / dim0 / X */
         results[a][b] = (results[a][b]) - (likelihood) ;

                  /* store maximum for plots later */
         if (results[a][b] > cuts_out[1])
             cuts_out[1] = results[a][b];
         else if (results[a][b] < cuts_out[0])
             cuts_out[0] = results[a][b];
         }
     }

    printf("\n ====== Result of fit_lf_sty.c(BvK) of %d           \
                  Objects  ======", ndata);
    printf("\n        PHY* (MAX)= %7.3f \tM* (max)= %7.3f         \
                  \t alpha (max) = %7.3f \n",
                  max_phy, max_mstar, max_alpha) ;

/* ******* save results
           for example in Midas frames, keywords
           and descriptors

           SIMPLE AND THUS NOT DESCRIBED HERE ....   ******* */

}                 /* end main */

/* ******* Functions:   ******* */

void schechter(float* x, int s_size, float* s_para, float* y)
                  /* for computing Schechterfunction values
                     of single values and arrays */
                  /* Parameter:  input values for magnitudes
                                (pointer to array),
                               sizes of the array,
                               Schechterfunction parameter array
                               (Phy,Mstar,alpha),
                               output array (pointer) */
{
   float zehn,fac,expo,schech;
```

```
   int s_run;

   for (s_run = 0; s_run < s_size; s_run++)
      {            /* poop over input value array */
      zehn     = pow(10,(2.0/5.0*(s_para[1]-x[s_run])));
      fac      = 2.0/5.0*s_para[0]*log(10);
      expo     = exp(-1*zehn);
      schech   = fac*pow(zehn,(1+s_para[2]))*expo;
      y[s_run] = schech;
      }
}
```

List of Figures

List of Tables

Bibliography

[Barrow et al., 1984] Barrow, J. D., Sonoda, D. H., and Bhavsar, S. P. (1984). A bootstrap resampling analysis of galaxy clustering. *Monthly Notices of the Royal Astronomical Society*, 210:19P–23P. 47

[Beckwith et al., 1998] Beckwith, S., Chaffee, F., , Fried, J. W., Hippelein, H. H., Huang, J., von Kuhlmann, B., Leinert, C., Meisenheimer, K., Phleps, S., Röser, H.-J., Thiering, I., Thommes, E., Thompson, D. J., and Wolf, C. (1998). Calar Alto Deep Imaging Survey – CADIS – revised proposal. hhttp://www.mpia-hd.mpg.de/GALAXIES/CADIS/cadis_prop_aug98.ps.gz. 7, 13

[Bertin and Arnouts, 1996] Bertin, E. and Arnouts, S. (1996). SExtractor: Software for source extraction. *Astronomy and Astrophysics Supplement Series*, 117:393–404. 12, 16

[Binggeli et al., 1988] Binggeli, B., Sandage, A., and Tammann, G. A. (1988). The luminosity function of galaxies. *Annual Review of Astronomy and Astrophysics*, 26:509–560. 41, 43, 59, 61, 64, 112

[Blain, 2000] Blain, A. (2000). The history of starburst galaxies. astro-ph/0011387. 4, 93

[Bower, 1991] Bower, R. G. (1991). The evolution of groups of galaxies in the Press-Schechter formalism. *Monthly Notices of the Royal Astronomical Society*, 248:332–352. 75

[Bruzual A. and Charlot, 1993] Bruzual A., G. and Charlot, S. (1993). Spectral evolution of stellar populations using isochrone synthesis. *Astrophysical Journal*, 405:538–553. 13

[Carlberg et al., 2000] Carlberg, R. G., Yee, H. K. C., Morris, S. L., Lin, H., Hall, P. B., Patton, D., Sawicki, M., and Shepherd, C. W. (2000). Galaxy Clustering Evolution in the CNOC2 High-Luminosity Sample. *Astrophysical Journal*, 542:57–67. 37, 39

[Chaisson and Mc Millan, 1993] Chaisson, E. and Mc Millan, S. (1993). *Astronomy today*. Prentice-Hall Incorporated, 2. edition. 3

[Coleman et al., 1980] Coleman, G. D., Wu, C. ., and Weedman, D. W. (1980). Colors and magnitudes predicted for high redshift galaxies. *Astrophysical Journal Supplement Series*, 43:393–416. 76

[Dressler, 1980] Dressler, A. (1980). Galaxy morphology in rich clusters - Implications for the formation and evolution of galaxies. *Astrophysical Journal*, 236:351–365. 41

[Efstathiou et al., 1988] Efstathiou, G., Ellis, R. S., and Peterson, B. A. (1988). Analysis of a complete galaxy redshift survey. II - The field-galaxy luminosity function. *Monthly Notices of the Royal Astronomical Society*, 232:431–461. 41, 43, 44, 64

[Ellis, 1997] Ellis, R. S. (1997). Faint Blue Galaxies. *Annual Review of Astronomy and Astrophysics*, 35:389–443. 3

[Ellis, 2001] Ellis, R. S. (2001). Galaxy formation and evolution: recent progress. astro-ph/102056. 1, 4

[Ellis et al., 1996] Ellis, R. S., Colless, M., Broadhurst, T., Heyl, J., and Glazebrook, K. (1996). Autofib Redshift Survey - I. Evolution of the galaxy luminosity function. *Monthly Notices of the Royal Astronomical Society*, 280:235–251. 4, 39, 42, 43, 65

[Fan et al., 2001] Fan, X., L., P., and H.W., R. (2001). Jüngster Quasar durchleuchtet Urmaterie des Universums. http://www.mpg.de/pri01/pri0152.htm. 1

[Felten, 1976] Felten, J. E. (1976). On Schmidt's Vm estimator and other estimators of luminosity functions. *Astrophysical Journal*, 207:700–709. 42

[Felten, 1977] Felten, J. E. (1977). Study of the luminosity function for field galaxies. *Astronomical Journal*, 82:861–878. 41, 43

[Ferguson and McGaugh, 1995] Ferguson, H. C. and McGaugh, S. S. (1995). The Contribution of Low Surface Brightness Galaxies to Faint Galaxy Counts. *Astrophysical Journal*, 440:470. 64

[Fockenbrock, 1998] Fockenbrock, R. (1998). *Verteilung, Leuchtkraftfunktion und Statistik von Emissionsline-Galaxien bei 0.3 $<$ z $<$ 1.2*. PhD thesis, Ruprechts–Karls–Universität Heidelberg. 9

[Fried et al., 2001] Fried, J. W., von Kuhlmann, B., Meisenheimer, K., Rix, H. W., Wolf, C., Hippelein, H. H., Kümmel, M., Phleps, S., Röser, H.-J., Thierring, I., and Maier, C. (2001). The luminosity function of field galaxies and its evolution since z=1. *Astronomy and Astrophysics*, 367:788–800. 9, 27, 44, 50, 65

[Fruchter, 2001] Fruchter, A. (2001). Galaxy at redshift 5.58,the most distant galaxy yet measured. http://antwrp.gsfc.nasa.gov/apod/ap011007.html. 1

[Glänzer, 1994] Glänzer, H. (1994). Test und Kalibration eines Fokalreduktor–Spektrographen. Master's thesis, Max–Planck–Institut für Astronomie in Heidelberg. 10

[Gunn and Stryker, 1983] Gunn, J. E. and Stryker, L. (1983). *Stellar spectrometric atlas 3130 A - 10800 A*. NSSDC / WDC-A-R&S, Greenbelt: NASA, National Space Science Data Center (NSSDC), 1983. 13

[Hippelein, 2002] Hippelein, H. (2002). Star formation rates between $z = 0.25$ and $z = 1.2$ from CADIS emission line survey. in preperation. 9

[Kauffmann et al., 1996] Kauffmann, G., Charlot, S., and White, S. D. M. (1996). Detection of strong evolution in the population of early-type galaxies. *Monthly Notices of the Royal Astronomical Society*, 283:L117–L122. 64

[Kauffmann and White, 1993] Kauffmann, G. and White, S. D. M. (1993). The merging history of dark matter haloes in a hierarchical universe. *Monthly Notices of the Royal Astronomical Society*, 261:921–928. 75, 76, 97

[Kauffmann et al., 1993] Kauffmann, G., White, S. D. M., and Guiderdoni, B. (1993). The Formation and Evolution of Galaxies Within Merging Dark Matter Haloes. *Monthly Notices of the Royal Astronomical Society*, 264:201. 75, 76, 79

[Kayser et al., 1997] Kayser, R., Helbig, P., and Schramm, T. (1997). A general and practical method for calculating cosmological distances. *Astronomy and Astrophysics*, 318:680–686. 21, 89

[Kinney et al., 1996] Kinney, A. L., Calzetti, D., Bohlin, R. C., McQuade, K., Storchi-Bergmann, T., and Schmitt, H. R. (1996). Template Ultraviolet to Near-Infrared Spectra of Star-forming Galaxies and Their Application to K-Corrections. *Astrophysical Journal*, 467:38. 13, 14, 82, 87, 89

[Koo and Kron, 1992] Koo, D. C. and Kron, R. G. (1992). Evidence for evolution in faint field galaxy samples. *Annual Review of Astronomy and Astrophysics*, 30:613–652. 41

[Le Fèvre et al., 2000] Le Fèvre, O., Abraham, R., Lilly, S. J., Ellis, R. S., Brinchmann, J., Schade, D., Tresse, L., Colless, M., Crampton, D., Glazebrook, K., Hammer, F., and Broadhurst, T. (2000). Hubble Space Telescope imaging of the CFRS and LDSS redshift surveys - IV. Influence of mergers in the evolution of faint field galaxies from z˜1. *Monthly Notices of the Royal Astronomical Society*, 311:565–575. 64

[Lilly et al., 1998] Lilly, S., Schade, D., Ellis, R., Le Fevre, O., Brinchmann, J., Tresse, L., Abraham, R., Hammer, F., Crampton, D., Colless, M., Glazebrook, K., Mallen-Ornelas, G., and Broadhurst, T. (1998). Hubble Space Telescope Imaging of the CFRS and LDSS Redshift Surveys. II. Structural Parameters and the Evolution of Disk Galaxies to Z approximately 1. *Astrophysical Journal*, 500:75. 73, 97

[Lilly et al., 1995] Lilly, S. J., Tresse, L., Hammer, F., Crampton, D., and Le Fevre, O. (1995). The Canada-France Redshift Survey. VI. Evolution of the Galaxy Luminosity Function to Z approximately 1. *Astrophysical Journal*, 455:108. 4, 39, 50, 64

[Lin et al., 1996] Lin, H., Kirshner, R. P., Shectman, S. A., Landy, S. D., Oemler, A., Tucker, D. L., and Schechter, P. L. (1996). The Luminosity Function of Galaxies in the Las Campanas Redshift Survey. *Astrophysical Journal*, 464:60. 44, 77, 98

[Lin et al., 1999] Lin, H., Yee, H. K. C., Carlberg, R. G., Morris, S. L., Sawicki, M., Patton, D. R., Wirth, G., and Shepherd, C. W. (1999). The CNOC2 Field Galaxy Luminosity Function. I. A Description of Luminosity Function Evolution. *Astrophysical Journal*, 518:533–561. 4, 37, 43, 50, 64

[Madau et al., 1996] Madau, P., Ferguson, H. C., Dickinson, M. E., Giavalisco, M., Steidel, C. C., and Fruchter, A. (1996). High-redshift galaxies in the Hubble Deep Field: colour selection and star formation history to z˜4. *Monthly Notices of the Royal Astronomical Society*, 283:1388–1404. 4, 93

[Madau et al., 1998] Madau, P., Pozzetti, L., and Dickinson, M. (1998). The Star Formation History of Field Galaxies. *Astrophysical Journal*, 498:106. V, 4, 93

[Marinoni et al., 1999] Marinoni, C., Monaco, P., Giuricin, G., and Costantini, B. (1999). The Nearby Optical Galaxy Sample: The Local Galaxy Luminosity Function. *Astrophysical Journal*, 521:50–63. 41, 59

[Marzke et al., 1994] Marzke, R. O., Geller, M. J., Huchra, J. P., and Corwin, H. G. (1994). The luminosity function for different morphological types in the CfA Redshift Survey. *Astronomical Journal*, 108:437–445. 44

[Meisenheimer, K., 2002] Meisenheimer, K. (2002). The Calar Alto Deep Imaging Suvey: Concept, Data Analythis and Calibration. in preparation. 13

[Meisenheimer, 1994] Meisenheimer, K. (1994). Cafos 2,2 – Der Fokalreduktor des 2.2–m–Teleskops auf dem Calar–Alto. *Sterne und Weltraum*, 7:516–522. 10

[Meisenheimer et al., 1998] Meisenheimer, K., Beckwith, S., Fockenbrock, R., Fried, J., Hippelei, H., Huang, J., Leinert, C., Phleps, S., Röser, H., Thompson, D., Wolf, C., and Chaffee, F. (1998). The Calar Alto Deep Imaging Suvey for Galaxies and Quazars at $z > 5$. In D'Odorico, I., Fortuna, S., and Giallongo, E., editors, *The Young Universe*, page 134. 7

[Meisenheimer et al., 2001] Meisenheimer, K., Drepper, S., Fried, J. W., Hippelein, H. H., Kümmel, M., von Kuhlmann, B., Maier, C., Phleps, S., Röser, H.-J., Rix, H., and Wolf, C. (2001). CADIS Webpage. http://www.mpia-hd.mpg.de/GALAXIES/CADIS/science_index.html. 13

[Möller et al., 2001] Möller, C. S., Fritze-V. Alvensleben, U., Fricke, K. J., and Calzetti, D. (2001). Chemically Consistent Evolutionary Models With Dust. *Astrophysics and Space Science*, 276:799–806. 87, 89, 97

[Nonino et al., 1999] Nonino, M., Bertin, E., da Costa, L., Deul, E., Erben, T., Olsen, L., Prandoni, I., Scodeggio, M., Wicenec, A., Wichmann, R., Benoist, C., Freudling, W., Guarnieri, M. D., Hook, I., Hook, R., Mendez, R., Savaglio, S., Silva, D., and Slijkhuis, R. (1999). ESO Imaging Survey. I. Description of the survey, data reduction and reliability of the data. *Astronomy and Astrophysics Supplement Series*, 137:51–74. 27

[Oke, 1990] Oke, J. B. (1990). Faint spectrophotometric standard stars. *Astronomical Journal*, 99:1621–1631. 12

[Phleps, 1998] Phleps, S. (1998). Schwache Sterne in CADIS und die Struktur der Milchstraße. Master's thesis, Ruprechts–Karls–Universität Heidelberg. 9

[Phleps et al., 2000] Phleps, S., Meisenheimer, K., Fuchs, B., and Wolf, C. (2000). CADIS deep star counts: Galactic structure and the stellar luminosity function. *Astronomy and Astrophysics*, 356:108–117. 9

[Press et al., 1994] Press, W., Teukolsky, S., Vetterling, W., and Flannery, B. (1994). *Numerical Recipies in C*. Cambridge University Press. 43, 45

[Press and Schechter, 1974] Press, W. H. and Schechter, P. (1974). Formation of Galaxies and Clusters of Galaxies by Self-Similar Gravitational Condensation. *Astrophysical Journal*, 187:425–438. 75

[Rocca-Volmerange and Guiderdoni, 1988] Rocca-Volmerange, B. and Guiderdoni, B. (1988). An atlas of synthetic spectra of galaxies. *Astronomy and Astrophysics Supplement Series*, 75:93–106. 76

[Röser and Meisenheimer, 1986] Röser, H.-J. and Meisenheimer, K. (1986). CCD photopolarimetry of the jet of 3 C 273. *Astronomy and Astrophysics*, 154:15–24. 12

[Röser and Meisenheimer, 1991] Röser, H.-J. and Meisenheimer, K. (1991). The synchrotron light from the jet of 3C 273. *Astronomy and Astrophysics*, 252:458–474. 12

[Sandage et al., 1985] Sandage, A., Binggeli, B., and Tammann, G. A. (1985). Studies of the Virgo cluster. IV - an Atlas of Virgo cluster spiral galaxies: The luminosity range within a given spiral type. *Astronomical Journal*, 90:395–404. 41

[Sandage et al., 1979] Sandage, A., Tammann, G. A., and Yahil, A. (1979). The velocity field of bright nearby galaxies. I - The variation of mean absolute magnitude with redshift for galaxies in a magnitude-limited sample. *Astrophysical Journal*, 232:352–364. 44

[Schade et al., 1999] Schade, D., Lilly, S. J., Crampton, D., Ellis, R. S., Le Fèvre, O., Hammer, F. ., Brinchmann, J., Abraham, R., Colless, M., Glazebrook, K., Tresse, L., and Broadhurst, T. (1999). Hubble Space Telescope Imaging of the CFRS and LDSS Redshift Surveys. III. Field Elliptical Galaxies at 0.2<z<1.0. *Astrophysical Journal*, 525:31–46. 64

[Schechter, 1976] Schechter, P. (1976). An analytic expression for the luminosity function for galaxies. *Astrophysical Journal*, 203:297–306. 43

[Schmidt, 1968] Schmidt, M. (1968). Space Distribution and Luminosity Functions of Quasi-Stellar Radio Sources. *Astrophysical Journal*, 151:393. 42

[Subbarao et al., 1996] Subbarao, M. U., Connolly, A. J., Szalay, A. S., and Koo, D. C. (1996). Luminosity Functions From Photometric Redshifts. I. Techniques. *Astronomical Journal*, 112:929. 41

[Tammann et al., 1979] Tammann, G. A., Yahil, A., and Sandage, A. (1979). The velocity field of bright nearby galaxies. II - Luminosity functions for various Hubble types and luminosity classes - The peculiar motion of the local group relative to the Virgo cluster. *Astrophysical Journal*, 234:775–784. 44

[Thommes, 1996] Thommes, E. (1996). *Suche nach Lyman–α Emissions von Urgalaxien bei $z > 5$.* PhD thesis, Ruprechts–Karls–Universität Heidelberg. 7

[Thompson et al., 1999] Thompson, D., Beckwith, S. V. W., Fockenbrock, R., Fried, J., Hippelein, H., Huang, J. ., von Kuhlmann, B., Leinert, C., Meisenheimer, K., Phleps, S., Röser, H. ., Thommes, E., and Wolf, C. (1999). The Surface Density of Extremely Red Objects. *Astrophysical Journal*, 523:100–106. 9

[Totani and Yoshii, 1998] Totani, T. and Yoshii, Y. (1998). Does the Number Density of Elliptical Galaxies Change at z<1? *Astrophysical Journal Letters*, 501:L177. 4

[Valotto et al., 1997] Valotto, C. A., Nicotra, M. A., Muriel, H., and Lambas, D. G. (1997). The Luminosity Function of Galaxies in Clusters. *Astrophysical Journal*, 479:90. 41, 98

[von Kuhlmann, 1997] von Kuhlmann, B. (1997). Inbetriebnahme und Leistungstest des Fokalreduktors MOSCA für das 3,5-Meter-Teleskop auf dem Calar Alto. Master's thesis, Ruprecht-Karls-Universität Heidelberg, Max-Planck-Insitiut für Astronomie. 10

[von Kuhlmann and Fried, 1999] von Kuhlmann, B. and Fried, J. (1999). Luminosity function of field-galaxies between Z = 0.2 and 1. In Schielick, R., editor, *Abstracts of Contributed Talks and Posters presented at the Annual Scientific Meeting of the Astronomische Gesellschaft, in Goettingen*, volume 15, page 94. Astronomische Gesellschaft, Colordruck Kurt Weber GmbH, D–Leimen, Germany. 9

[Walsh, 1995] Walsh, J. (1995). Optical and UV spectroscopic standard stars. http://www.eso.org/observing/standards/spectra/. 12

[Willmer, 1997] Willmer, C. N. A. (1997). Estimating galaxy luminosity functions. *Astronomical Journal*, 114:898–912. 41

[Wolf, 1999] Wolf, C. (1999). *Vielfarben–Klassifikation in CADIS und die Suche nach Quarsaren.* PhD thesis, Ruprechts–Karls–Universität Heidelberg. 9, 12, 13

[Wolf et al., 1999] Wolf, C., Meisenheimer, K., Röser, H. ., Beckwith, S. V. W., Fockenbrock, R., Hippelein, H., von Kuhlmann, B., Phleps, S., and Thommes, E. (1999). Did most high-redshift quasars escape detection? *Astronomy and Astrophysics*, 343:399–406. 9

[Wolf et al., 2001] Wolf, C., Meisenheimer, K., Röser, H. J., Beckwith, S. V. W., Chaffee, F. H., Fried, J., Hippelein, H., Huang, J. ., Kümmel, M., von Kuhlmann, B., Maier, C., Phleps, S., Rix, H. ., Thommes, E., and Thompson, D. (2001). Multi-color classification in the calar alto deep imaging survey. *Astronomy and Astrophysics*, 365:681–698. 13, 14, 23, 33

[Wolf et al., 1998] Wolf, C., Mundt, R., Thompson, D., Chaffee, F., Beckwith, S. V. W., Fockenbrock, R., Fried, J., Hippelein, H., Huang, J. ., von Kuhlmann, B., Leinert, C., Meisenheimer, K., Phleps, S., Röser, H. ., and Thommes, E. (1998). Discovery of three very distant M and L dwarfs. *Astronomy and Astrophysics*, 338:127–131. 9

[Zucca et al., 1997] Zucca, E., Zamorani, G., Vettolani, G., Cappi, A., Merighi, R., Mignoli, M., Stirpe, G. M., MacGillivray, H., Collins, C., Balkowski, C., Cayatte, V., Maurogordato, S., Proust, D., Chincarini, G., Guzzo, L., Maccagni, D., Scaramella, R., Blanchard, A., and Ramella, M. (1997). The ESO Slice Project (ESP) galaxy redshift survey. II. The luminosity function and mean galaxy density. *Astronomy and Astrophysics*, 326:477–488. 41, 59, 98

Acknowledgment

> *A faithful friend is a sturdy shelter:*
> *he that has found one has found a treasure.*
>
> Bible; Wisdom of Jesus Son of Sirach; Sir 6,14

A special thank to the management of the Max–Planck–Institute for Astronomy: I. Appenzeller, S. Beckwith, and H.–W. Rix for giving me the opportunity to carry out this work in this pleasant institute and especially Hans–Walter Rix for his helpful fair support and advice in difficult situations.

I thank my thesis advisor Prof. Dr. J. Fried for accepting me as a PhD student, the comments he provided to finish this work and for being a referee for this thesis.

Prof. Dr. Wielen I thank very much for accepting to be the second referee of my thesis.

Many thanks to the CADIS–team Christian Wolf, Hans Hippelein, Hermann-Josef Röser, Inge Thiering, Jiasheng Huang, Martin Kümmel, Ralf Fockenbrock, Sabine Drepper, Stefanie Phleps and the rest of the team, especially the team manager Klaus Meisenheimer for the nice teamwork and multifaceted support.

I thank Dr. G. Kauffmann for supporting me with a simulation of the galaxy evolution and the nice collaboration with Dr. Claudia Möller and Dr. U. Fritze–von Alvensleben and their modeled spectra.

My really special thank for their sacrifices goes to those people, who helped me with my weakness and supported me by checking my spelling and bringing this thesis into this form: Andrea Stolte, Bernd Lang, Gary Kilo, Marc Zimer, Mareike Ziegler, Martina Kleinheinrich, Peter Schuller, Rolf von Kuhlmann, Saskia von Kuhlmann and Stefan Noll

··· for reading and reading again ···

Thanks also to my sympathetic office colleges Marc Zimer, Mareike Ziegler, Martina Kleinheinrich, Ralf Fockenbrock, Simon Dye, Thomas Berkefeld and Ulrich Hiller for maintaining a pleasant atmosphere and I appreciate all the seconds, minutes and hours of discussions on scientific or less serious matters.

Really grateful I am for the support in essentials of the hard– and software to Andreas Tusche, Florian Briegel, Robert Weiß, Oliver Baumann, Ulrich Hiller, Thomas Helfert and Walter Rauh.

Thank you, to all my good friends and especially Anja S., Andrea S., Irina K., Katharina W. and Marei M. just for being there as good friends!

Many thanks to the forest and nature around the Königstuhl for the moments and walks of relaxation with all the good friends and colleges to refuel for the upcoming work.

Also I am very grateful that I had the possibility to learn how important and difficult it is for some people to keep promises, to be honest, to praise or the ability to say and mean *sorry* and that I had the chance to find out that for myself it will always be a major goal to never loose those important qualities.

And last but for sure not least my unlimited thank to my parents for giving me all the freedom, confidence and support I needed to realize this thesis and for their love.

Index